MEASURING ENERGETICS OF MAGNETIC VORTICES USING SMALL-ANGLE NEUTRON SCATTERING

A Dissertation

Submitted to the Graduate School
of the University of Notre Dame
in Partial Fulfillment of the Requirements
for the Degree of

Doctor of Philosophy

by

Allan Leishman

Morten Eskildsen, Director

Graduate Program in Physics
Notre Dame, Indiana

April 2021

MEASURING ENERGETICS OF MAGNETIC VORTICES USING SMALL-ANGLE NEUTRON SCATTERING

Abstract

by

Allan Leishman

Superconducting vortices and magnetic skyrmions are two types of mesoscale magnetic vortices that arrange themselves into periodic lattices in condensed matter systems. One method to study these structures is small angle neutron scattering (SANS), which is uniquely capable of resolving magnetic order throughout the bulk of a crystal in reciprocal space. Through careful modelling, the information that SANS provides can be used to extract more than just the magnetic structure, including the fundamental energetics and symmetries which are at play. This dissertation discusses three projects of this nature.

Skyrmions are of direct interest for future spintronic memory applications due to their intrinsic topological protection. Measurements of the energy barrier associated with this protection have often relied on generating metastable configurations of skyrmions which decay away over an observable period of time. We have developed a method of measuring the energy barrier in equilibrium (not metastable) skyrmion lattices (SkLs) by exploiting a hysteresis in the SANS signal of the prototypical skyrmion material MnSi. By modelling this hysteresis with a simple Preisach free energy and comparing it with atomistic spin simulations, the activation barrier is found to be several eV/ skyrmion. Additionally, it is confirmed that the SkL forms progressively in domains several hundred skyrmions in size.

The most promising applications of skyrmions involve using them as bits in a racetrack memory device. Such devices will likely drive the skyrmions into motion by using electric currents, and while the current density required to move skyrmions is substantially less than what is required to move domain walls, it still results in significant power consumption. We have sought to develop a new skyrmion device architecture to more efficiently produce SANS-visible SkL motion. By exploiting the Magnus force that current exerts on the SkL, we believe our new device will drive the SkL into a rotation at lower current densities than previously reported. Since rotations are visible in reciprocal space, this motion will be observable with SANS. Additionally, by measuring the rotation as a function of current density, we will be able to directly map the SkL-crystal lattice interaction potential and measure elastic properties of the SkL.

Superconducting vortex lattices (VLs) are highly sensitive to anisotropies in the underlying superconductivity. In the two-band superconductor MgB_2, orientation of the triangular VL is dictated by competing 6 and 12 fold anisotropies in the *ab* crystal plane. When these two contributions are comparable in energy, the VL fragments into counter rotated domains in the so called L phase. We have observed that when the VL is rotated out of the *ab* plane, the L phase rapidly shrinks in size. Above a critical rotation angle Ω_0, the phase disappears entirely, which can be explained by the 12 fold term in the superconducting anisotropy reversing sign.

For Laura

CONTENTS

FIGURES

TABLES

ACKNOWLEDGMENTS

I wouldn't have been able to complete this dissertation without the help of dozens (if not hundreds) of people that have guided and supported me throughout my physics career. Firstly, I would like to thank my advisor Morten Eskildsen. Morten has always been my loudest advocate, and his belief in me is what gave me the strength to push through all the late nights at the SANS beamline and writing this thesis. Coming to Notre Dame and working with his group as an undergrad is what convinced me to attend graduate school in the first place, and I am so grateful that I was able to continue my research with them during my PhD. The Eskildsen group has always felt like more of a family than a group of coworkers, and our camaraderie has made the long trudge of grad school much easier. Along those lines, I would like to thank all of my academic "older siblings", David, Steve, and Liz. You all taught me so much, from how to properly solder, to how to better handle the pressures and stresses of grad school, and I never could have done it without you. I would also like to thank my "younger siblings", Tony, Grace, and Nathan. Teaching you guys some of the useful (I hope) things I learned along the way reignited an excitement for science that allowed me to get this project across the line. To all my academic siblings, I treasure our friendships immensely, and I hope we can stay in touch.

This thesis also wouldn't have been completed without the helpful advice and mentorship of all my thesis committee members, Badih Assaf, Dinshaw Balsara, and Sylwia Ptasinska. Thank you all. Additionally, I would like to thank Ken Gomes and Jacek Furdyna who also provided support and guidance during my preparation for candidacy.

Next, I would like to thank all of the scientific collaborators that have made the included research projects possible. Thank you to Eric Bauer and Marc Janoschek, who both provided essential advice and samples as Morten and I took our first steps into the field of magnetic skyrmions. Thank you to Markus Bleuel, Lisa DeBeer-Schmitt, Dirk Honecker, Anna Sokolova, and Jon White, for being our local contacts for SANS measurements and patiently putting up with all the ridiculous ideas Morten and I came up with at the beamline. Thank you to Raí Menezes and Milorad Milošević, whose clever magnetic simulations gave us the final puzzle pieces we needed to understand the data we collected. Finally, thank you to Wai Kwok and Ulrich Welp, who provided me with countless hours of ideas and advice as I worked on the Corbino project.

Most importantly, I would like to thank my family for supporting me through all these years. Thank you to my parents for encouraging me to pursue a field that I enjoy, and never doubting that I would make it this far. Finally, thank you to Laura. You are one of the wisest people I know, and your patience and kindness got me through all the low days of grad school. Thank you.

All neutron scattering data presented in this thesis were collected at D33 at the Institut Laue Langevin (ILL); at GP-SANS at Oak Ridge National Laboratory (ORNL); at SANS I at the Paul Scherrer Institute (PSI); at Bilby at the Australian Nuclear Science and Technology Organisation (ANSTO); or at NG-7 at the National Institute of Standards and Technology (NIST). This work was supported by the U.S. Department of Energy, Office of Basic Energy Sciences, under Award No. DE-SC0005051. A portion of this research used resources at the High Flux Isotope Reactor, a DOE Office of Science User Facility operated by the Oak Ridge National Laboratory. I also acknowledge the support of the National Institute of Standards and Technology, U.S. Department of Commerce.

CHAPTER 1

MAGNETIC VORTICES IN CONDENSED MATTER

In this chapter I will provide a brief introduction to two types of mesoscale magnetic vortices that form in condensed matter systems: magnetic skyrmions and superconducting vortices. I will discuss the fundamental physics that leads to their formation, motivate their relevance to technological applications, and summarize the basic science questions surrounding these structures that this dissertation seeks to answer. These important questions are highlighted in **bold**.

1.1 Superconducting Vortex Lattices

In this section I will provide a brief introduction to superconductivity, one of the most fascinating and complex discoveries in the 20th century. I will summarize three models of superconductivity, the London Model, the Ginzburg Landau Model, and BCS Theory, and by combining all three motivate the emergence of the superconducting vortex lattice (VL). I will then provide a brief overview of the properties and behaviors of VLs, and finally introduce the novel VL of MgB_2, which is the subject of research in Chapter 4.

If not otherwise cited, the material in this section is based on the superconductivity chapters of Simon [122], Kittel [69], Ashcroft and Mermin [9], and Annett [8].

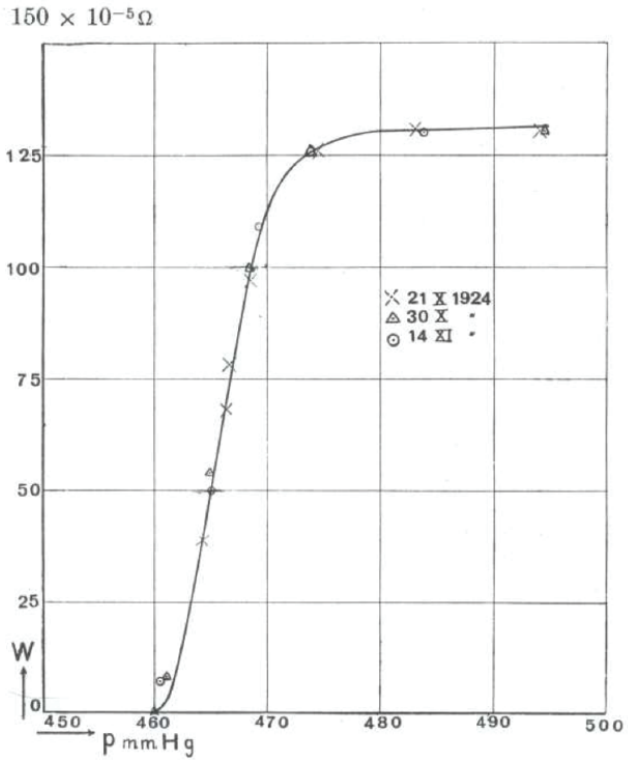

Figure 1.1. Superconducting phase transition of tin measured by Onnes. Here, temperature is determined from the vapor pressure of the liquid helium bath. T_c is observed at ∼464 mm Hg, or ∼3.7 K. *From Sizoo et al.*[123]

1.1.1 Introduction to Superconductivity

In 1911, Heike Kammerlingh Onnes observed a new phase of matter while cryogenically cooling mercury with liquid helium. When the temperature of the solid mercury cooled below 3 K, its electrical resistance dropped well below both what Onnes could measure and what was predicted from the otherwise linear resistivity of the metal [109]. It was later recognized that this rapid increase of conductivity was actually a phase transition into an entirely new phase which was given the name "superconductivity." In the following years, other materials were confirmed to host superconducting phases, including lead below the critical temperature (T_c) ∼7 K and tin below 3.7 K (Fig. 1.1).

These phases exhibited a collection of novel properties, the first of which being zero resistivity. This lack of resistance allowed persistent currents to remain in a superconductor without the need for a maintained applied voltage. This arguably was (and still is) the most attractive property of superconductors as it allows for the construction of high current devices for applying magnetic fields and transmitting power with minimal energy losses as long as the material is kept cooled below T_c.

Superconductors also demonstrated a peculiar opposition to magnetic fields, for whenever a superconductor was placed in an applied field H (or indeed if H was increased around a superconductor), the superconductor would become exactly oppositely magnetized such that the total magnetic field B within the superconductor was zero. Beyond that, if a conventional material was placed in a constant magnetic field and cooled below T_c, the superconductor would once again become magnetized and expel the field B (Fig. 1.2). This active expulsion of constant field demonstrates that a superconductor is not a zero resistance metal responding to a change in flux according to Faraday's Law, but something unique entirely. This phenomenon was named the Meissner effect after Walther Meissner (and Robert Ochsenfeld) who discovered it in 1933 [96].

It is important to note that the perfect diamagnetism of the Meissner effect can only be maintained up to a small applied field. Above its critical field H_c each superconductor reverts to the normal state, and indeed for all superconductors there exists a continuous curve in the (H, T) plane which separates the superconducting phase from the normal phase. A cartoon of this phase diagram is shown in Fig 1.3. Along this phase boundary, a second-order transition between the two phases occurs.

1.1.1.1 The London Model

One of the first successful attempts to model the behavior of a superconductor under the influence of electromagnetic fields was put forth by Heinz and Fritz London

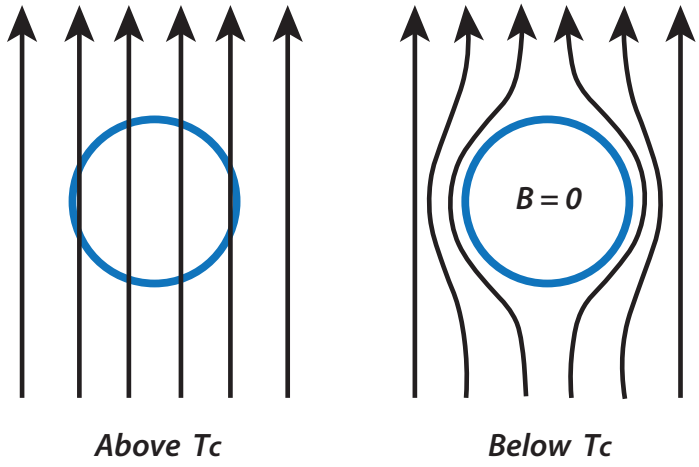

Figure 1.2. Magnetic field distribution before and after a superconducting phase transition. Since flux is conserved, the field density becomes greater in the region immediately outside the superconducting material. This increase in external field density is how Meissner and Ochsenfeld were able to confirm the effect.

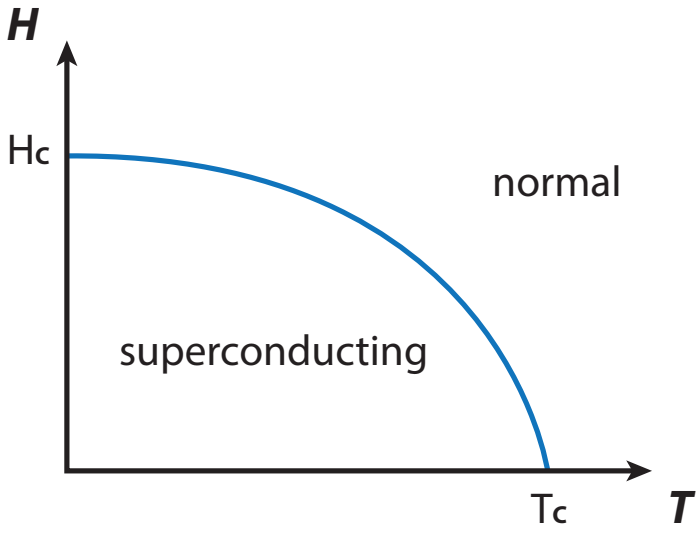

Figure 1.3. Superconducting phase diagram of a (type I) superconductor.

in 1935. They proposed that while charges flowing in conventional conductors follow Ohms Law,

$$\vec{j} = \sigma \vec{E} \tag{1.1}$$

charges in a superconductor should instead be constantly accelerating when electric field is applied, as if they are free particles

$$\frac{\partial \vec{j}}{\partial t} = \frac{ne^2}{m}\vec{E} \tag{1.2}$$

where n, e, and m are the density, charge, and mass of charges, respectively. The first London equation can be found by taking the curl of both sides

$$\frac{\partial}{\partial t}(\nabla \times \vec{j}) = \frac{ne^2}{m}(\nabla \times \vec{E}) \tag{1.3}$$

and by applying Faraday's Law

$$\nabla \times \vec{E} = -\frac{\partial \vec{B}}{\partial t} \tag{1.4}$$

$$\frac{\partial}{\partial t}(\nabla \times \vec{j} + \frac{ne^2}{m}\vec{B}) = 0 \tag{1.5}$$

so that we find

$$\nabla \times \vec{j} = -\frac{ne^2}{m}\vec{B} \tag{1.6}$$

One can gain more insight into the predictions of these equations by using Ampere's Law[1]

$$\nabla \times \vec{B} = \mu_0 \vec{j} \tag{1.7}$$

[1]Assuming no displacement current.

to adjust Equation 1.6

$$\nabla \times (\nabla \times \vec{B}) = -\frac{ne^2\mu_0}{m}\vec{B} \tag{1.8}$$

Next, by using the vector derivative identity for the curl of a curl

$$\nabla(\nabla \cdot \vec{B}) - \nabla^2\vec{B} = -\frac{ne^2\mu_0}{m}\vec{B} \tag{1.9}$$

and finally by using Gauss' Law for magnetism we are left with

$$\nabla^2\vec{B} = \frac{ne^2\mu_0}{m}\vec{B} \tag{1.10}$$

Solutions to this equation take the form of exponentials, and if we consider for instance the z component of B

$$B_z = A\ e^{z/\lambda_L} + C \tag{1.11}$$

where

$$\lambda_L \equiv \sqrt{\frac{m}{\mu_0 ne^2}} \tag{1.12}$$

it is clear that any solutions for a finite volume of superconductor must require B to exponentially decay of field upon entering the superconductor. The lengthscale of this decay is set by λ_L, and is named the "penetration depth" as it defines roughly how far the magnetic field B can penetrate into the superconductor. To get an estimate of the size of λ_L, let us consider a free electron gas with density of 10^{29} m^{-3}, which is roughly the order of magnitude of valence electron density in common metals [69]. Plugging in the free electron mass and charge, we find that $\lambda_L \sim 10^{-8}$ m. Therefore, the field is truly confined to the outermost shell of the superconductor. Any macroscopic measurement of a London superconductor would therefore observe perfect diamagnetism as Meissner and Ochsenfeld did.

It is also sometimes useful to express the current $\vec{j}$ in terms of the vector potential $\vec{A}$, where $\nabla \times \vec{A} \equiv \vec{B}$. One suitable choice of gauge, called the London gauge, sets

$$\nabla \cdot \vec{A} = 0 \tag{1.13}$$

so that we are left with

$$\vec{j} = -\frac{ne^2\mu_0}{m}\vec{A} \tag{1.14}$$

One final, special case worth considering is that of a small region of normal phase being enclosed by a superconductor. If we place a normal phase region along an infinitesimal line at the origin aligned with z, then from symmetry the field must point along z and cylindrical symmetry applies. Therefore, we can express 1.10 as

$$\frac{\partial^2 B_z}{\partial r^2} + \frac{1}{r}\frac{\partial B_z}{\partial r} - \frac{B_z}{\lambda_L^2} = 0 \tag{1.15}$$

This Bessel's Equation with $n = 0$, and has a solution in the form of the Bessel function $J_0(x)$

$$B_z(r) = CJ_0(r/\lambda_L) \tag{1.16}$$

Using the large x and small x approximations of J_0, we can get a better picture of the field profile in this structure. Near the normal region at $r = 0$, we have a concentrated region of field density

$$B_z(r) \approx C \ln \frac{\lambda_L}{r} \qquad r << \lambda \tag{1.17}$$

and far from this point we once again have an exponential decay of field set by λ_L.

$$B_z(r) \approx Ce^{-\frac{r}{\lambda_L}} \qquad r >> \lambda \tag{1.18}$$

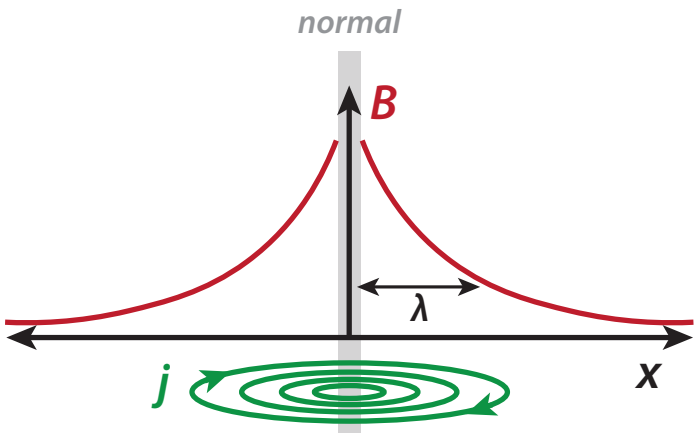

Figure 1.4. The London vortex.

This structure is called the "London vortex" (Fig. 1.4), and while it is not energetically favorable in the superconductors we have discussed so far, it will become relevant in later sections.

1.1.1.2 The Ginzburg Landau Model

Ginzburg and Landau attempted to take a more thermodynamic approach to modelling superconductivity by introducing a quantity called the order parameter ψ [76]. We now know $|\psi|^2$ to be a direct measure of the density of superconducting charge carriers, but for simplicity it can just be considered as a complex[2] quantity that distinguishes between the normal phase ($\psi = 0$) and the superconducting phase ($\psi \neq 0$). This value can vary throughout the superconducting phase pocket, but as we approach superconducting phase boundary, ψ should become vanishingly small. Since the superconducting phase transition is second order, the energy of the two phases must be equal along the phase boundary. Therefore, the free energy separation of these two phases $f_{sc} - f_{norm} = 0$ at all points all along the superconducting dome. If we take the special case of $H = 0$, then the free energy separation of the two

[2]Complex as in $\psi = a + bi$, not complicated, although it is that too.

phases *just* within the superconducting phase can be expanded in terms of the order parameter as follows:

$$f_{sc}(T, H = 0) - f_{norm}(T, H = 0) = a(T)|\psi(T)|^2 + \frac{b(T)}{2}|\psi(T)|^4 - \frac{\hbar^2}{2m}|\nabla\psi(T)|^2 \quad (1.19)$$

Here, we have excluded odd terms in ψ since the free energy must be a real (measurable) quantity, and higher order terms because near T_c the order parameter should be small. Finally, if we assume the simplest spacial scenario, a uniform superconductor for all space, then symmetry requires that ψ should be constant for all space and $\nabla\psi = 0$. Therefore,

$$f_{sc}(T, H = 0) - f_{norm}(T, H = 0) = a(T)|\psi(T)|^2 + \frac{b(T)}{2}|\psi(T)|^4 \quad (1.20)$$

Next, to find the most energetically favorable solution of this equation, we will look for $|\psi|$ such that the free energy of the superconducting phase (and therefore also $f_{sc} - f_{norm}$[3].) is minimized. Taking a derivative to look for minima with respect to $|\psi|$, we get

$$\frac{\partial(f_{sc}(T, H = 0) - f_{norm}(T, H = 0))}{\partial|\psi(T)|} = 0 = 2a(T)|\psi(T)| + 2b(T)|\psi(T)|^3 \quad (1.21)$$

$$0 = 2|\psi(T)|\ [a(T) + b(T)|\psi(T)|^2] \quad (1.22)$$

Here we find two roots of the equation, $\psi(T) = 0$ and $|\psi(T)|^2 = \frac{-a}{b}$. Taking one final derivative to determine which roots are minima, we find.

$$0 < 2a(T) + 6b(T)|\psi(T)|^2 \quad (1.23)$$

[3]The free energy difference of the two phases must also be minimized as f_{norm} is not and cannot be a function of ψ

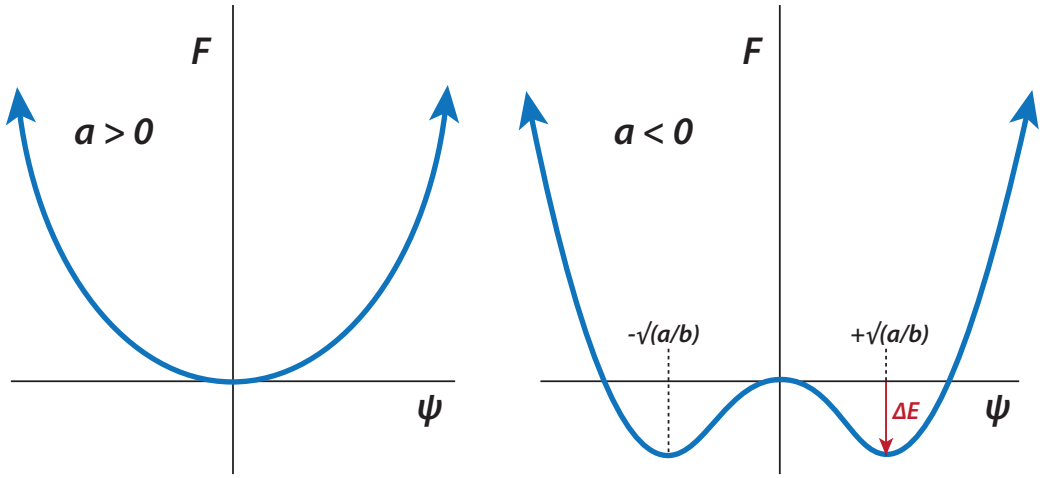

Figure 1.5. Ginzburg Landau model of the superconducting phase transition, with the free energy landscape above T_c ($a > 0$) and below T_c ($a < 0$) shown. The energy of condensation ΔE is also shown.

Therefore, $\psi(T) = 0$ will be a minimum only when $a(T) > 0$, and $|\psi(T)|^2 = \frac{-a}{b}$ will only be a minimum when $a(T) < 0$. Since the order parameter ψ serves as our "measure" of superconductivity in an a material, we can now recognize that the material transitions from the normal state to the superconducting state when a switches from positive to negative (Fig. 1.5). Therefore $a(T)$ must change signs from positive to negative as the sample is cooled through T_c. One simple and dimensionless functional form that accomplishes this is

$$a(T) = a_0[\frac{T}{T_c} - 1] \tag{1.24}$$

where $-a_0$ is the minimal value that $a(T)$ takes at zero temperature. When $a(T)$ crosses zero, the free energy of the system is reduced by an amount called the "energy of condensation." This is illustrated as ΔE in Fig. 1.5. The significance of this name will be discussed in Section 1.1.1.3.

One final piece of insight that we can gain from Ginzburg Landau theory is to

once again return to Equation 1.5 in the limit of small ψ (i.e. T close to but less than T_c).

$$f_{sc}(T, H=0) - f_{norm}(T, H=0) = a(T)|\psi(T)|^2 + \frac{b(T)}{2}|\psi(T)|^4 - \frac{\hbar^2}{2m}|\nabla\psi(T)|^2 \quad (1.25)$$

In order to understand the behavior of ψ near a SC-normal boundary, we need to look for solutions of ψ which are spatially inhomogeneous (i.e. $\nabla\psi \neq 0$). Minimizing the free energy to find such solutions requires extensive calculus and algebra[4], and the result of this process is the differential equation

$$0 = a(T)\psi(T) + b(T)|\psi(T)|^2\psi(T) - \frac{\hbar^2}{2m}\nabla^2\psi(T) \quad (1.26)$$

If we consider the simple 1D case, where a SC-normal boundary occurs at $x = 0$, with the $x > 0$ region being superconducting, then this equation has solutions of the form

$$\psi(x, T) = \psi_0 \tanh\left(\frac{x}{\sqrt{2}\ \xi_0(T)}\right) \quad (1.27)$$

where

$$\xi_0(T) \equiv \sqrt{\frac{\hbar^2}{2m|a(T)|}} \quad (1.28)$$

Here we have found our second important lengthscale in superconductivity, the Ginzburg Landau "coherence length" ξ_0. This parameter describes the intrinsic lengthscale over which the order parameter ψ can change. Personally, I think of ξ_0 as a measure of the flexibility of the order parameter in a given material. For long ξ_0 materials, ψ is very rigid and it takes a large distance from a superconductor-normal boundary to reach a maximum value. For short ξ_0 materials, the order parameter is more fluid, and ψ can quickly be restored to its bulk value over a minimal range.

[4]This is covered rigorously in Annett [8] Chapter 4.4.

Finally, if we combine 1.28 and 1.24, we find

$$\xi_0(T) \propto [1 - \frac{T}{T_c}]^{-1/2} \tag{1.29}$$

making it clear that ξ_0 grows very rapidly as T approaches T_c.

1.1.1.3 Insights from BCS Theory

While it is beyond the scope of this dissertation to rigorously develop the microscopic theory of superconductivity proposed by Bardeen, Cooper, and Schrieffer (BCS), it is nonetheless useful to qualitatively discuss their findings and the insights it can provide into the behavior of superconductors.

The simplest "cartoon" picture of BCS theory explains that superconductivity is a fundamentally quantum mechanical phase of matter that arises when electrons in a material experience an effective attraction to each other [15]. Normally, electrons strongly repel each other due to the Coulomb force. However, when moving through a material, they are also attracted to the positively charged ions fixed into the crystal lattice surrounding them. While both the electron and the lattice ions experience the same attractive force, the much greater mass of the ion makes it much slower to accelerate under said force. This means that the distortion of the crystal lattice lags behind the movement of a passing electron, creating a region of slightly higher charge density that follows in the wake of an electron (Fig. 1.6). At low temperatures, this region of slight positive charge can attract another electron and allows the two electrons to form a quasiparticle called a "Cooper pair" (Fig. 1.6.A).

Free electrons in a metal have spin 1/2 and therefore must follow Fermi-Dirac statistics. In the Drude Sommerfeld model, this forces one electron into each energy level, building all the way up to the highest occupied state[5] at the Fermi level ϵ_F (Fig.

[5]at zero temperature

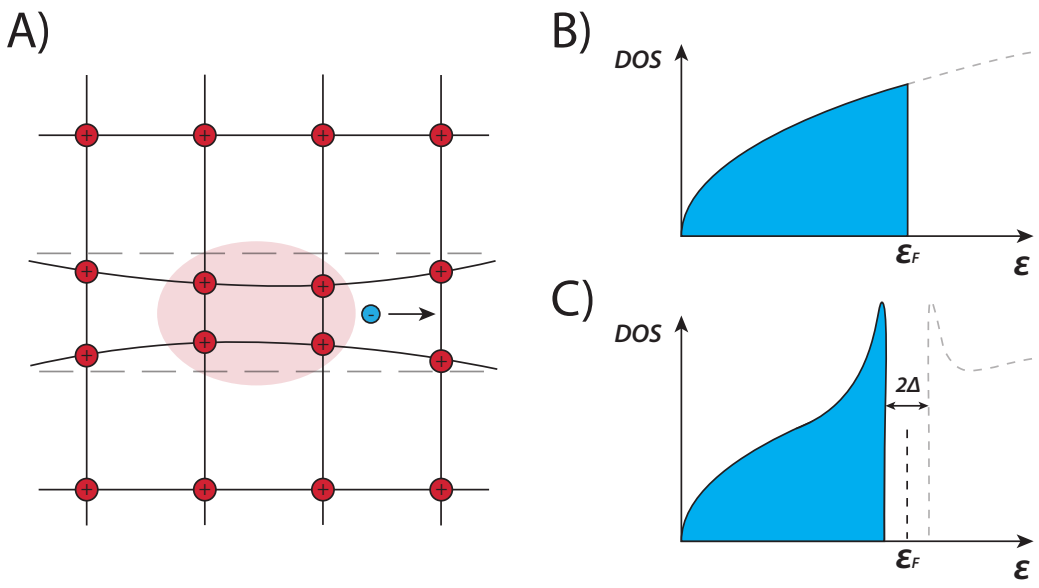

Figure 1.6. A) Cartoon picture of BCS theory, where a passing electron distorts the ionic charge distribution. Red shaded area represents the region of local positive charge density that could couple to a second electron. B) Density of states of a free electron gas at zero temperature. C) Density of states of a BCS superconductor at zero temperature (not to scale).

1.6.B). Cooper pairs, on the other hand, have an integer total spin and therefore are bosons. Unlike fermions, multiple bosons in a closed system can occupy the same quantum mechanical state, and so the density of states below ϵ_F rises rapidly. This destabilizes the Fermi surface, opening a small energy gap Δ at ϵ_F. Cooper pairs below the Fermi energy are highly correlated, and are said to have "condensed" [6] into a single quantum state. If the temperature is low enough ($k_bT < \Delta$), then thermal excitations within the lattice are too small to excite quasiparticles across the gap and the Cooper pairs therefore cannot be scattered. This allows the Cooper pairs to pass through the lattice uninhibited, and since they have a charge of $2e$, they can carry current without resistance.

This theory has several relevant implications for our discussion of superconductors. Firstly, the condensation of Cooper pairs and opening of an energy gap finally provides a microscopic mechanism for our system to reduce its free energy by entering the superconducting phase, explaining the condensation energy. Additionally, BCS theory allows us to better understand the meaning of Ginzburg Landau theory. The order parameter ψ is the Cooper pair wavefunction, such that $|\psi|^2$ measures the Cooper pair probability density. Additionally, the coherence length ξ_0 can be understood as the "size" of our Cooper pairs[7]. Finally, since it is Cooper pairs that carry the supercurrent, we need to be a bit more cautious about the properties we assume for our charges. Specifically, the charge $2e$ will make an appearance in several upcoming results, and we will transition to using the effective quasiparticle mass m^* where necessary.

---

[6] Hence, "condensation energy"

[7] More specifically, the size of the Cooper pair wavepacket.

1.1.1.4 Type I and Type II Superconductors

With the development of λ_L and ξ_0 we have introduced two lengthscales that are crucial to understanding the behavior of different superconductors. While λ_L describes the response of the supercurrent j to an external field, ξ_0 describes the "flexibility" of the underlying superconductivity. At this point it is important to note that the actual values of these parameters (λ and ξ) can vary substantially from the "optimal" values introduced by these theories (λ_L and ξ_0). For an example, adding defects or impurities to a crystal reduces the mean free path l of the quasiparticles, which has the effect of both increasing λ and decreasing ξ.

Until this point, we have only discussed the case of superconductors perfectly screening external fields via the Meissner effect up until a maximum field of H_c. This is the case for many elemental superconductors, especially those that were first discovered. However, as more superconductors were discovered, it became clear that some did not entirely leave the superconducting phase upon leaving the Meissner state but instead entered a "mixed state", where the bulk remains electrically superconducting, but small regions of normal phase intermix with the superconductor and allow magnetic flux to penetrate the bulk[8] (Fig. 1.7). This new class of superconductors were called "type-II" superconductors to distinguish them from the previously discussed "type-I" superconductors. A cartoon of the type-II phase diagram is shown in Fig. 1.8, with the mixed state located between critical fields H_{c1} and H_{c2}.

A useful way to distinguish between these two types of superconductor is by introducing the Ginzburg Landau parameter $\kappa \equiv \frac{\lambda}{\xi}$. Type-II superconductors have larger values of κ than type-I's, with the exact cut off line between the two classes normally set at $\kappa = \frac{1}{\sqrt{2}}$. The reason for this difference can be understood qualitatively by con-

[8]In fact, the London brothers discussed the experimental observation of "frozen in" field lines in their seminal work, however dismissed it at as being due to defects since it was inconsistent with the Meissner effect.

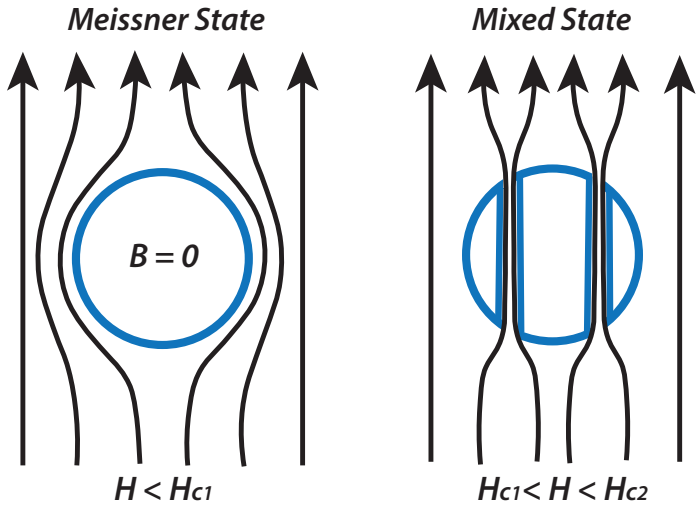

Figure 1.7. Behavior of a type-II superconductor in the Meissner ($H < H_{c1}$) and mixed state phases ($H_{c1} < H < H < H_{c2}$).

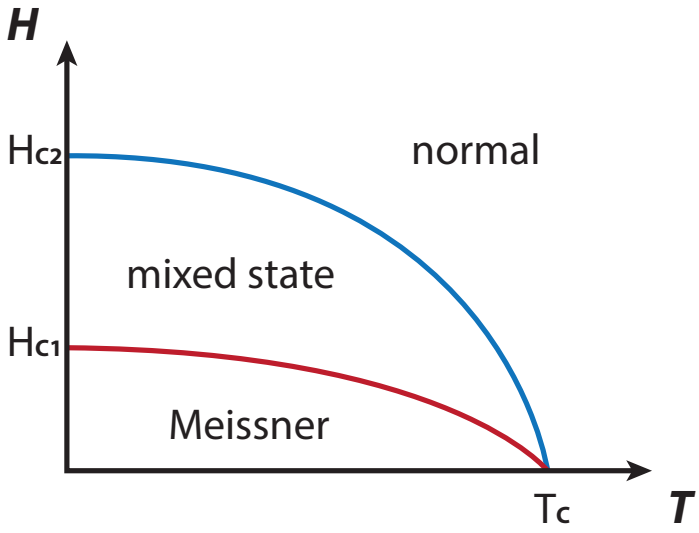

Figure 1.8. Phase diagram of a type-II superconductor.

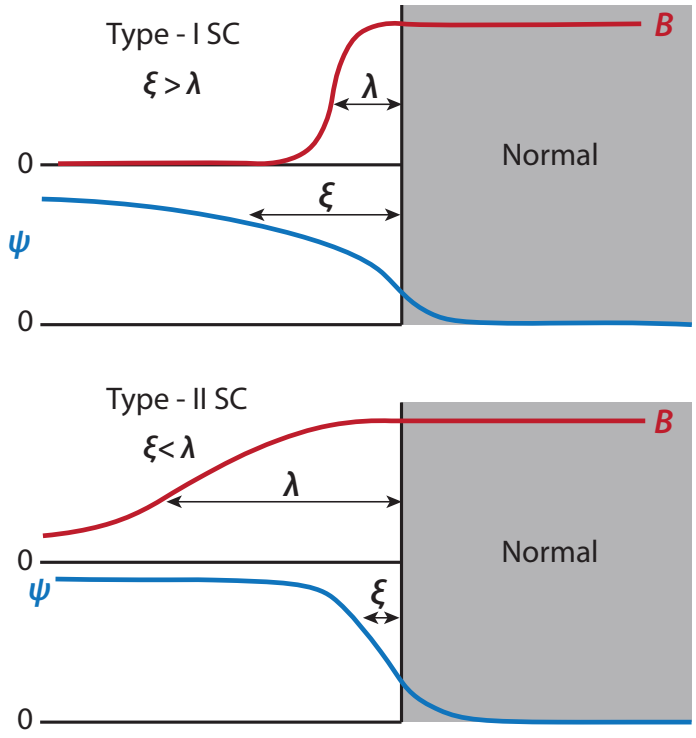

Figure 1.9. Visualization of the penetration depth and the coherence length in a type-I (top) and type-II (bottom) superconductor.

sidering an interface between a superconducting region and normal phase region (Fig. 1.9). For a strongly type-II material, $\lambda > \xi$, and so the superconductor can quickly reach the maximal value of the order parameter despite the deeply penetrating fields. From an energetics standpoint, this means that the superconductor gains benefits of reducing its free energy via condensation while also not paying the energy penalty to expel the field out of the material. Because of this, it is actually energetically favorable for the type-II superconductor to form as many superconducting-normal interfaces as possible. This is accomplished by introducing many microscopic normal phase regions into the superconducting bulk, each of which carries the minimal amount flux allowed by quantum mechanics, the flux quantum $\Phi_0^{sc} = \frac{h}{2e}$, through

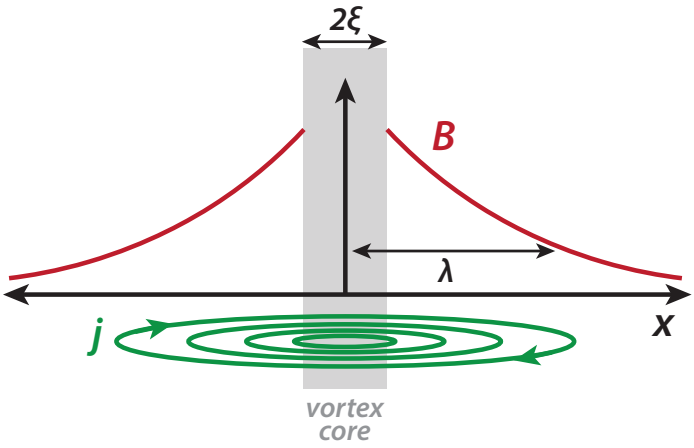

Figure 1.10. The superconducting vortex.

the sample[9]. These small regions are called "vortices" due to the supercurrents that circulate around them to screen the magnetic field (Fig. 1.10). The central, normal phase region of the vortex is referred to as the "vortex core", and its size is dictated by the coherence length. The field density outside of the vortex core, as well as the supercurrents which screen the field, decay with a lengthscale set by the penetration depth.

1.1.1.5 The Vortex Lattice

Since each vortex carries one quantum of flux, the density of vortices in a superconductor is directly proportional to the applied field. Each vortex repels its neighbors due to their magnetization, and so in suitably clean materials[10] the vortices will be uniformly distributed throughout the crystal. These vortices tend to follow the direction of the applied field, however anisotropies within the underlying crystal lattice

[9]Note the Cooper pair charge $2e$ which distinguishes Φ_0^{sc} from the single electron flux quantum Φ_0^e.

[10]Here, clean means free of crystal impurities and defects, which have a tendency to "pin" vortices to one location. In the superconducting crystal studied in this dissertation, MgB_2, pinning is negligible.

can distort the vortex lines away from the external field direction [73, 111].

In 1957, Alexei Abrikosov found a periodic solution to the Ginzburg Landau equation which described the mixed state in clean type-II superconductors [5]. This solution described a 2D lattice of vortices lying in the plane perpendicular to the applied field, with the vortices themselves extending parallel to the field direction. This structure came to called a "flux line lattice" or, for the purposes of this dissertation, a "vortex lattice" (VL). It was later demonstrated that the most energetically favorable VL structure in a perfectly isotropic superconductor was a triangular lattice, which is not suprising considering that it is the most efficient packing of circles in 2D. However, the theoretical difference in free energy between the triangular and square VLs was only $\sim 2\%$ [70]. Because this difference is so small, anisotropies in the superconductivity or underlying crystal lattice can tilt the energetics in favor of a square VL or even more exotic VL symmetries. This is especially relevant at higher fields, where the higher density of vortices increases the importance of short range vortex-vortex interactions.

Since each vortex carries one quantum of flux, the unit cell of the VL must always have the same area regardless of lattice symmetry. The area of this cell A is given by the flux density of the applied field $\mu_0 H$:

$$A = \frac{\Phi_0^{sc}}{\mu_0 H} \tag{1.30}$$

From here we can calculate the lattice parameter of any arbitrary VL symmetry subject to the constraint $|\vec{a_1} \times \vec{a_2}| = A$. Taking the most symmetric extremes for example, we find for the four-fold square VL

$$a_0^{sqr} = \sqrt{\frac{\Phi_0^{sc}}{\mu_0 H}} \tag{1.31}$$

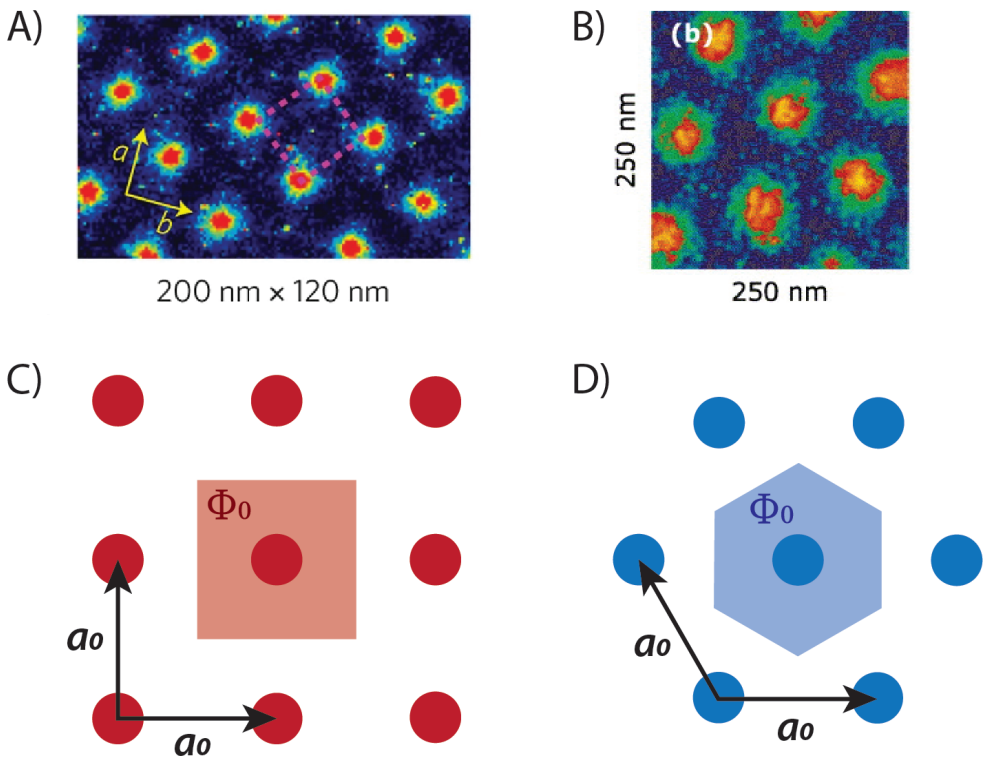

Figure 1.11. Scanning tunneling microscopy images of A) the square VL of $CeCoIn_5$ (*from Zhou et al.* [138]) B) the triangular VL of MgB_2 (*from Eskildsen et al.* [34]) . In both images the color indicates the density of states at the Fermi energy. Brighter regions reflect the higher density of states due to suppression of the superconducting energy gap within the vortex core. C) Cartoon of the square VL. D) Cartoon of the triangular VL. Shaded regions indicate the one-flux quantum unit cells.

and for the triangular VL

$$a_0^{tri} = \sqrt{\frac{2\Phi_0^{sc}}{\sqrt{3}\mu_0 H}} \tag{1.32}$$

Assuming reasonable applied fields of order 1 T, this leads to lattice parameters of order ∼50 nm. Since this lattice is so much larger than the underlying crystal structure, the two are said to be incommensurate. Images of some vortex lattices are shown in Fig. 1.11.

1.1.2 Effects of Anisotropy on the Vortex Lattice

As suggested in the previous section, the VL is highly sensitive to any anisotropy in the plane which the screening supercurrents are moving through. Any anisotropy in the Fermi surface or in the superconducting energy gap Δ within this plane can correspondingly affect the penetration depth and therefore the VL symmetry. Anisotropy in the penetration depth results in a distortion of the VL such that the lattice vectors no longer have equal magnitudes. However, since the VL unit cell area is still fixed by flux quantization, these vectors are still subject to the constraint that $|\vec{a_1} \times \vec{a_2}| = \frac{\Phi_0^{sc}}{\mu_0 H}$.

This effect gets particularly interesting in the case where the superconducting anisotropy is incompatible with the "ideal" triangular VL, such as the case in the four-fold symmetric [100] planes of niobium [77, 78, 99]. The result is a rich VL phase diagram, with many different symmetries and structures. However, interesting VL structures can still arise in hexagonal superconductors. In these materials, while the VL normally remains triangular, the alignment of the VL with respect to the crystal lattice is dictated by otherwise weakly coupling higher order terms in the anisotropy. This is the case for the VLs of UPt_3 [45, 10] and MgB_2 [29, 30], the latter of which we will discuss in detail later.

1.1.3 Practical Relevance of Superconducting Vortices

By far the most common industrial use for superconducting materials is to draw them into wires to carry the extremely high currents necessary to produce high magnetic fields. Since type-II superconductors consistently have higher critical temperatures and fields, they are almost universally the choice for these applications. This means that vortices will form in these materials, and the behavior of these vortices can have a profound impact on the performance of the superconductor.

When current j is passed through superconductor in a direction perpendicular to the applied field, the magnetized vortex core experiences an orthogonal Lorentz force

$$\vec{F}_L = \vec{j} \times \Phi_0^{sc} \hat{z} \tag{1.33}$$

which will drive the vortex into motion across the superconducting bulk. Assuming the simplest case where the Lorentz force on the vortex is only resisted by a drag force, the steady state velocity of the vortex can be written as

$$\vec{v}_\Phi = \frac{j\Phi_0^{sc}}{\eta}\hat{y} \tag{1.34}$$

where η is the drag coefficient. This motion of flux lines is called "flux flow", and the resulting change of magnetic flux across the sample induces an electric field according to Faraday's Law.

$$\int \vec{E} \cdot d\vec{l} = -\frac{\partial}{\partial t} \int \vec{B} \cdot d\vec{S} \tag{1.35}$$

Assuming a uniform slab of width l, the rate of change of flux will just be given by the vortex velocity times the number of vortices

$$\frac{\partial \Phi}{\partial t} = \frac{\Phi_0^{sc} \Delta N_\Phi}{\Delta t} = \frac{\Phi_0^{sc} n_\Phi l^2}{l/v_\Phi} = \Phi_0^{sc} n_\Phi l v_\Phi \tag{1.36}$$

where n_Φ is the area density of vortices. If we solve for the electric field within the superconductor

$$\vec{E} = \Phi_0^{sc} n_\Phi \vec{v}_\Phi = \frac{(\Phi_0^{sc})^2 n_\Phi}{\eta}\vec{j} \tag{1.37}$$

we find a new form of Ohm's law, where the motion of vortices induces a resistance in our superconductor, with resistivity

$$\rho_{\text{flow}} = \frac{(\Phi_0^{sc})^2 n_\Phi}{\eta} \tag{1.38}$$

Clearly, this resistance is undesirable in a superconductor, and it has the effect of limiting both the upper critical field and the critical current density of the material.

One way to mitigate this effect is to engineer defects into the crystal such that the vortices get "pinned" in one location, preventing them from drifting under the Lorentz force. The more effectively that the vortices are pinned, the greater the performance of the superconducting device, and so to build higher field superconducting magnets we must develop better understanding of the behaviors of vortices and VLs.

1.1.4 The Vortex Lattice of MgB_2

Magnesium diboride (MgB_2) was first synthesized by Jones and Marsh in 1953 [62]. It is a hexagonal crystal with $a_0 = 3.0834$ Å and $c_0 = 3.5213$ (spacegroup P6/mmm) formed of honeycomb planes of boron atoms (B-B separation = 1.780 Å) separated by triangular planes of magnesium atoms (Mg-Mg separation = 3.083 Å) (Fig. 1.12). High quality single crystals of MgB_2 can be grown by heating elemental magnesium and boron under high pressures to 1700-1800 °C [65]. Crystals grown by this method are normally smaller than 1 mm in all dimensions.

Although it was synthesized in the 50's, it wasn't until 2001 that MgB_2 was discovered to be superconducting below a critical temperature of 39 K [103]. While this T_c was well below the records being set by cuprate based superconductors, MgB_2 still gained notoriety as 39 K is much higher than other conventional[11] superconductors. It was also discovered that MgB_2 hosts two bands at the Fermi surface which both superconduct independently of each other. The two bands are formed predominately by σ bonding (π bonding) within the boron planes, and as such are called the σ (π) bands, respectively. The Fermi surface of these bands is shown within Fig. 1.13. From *ab initio* calculations, it was discovered that the σ band in particular couples very strongly to vibrational modes within the boron planes, enhancing Cooper pairing and leading to extraordinary T_c [26]. This discovery prompted a wave of optimism for

[11] Here, "conventional" means those superconductors whose pairing can be understood within the limits of BCS theory.

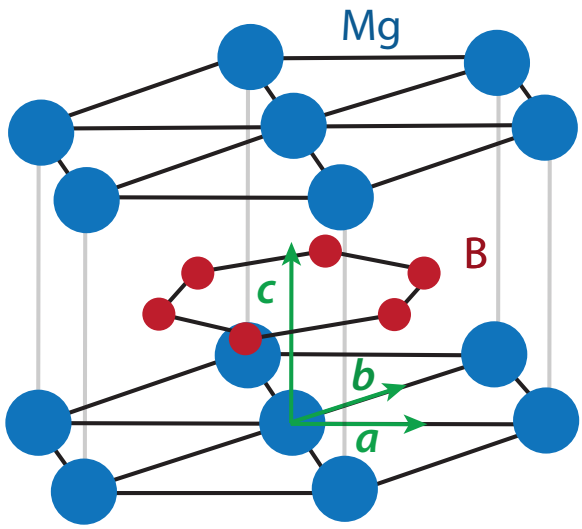

Figure 1.12. Crystal structure of MgB_2. *Adapted from Abanador et al.* [4]

a new family of high T_c, BCS superconductors based on comparatively light elements, like boron, carbon, and nitrogen that so far has not been realized[12].

The σ band is composed of four, semi-cylindrical sheets located at the corners of the Brillouin zone (BZ) and has a superconducting energy gap of $\Delta_\sigma \approx 6.8$ meV. Quasiparticles within the σ band are strongly confined to the boron planes, and as such the σ band is often referred to as a quasi two dimensional band. The π band is formed of a "webbed tunnel" structure at the center of the BZ, and has much smaller energy gap of $\Delta_\pi \approx 1.8$ meV. As magnetic field is increased, superconductivity within the π band is rapidly suppressed, and the density of states returns to that of a single gap superconductor.

As it turns out, competition between these two superconducting bands generates a phenomenally interesting vortex lattice phase diagram (Fig. 1.14)[30]. For all points within the superconducting phase, MgB_2 forms a triangular VL, but the orientation of the VL relative to the crystal lattice changes throughout (H, T) space. For low

[12]At least not at atmospheric pressures.

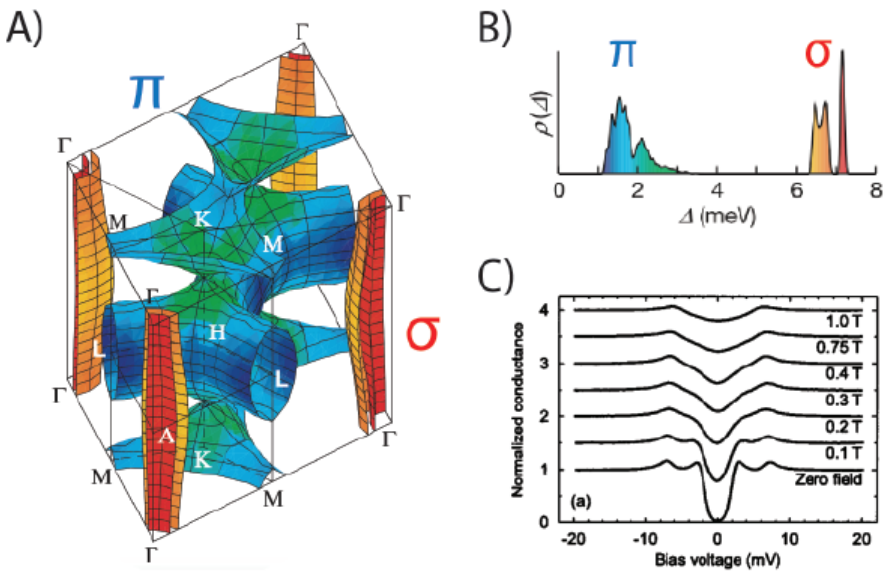

Figure 1.13. A) Fermi surface of MgB_2, showing both the sigma (orange) and pi bands (blue). *Adapted from Choi et al.* [26] B) Superconducting energy gap size Δ for the two bands. *Adapted from Choi et al.* [26] C) Suppression of the double gap structure with increasing magnetic field. *From Eskildsen et al.* [37]

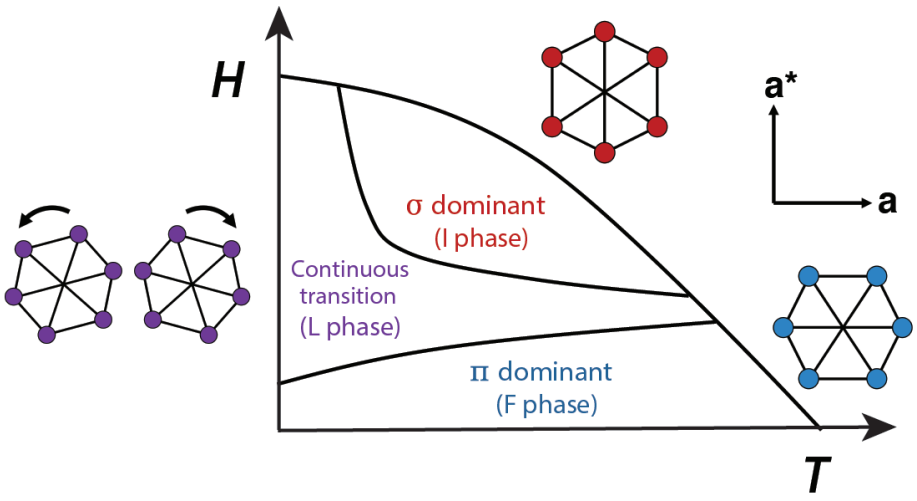

Figure 1.14. Qualitative VL phase diagram of MgB_2, showing the F, L and I phases and the corresponding triangular VL alignment.

fields ($\mu_0 H < 0.6$ T), the high anisotropy of the π band aligns the vortex lattice vectors along the a crystalline axis in the so-called F phase. However, as field is increased the influence of the π band becomes suppressed, and above $\sim$ 1 T, the anisotropy of the sigma band rotates the VL vectors 30° such that they are aligned with the a^* crystal axis. This region is known as the I phase. In between the F phase and the I phase, the two bands compete for superiority, and the VL experiences a region of continuous rotation from a to a^*, known as the L phase. Since there are two, degenerate directions the VL can rotate (clockwise and counterclockwise), the VL fractures into counter-rotating domains roughly $\sim$1 to 10's of microns in size [86].

The domain walls within the L phase have a profound impact on the behavior of the VL, as phase transitions between the L and F phases, and between the L and I phases require either forming or destroying these domain walls. There is a steep energy barrier associated with both processes, and the result is that very robust metastable VL structures can be formed if a phase boundary is crossed without providing enough energy to overcome the barrier [30]. These metastable states can be

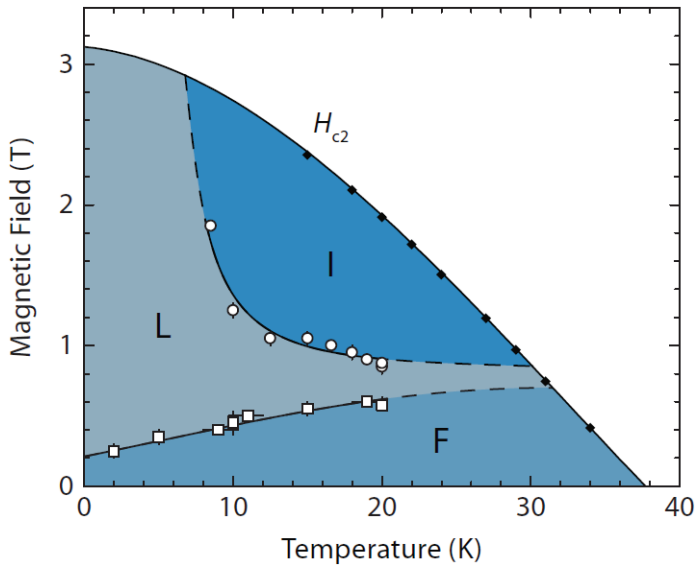

Figure 1.15. Quantitative VL phase diagram of MgB_2, showing the F, L and I phases. *From Das et al.*[30]

destroyed by oscillating the magnitude of the applied field, which in turn oscillates the vortex density [116]. The rate of decay to the equilibrium VL configuration depends on the magnitude of the field oscillations, and can be modelled as an activated phase transition, much like martensitic phase transitions observed in steel [88, 87]. These metastable states are demonstrably not a result of vortex pinning due to defects within the material, but instead are a result of the intrinsic VL structure [116].

The preferred alignment of the VL within the L phase can be well modelled as a result of competing six- and twelve-fold rotation symmetric anisotropies [137]. We can write down the free energy of the VL orientation

$$\delta F(\varphi) = K_6 \cos(6\varphi) + K_{12} \cos(12\varphi), \tag{1.39}$$

where φ is the angle between the a axis and the VL vector. Minimizing this free

energy, we find the preferred orientation to be determined by

$$\kappa = -4\cos(6\varphi), \tag{1.40}$$

where $\kappa \equiv \frac{K_6}{K_{12}}$. From here we see that by varying κ over the range -4 to 4, the VL continuously rotates from $\varphi = 0$ to $\varphi = 30°$.

The vortex lattice within MgB_2 is relatively isotropic when field is applied parallel to the crystalline c axis and the supercurrents therefore lie in the $a-b$ plane. However, as field is rotated toward the $a-b$ plane, the larger penetration depth and smaller coherence length along the c direction begins to influence the superconductivity. The increasing coherence length causes the upper critical field H_{c2} to grow very rapidly, from ∼3.1 T at $H \parallel c$ to ∼18 T at $H \perp c$[13] (Fig. 1.16.A)([92]. Additionally, since the Ginzburg Landau parameter κ is not isotropic within the $a-c$ plane, the VL distorts from an equilateral triangular VL to an isosceles triangular VL, with the shorter lattice vector pointing along c (Fig. 1.16.B).

Since the behavior of the VL depends so strongly on the weak six and twelve anisotropies of the boron planes when $H \parallel c$, a natural question to ask is how the VL phase diagram changes when anisotropy is increased even further by forcing the lattice to form in the $a-c$ plane. This anisotropy can of course be tuned continuously by rotating the applied field angle between $H \parallel c$ and $H \perp c$. **How does the VL phase diagram respond to increasing anisotropy as the field is rotated away from c? Is robust metastability maintained between VL phases?**

1.2 Magnetic Skyrmion Lattices

In this section I will briefly explain the antisymmetric exchange interaction and the novel phases of magnetic order that arise when it is added to otherwise ordinary

[13]Depending on sample quality

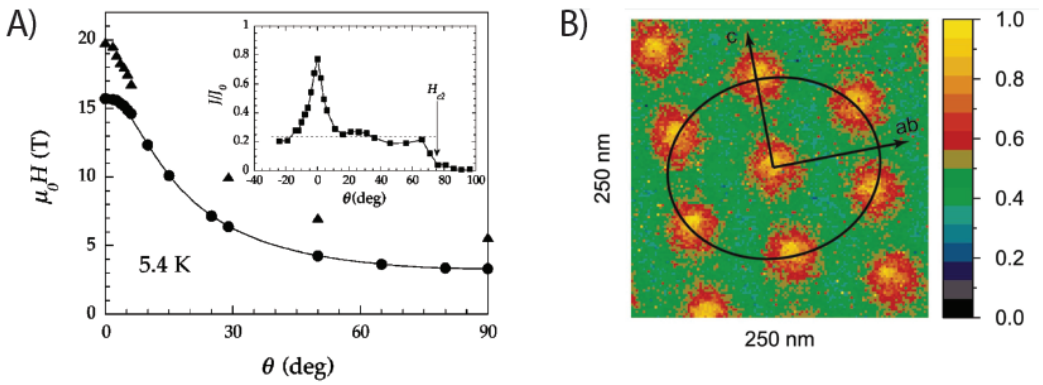

Figure 1.16. A) Increase in the upper critical field H_{c2} of MgB_2 as the field direction is rotated from $H \parallel c$ ($\theta = 90°$) to $H \perp c$ ($\theta = 0°$). Inset shows the corresponding growth of critical current j_c. *From Lyard et al.*[92] B) Distortion of the VL of MgB_2 to an isosceles triangular structure when $H \perp c$. Observed in real space via scanning tunneling microscopy. *From Eskildsen et al.*[37]

ferromagnets. Among these magnetic phases is the magnetic skyrmion lattice (SkL), which is of particular relevance for future spintronic research. After motivating the study of SkLs under application of electric currents, I will finally provide an overview of the prototypical SkL material MnSi, which is the subject of research in Chapters 3 and 5.

1.2.1 Introduction to Chiral Magnetism

In 1952, Néel and Pauthenet observed a very small magnetization in the antiferromagnetic crystal α-Fe_2O_3 [89]. While this "weak" ferromagnetism could be explained by the formation of Bloch domain walls between antiferromagnetic domains [82], it took the work of Dzyaloshinsky [33] and Moriya [98] to demonstrate that such a structure could be energetically favorable. Moriya demonstrated that by adding spin-orbit coupling to P.W. Anderson's model of the superexchange interaction [7], a new term

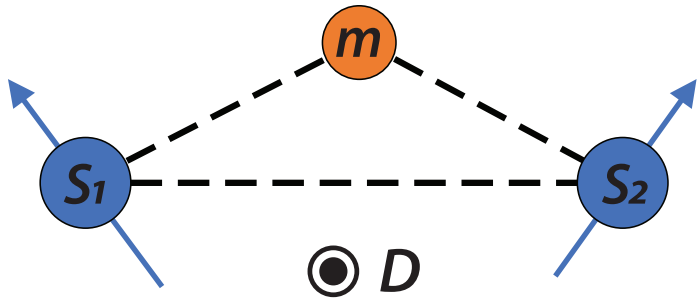

Figure 1.17. Dzyaloshinsky-Moriya interaction of spins S_1 and S_2 moderated through non-magnetic atom m.

is introduced to the spin Hamiltonian:

$$\vec{D}_{ij} \cdot [\vec{S}_i \times \vec{S}_j] \tag{1.41}$$

This antisymmetric exchange interaction, often referred to as the Dzyaloshinsky-Moriya Interaction (DMI), favors spins S_i and S_j aligning perpendicular. The vector $\vec{D}_{ij}$ is a constant determined by the symmetry of the two interacting spins as well as the superexchange moderating atom m (Fig. 1.17). For $\vec{D}$ to be nonzero, the two spins must not share an inversion center at their midpoint, but rather possess mirror symmetry. From here, the direction of $\vec{D}$ can be determined from further symmetries following the rules set forth by Moriya [98]. In the case of Fig. 1.17, $\vec{D}$ must point perpendicular to the $S_1 - m - S_2$ plane.

Recognizing the tendency of the DMI to align neighboring spins perpendicular, it is natural that combining the DMI with the regular (symmetric) exchange interaction J $(\vec{S}_i \cdot \vec{S}_j)$ and its preference for parallel/antiparallel spins could result in novel spin structures. Rounding out the Hamiltonian with the Zeeman energy, we reach the full

extended Heisenberg Hamiltonian:

$$H = \sum_{<i,j>} [J\ (\vec{S}_i \cdot \vec{S}_j) + \vec{D}_{ij} \cdot (\vec{S}_i \times \vec{S}_j)] + \mu\ \sum_i \vec{B} \cdot \vec{S}_i \tag{1.42}$$

In searching for novel magnetic states, promising candidate materials are limited to those where neighboring spins meet the symmetry requirements to produce a nonzero DMI. One easy way to break inversion symmetry is to substrate a conventional magnetic system onto a second, nonmagnetic material. In this case, atoms in the substrate material can serve as a moderators for superexchange between neighboring atoms in the magnetic material, generating a nonzero $\vec{D}$ in close proximity to the interface. These "interfacial DMI" systems are of particular interest for spintronics applications due to their compatibility with other thin film devices and techniques [41].

Alternatively, inversion symmetry can be broken by placing magnetic atoms on a crystal lattice that is itself non-centrosymmetric. The most common example of these crystal structures is the B20 structure (space group $P2_13$), a cubic lattice which is inherently chiral (see Fig. 1.24). In such a case, a nonzero $\vec{D}$ can be produced between next-nearest neighbor magnetic atoms throughout the entirety of crystal. It is often easier to study the fundamental nature of the resulting magnetic structures within these "bulk DMI" systems due to the larger relevant sample volume, and as such they are the focus of this dissertation. What follows is a summary of a few relevant magnetic phases which arise in bulk materials with nonzero DMI below the magnetic ordering temperature.

1.2.1.1 Helical/ Cycloidal Magnetization

At low temperature T and magnetic field B, since $|\vec{D}|$ is normally much smaller than J, the DMI serves as a small perturbation upon the otherwise ferromagnetic/

antiferromagnetic ordering of the exchange interaction. Depending on the direction of $\vec{D}$, the DMI tilts the spins either within the plane containing neighboring spins to produce cycloidal ordering (Fig. 1.18.A), or out of the plane containing neighboring spins producing helical ordering (Fig. 1.18.B). Naturally, the families of materials that these structures form in are referred to as conical magnets and helimagnets, respectively. The wavelength of these periodic structures is given in units of lattice spacings by the ratio $J/|\vec{D}|$, with stronger DMI twisting the magnetization faster. It is often useful to define a wavevector $\vec{Q}$ for these periodic structures, where $\vec{Q}$ points along the axis of the helix/cycloid and has a magnitude $|\vec{Q}| = \frac{|\vec{D}|}{J}$.

In 3D materials, the orientation of $\vec{Q}$ is often largely degenerate, and ultimately determined by weak coupling to high symmetry directions in the crystal [12]. This has the effect of fracturing the magnetic ordering into coexisting domains with different $\vec{Q}$'s.

1.2.1.2 Conical Magnetization

For helimagnets, increasing the field above a critical field B_{c1} (Fig. 1.19) breaks the orientation degeneracy of $\vec{Q}$ and all helices reorient such that $\vec{Q} \parallel \vec{B}$. Additionally, the local magnetization vectors begin tilting towards $\vec{Q}$, giving the conical phase its name (Fig. 1.18). This tilting grows continuously with field until B_{c2} where the crystal becomes fully ferromagnetically ordered.

1.2.1.3 Magnetic Skyrmion Lattice

One final structure that can form in chiral magnets is the skyrmion lattice (SkL). In the B20 magnets, this structure occurs in a small region of temperature-field space near the ordering temperature T_N known as the A Phase (Fig. 1.19). The magnetic structure of this phase can be considered as three separate helices, each oriented with $\vec{Q}$ 120° from each other within the plane perpendicular to B. However, it is much

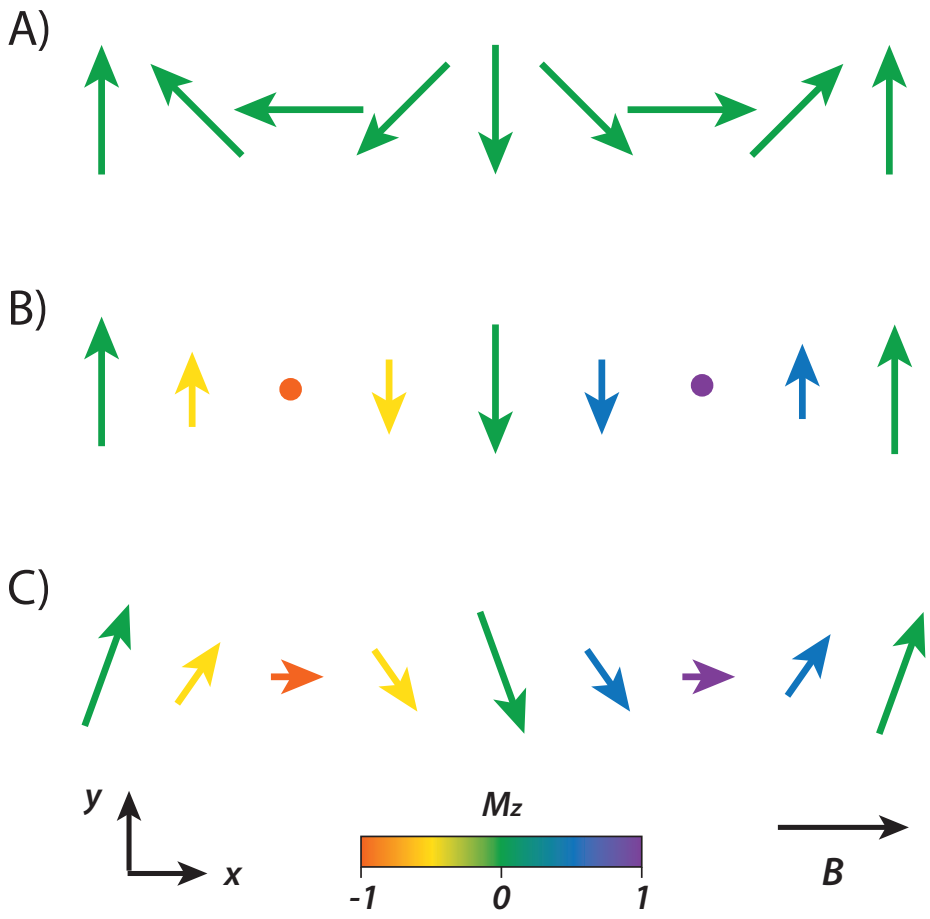

Figure 1.18. Spins in a 1D chain in forming a A) cycloidal structure, B) helical structure, C) conical structure. For all structures, $\vec{Q}$ points along x and the spin component out of the page M_z is indicated by the color bar. Total magnetic field B is also along x. In all structures, all spins have the same total magnetic moment, only the orientation changes from one site to the next.

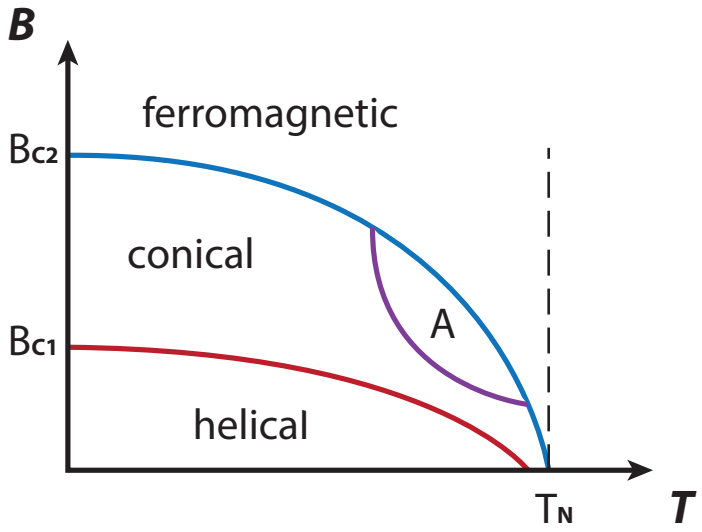

Figure 1.19. Qualitative phase diagram for the B20 helimagnets.

more common (and often more useful) to consider the structure as a 2D lattice of quasiparticles called skyrmions[14]. These 2D particles consist of a central spin oriented antiparallel to the applied magnetic field and the surrounding region where the spins rotate 180° back to parallel with the field. If forming in a cycloidal magnet, this rotation of spins occurs along the radius of the skyrmion, forming a "Néel type" skyrmion (Fig. 1.20.A). On the other hand, if forming in a helimagnet, the rotation of spins occurs about the radius of the skyrmion, forming a "Bloch type" skyrmion (Fig. 1.20.B). In both cases the naming convention comes from those previously established for magnetic domain walls[17]. More colloquially, these two classes of skyrmions are referred to respectively as "hedgehog" and "vortex" skyrmions, for obvious reasons. It is important to note that even in bulk systems, skyrmions often demonstrate individual particle behaviors, such as allowing for SkLs to change lattice symmetry [104].

[14]Skyrmions derive their name from nuclear physicist Tony Skyrme who proposed using a similar vector field structure to model nucleons [124].

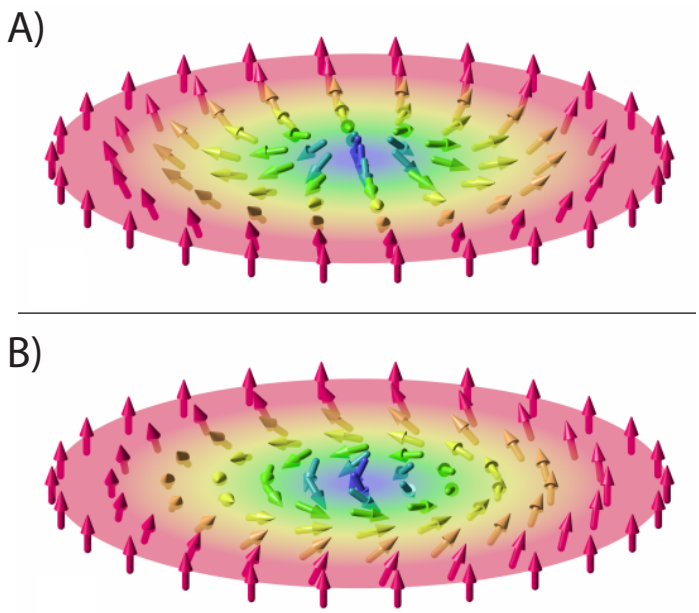

Figure 1.20. A) Néel type skyrmion structure. B) Bloch type skyrmion structure. *Adapted from Everschor-Sitte et al.* [39]

In bulk materials, the SkL structure is repeated for all crystal planes perpendicular to H. This has the effect of stretching the 2D skyrmions into long "skyrmion tubes" that pass through the entire length of the crystal in the field direction (Fig. 1.21). Since the skyrmion tubes must run parallel to H to maintain translation symmetry, the alignment of the SkL vectors is ultimately determined the by crystal directions within the plane perpendicular to H which are preferred by spin-orbit coupling [102]. As this effect is rather weak, the SkL can sometimes be forced into metastable alignments which contradict the global free energy minimum [12]. This suggests that the interaction potential of the SkL and the crystal lattice is quite sophisticated, with multiple local minima in free energy which could possibly be exploited to generate novel SkL structures. However, this interaction potential has not yet been measured. **Can we map the SkL-crystal lattice interaction potential? Can we exploit its shape to generate novel SkL configurations?**

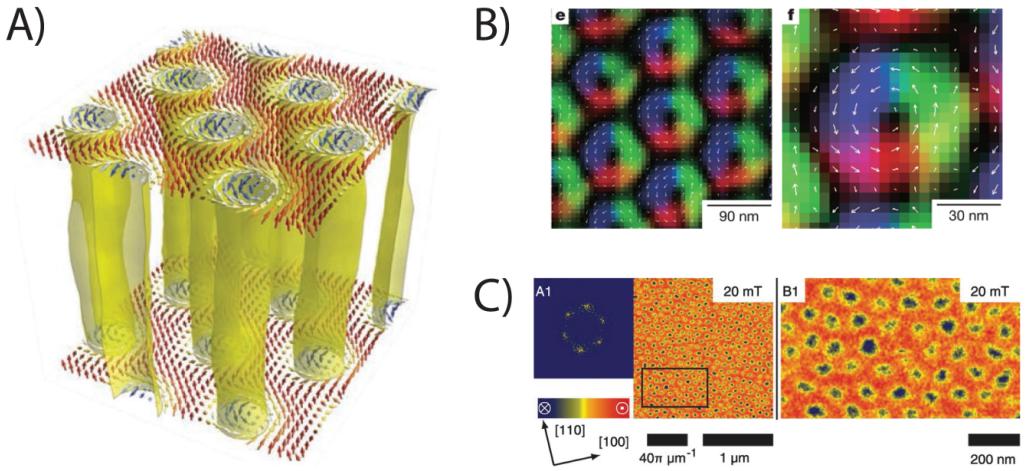

Figure 1.21. A) Cartoon of Bloch type skyrmion tubes in $Fe_{0.5}Co_{0.5}Si$. This structure can be imaged in real space via Lorentz transmission electron microscopy (LTEM) (B) and atomic force microscopy (AFM) (C). *From Milde et al.* [97] *and Yu et al.* [135].

Magnetic skyrmions have the unique property that they are topologically protected field structures. To identify structures which have this property, it is useful to define the "topological charge" S

$$S = \frac{1}{4\pi} \int \vec{n} \cdot (\frac{d\vec{n}}{dx} \times \frac{d\vec{n}}{dy}) \, dxdy \tag{1.43}$$

where $\vec{n}$ is the unit vector of magnetization $(\frac{\vec{M}}{|\vec{M}|})$ [52]. Skyrmionic structures can then be identified as those which have integer S when evaluated over the 2D magnetic unit cell, while topologically trivial structures have $S = 0$. Mathematically, no integer S structure can be continuously distorted into one with $S = 0$ (and vice versa), and so skyrmionic structures are said to be topologically protected.[15] While this is the mathematical definition of topological stability, a more physical under-

[15]For the purposes of this dissertation, "skyrmion" will always refer to a structure with $S = 1$. In principle, magnetic structures can have integer $S > 1$. These are said to have a higher "winding number" than standard skyrmions. Additionally, magnetic structures can have integers $S < 0$, and these are often described as "antiskyrmions".

standing can be gained from considering the 1D skyrmion shown in Fig 1.22. Here, we compare the magnetization profile of two, topologically trivial Néel-type domain walls (Fig 1.22.A) with that of a 1D Néel skyrmion (Fig 1.22.B). The primary difference of these two structures is that while the skyrmion magnetization winds through a full 2π of rotation, the domains only complete a rotation of π before reversing direction and rotating π the other way. If we wish to destroy either structure, we need to reverse the antiparallel spin at the center of both. For the two neighboring domain walls, this can be accomplished easily by continuously rotating the central spin clockwise until the structure disappears. On the other hand, if we try this same approach with the central spin of the skyrmion, we will eventually reach a point where we must introduce a discontinuity in the field by causing neighboring spins to "butt heads" with each other. Since this discontinuity conflicts with the intrinsic exchange stiffness of the magnetization field, forming it requires surmounting a huge energy barrier. For magnetic skyrmions, there is no formation or annihilation path that does not require surmounting this energy barrier, and so skyrmions are said to be topologically stable.

The topological energy barrier for skyrmions is predicted to be proportional to the product of the exchange constant J and the thickness of the magnetic layer d (i.e. the length of the crystal in the field direction for bulk systems) [20]. Recently, theorists have even predicted optimal thin film systems which could generate energy barriers that exceed 50 k_BT [23]. However, even for systems with smaller energy barriers, topology can still impact the behavior of the SkL. In the chiral magnet MnSi, the topological energy barrier stabilizes skyrmions that are quench-cooled well below the A Phase [104]. The resulting metastable skyrmions are so stable that they can even transition from a triangular to square lattice symmetry. Similar metastable SkLs have also been observed in $Co_8Zn_8Mn_4$ [66] and in Cu_2OSeO_3 [19]. Furthermore, in Cu_2OSeO_3 the energy barrier greatly slows the formation of the SkL upon application

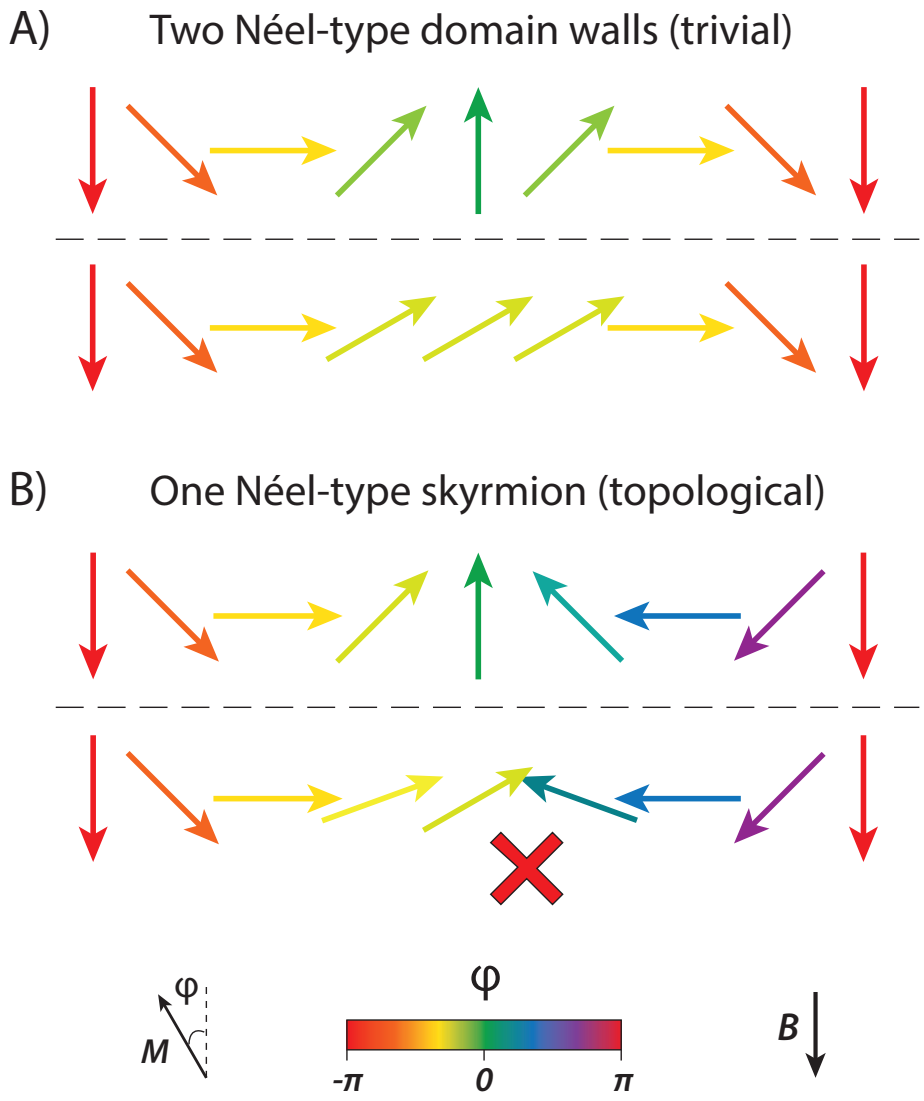

Figure 1.22. Magnetization profile of two Néel-type domain walls (A) and one Néel skyrmion (B). Color is used to indicate the orientation of the magnetization ϕ. Below each is shown the effect of continuously rotating the central spin clockwise. For the skyrmion, an energetically-unfavorable discontinuity is introduced in the magnetization field.

of an electric field. From this effect the authors were able to measure the topological energy barrier to be ∼1.6 eV/mm·skyrmion [132]. With such a large formation energy per skyrmion, it is natural to ask whether this also measurably effects the formation of equilibrium (non-metastable) SkLs. **Can we measure the formation energy of skyrmions in equilibrium systems, i.e. without relying on measuring the time-dependent decay of a non-equilibrium SkL?**

1.2.2 Applications of Skyrmions

The inherent topological stability of skyrmions make them attractive for memory applications in computers. In particular, significant research has been directed towards developing a so called "racetrack" memory (RM) devices for computation [40]. In a RM device, magnetic bits are stored linearly in a track and then pushed single file past a read/write head at a constant speed. The presence or absence of a bit in each interval of time then serves as binary 1's and 0's for computation. Unlike a conventional magnetic hard disk drive which requires the read/write head to be spun at high speed over the disk surface, RM requires no mechanically moving parts, and is only limited in computation speed by how quickly the bits can be pushed.

Since the turn of the century, IBM has dedicated efforts towards developing magnetic domain wall based RM devices and have predicted that such a device could combine the affordability of hard disk drives with speediness of solid state RAM [112]. However, in recent years skyrmions have become the favored candidates for bits in a future RM device due to their improved stability over domain walls (discussed in the previous section) and the much lower electric current densities required to move them [120][63]. Additionally, if we expand the geometry of the racetrack beyond a simple 1D chain, we open the door for entirely new paradigms of computation such as racetrack logic gates [136] and machine learning shufflers [114], further improving performance.

1.2.3 Skyrmions in Electric Currents

The most promising approach to driving skyrmions through a racetrack device is the application of a DC electric current. As electrons pass through the topologically nontrivial structure of the SkL, their spins adiabatically follow the local magnetization. This slow rotation of spin accumulates a Berry phase which can be modeled as an Aharonov-Bohm phase [6] due to an additional effective field $\vec{B}_{\text{eff}}$

$$B_{\text{eff},\,i} = \frac{\Phi_0^e}{8\pi} D_{ijk} \vec{n} \cdot (\partial_j \vec{n} \times \partial_k \vec{n}) \tag{1.44}$$

where Φ_0^e is the single-electron flux quantum $\Phi_0^e = \frac{h}{e}$ [22].[16] This field exerts an effective Lorentz force on the electrons and deflects their motion as they move through the SkL (Fig. 1.23). This deflection gives rise to an additional contribution to the Hall effect which is proportional to B_{eff} and the spin polarization of the charge carriers P (i.e. opposite spin electrons are deflected by the SkL in opposite directions, and so if both spins have equal populations ($P = 0$), the net Hall effect is zero). Observation of this "topological Hall effect" is often used as confirmation of skyrmion presence in a material, and it is anticipated that detection of skyrmions in a RM device will rely on this effect.

The deflection of spin-polarized electrons moving through the SkL exerts a opposite force on the SkL itself (Fig. 1.23) [128]. For convenience, this force is often broken down into two perpendicular components, one along the direction of current flow called the drag force F_D, and one perpendicular to the current called the Magnus force F_M. Here, the name Magnus force arises from the observation that much like a spinning baseball or soccer ball, skyrmions moving in a track experience a perpendicular force to their motion proportional to their speed [61][83]. Both the Magnus

[16] Not to be confused with the superconducting cooper pair flux quantum $\Phi_0^{sc} = \frac{h}{2e}$ which will be discussed in Chapter 1.1

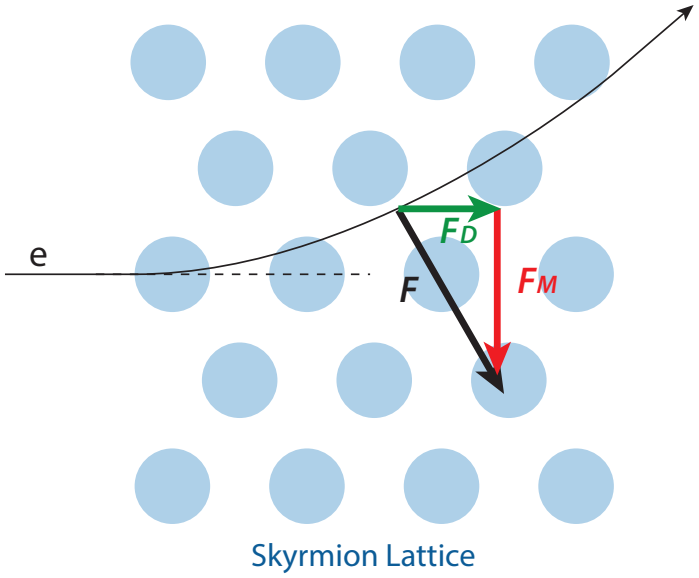

Figure 1.23. Deflection of an electron passing through a SkL due to the topological Hall effect, and the resultant force exerted on the SkL.

and drag forces are proportional to the current density passing through the SkL, and if they grow strong enough to overcome the crystal lattice couple can drive the SkL into motion. The critical current that this occurs at is often called j_c, and is routinely around $\sim 10^6$ A/m^2 for conductive B20 magnets. While this may sound like a lot of current, it is roughly two orders of magnitude less than the current required to drive magnetic domain walls [63]. **Can we find an even more efficient way to convert electric current in SkL motion?**

1.2.4 The Skyrmion Lattice of MnSi

The prototypical bulk SkL hosting material is MnSi. It is a cubic B20 crystal with lattice constant $a = 4.548$ Å[113], and its lack of inversion symmetry allows the formation of two chiral forms of the lattice (Fig. 1.24). Each unit cell contains four Mn and four Si atoms, located at positions $(u,\ u,\ u;\ \frac{1}{2}+u,\ \frac{1}{2}-u,\ \bar{u};\ \frac{1}{2}-u,\ \bar{u},\ \frac{1}{2}+u;\ \bar{u},\ \frac{1}{2}+u,\ \frac{1}{2}-u)$, with $u_{Mn} = 0.138$ and $u_{Si} = 0.845$ [56]. Each Mn

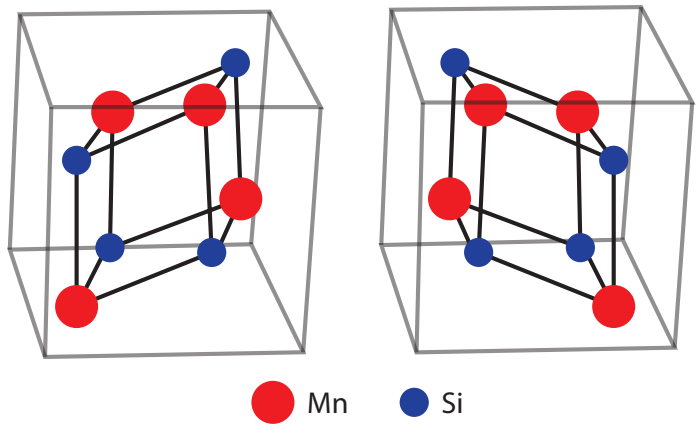

Figure 1.24. Two chiral forms of the B20 crystal structure, containing magnetic Mn and non-magnetic Si atoms. *Adapted from Stishov et al.*[126]

atom carries a magnetic moment of 0.4 μ_B, and while the Si atoms have negligible magnetic moment of their own, they serve as moderators for the superexchange which produces DMI. Since the chirality of the lattice ultimately dictates the handedness of magnetic structure [49], large single crystals of MnSi are normally grown slowly from seed crystals to ensure a single chiral phase.

In the 1970's, the magnetic phase diagram of MnSi was mapped and was confirmed to host both helical and conical phases below the magnetic ordering temperature $T_N \approx 29$ K [131]. The magnetic wavelength of these structures ($\frac{2\pi}{|\vec{Q}|}$) was found to be ∼180 Å. Additionally, both ultrasound absorption [75] and electron spin resonance [31] measurements detected the presence of another phase roughly 1 K below T_N and at $\sim$ 0.2 T applied field (Fig. 1.25). This phase was called the "Anomalous phase" or "A phase" for short. Small angle neutron scattering (SANS) measurements attempted to explain this phase as a small paramagnetic phase nesting within the conical phase [55]. However, further SANS measurements later confirmed the formation of a crystallized lattice of skyrmions within the A Phase [102]. These skyrmions were translationally symmetric along the applied field direction and therefore stretched into long tubes that extend through the entire length of the crystal.

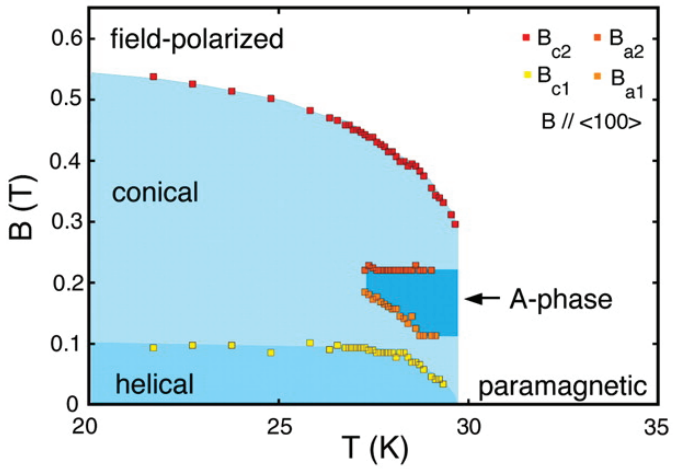

Figure 1.25. Magnetic phase diagram of MnSi. *From Mühlbauer et al.*[102]

Each skyrmion was found to carry a topological charge $S = 1$, with a single spin oriented antiparallel to the applied field at the center of the skyrmion. Theoretical modelling showed that the free energy of the SkL configuration was very close to that of the conical phase at the relevant fields, and the addition of thermal fluctuations allows the SkL to drop lower in energy [102]. This reliance on fluctuations explains why the SkL is the preferred structure only very near to T_N, however quench cooling through the A Phase has generated metastable skyrmions at a much wider range of temperatures [104].

As it was the first discovered, the SkL of MnSi has been used as a model system to observe many interesting properties of skyrmions and their lattices. Previously, we have discussed the metastable SkLs [104] and SkL orientations [12] that can be produced in MnSi. Other studies have shown that the A Phase can be tuned through the application of uniaxial strain [105][25] or hydrostatic pressure [14]. The A Phase can also be expanded by reducing the dimensionality of the MnSi crystal, both down to 2D in a thin film [129] and 1D in a nanowire [134]. Finally, some work has shown

that the SkL phase can be expanded by reducing the Mn availability during crystallization [110]. However, despite all this, measuring the topological energy barrier for skyrmions in MnSi has remained elusive, largely because the time dependent effects exploited in insulating SkL materials are not suitable for a metal like MnSi. **What is the topological energy barrier of MnSi?**

CHAPTER 2

SMALL ANGLE NEUTRON SCATTERING

Small angle neutron scattering (SANS) is a fundamental technique for studying structures of order 10's - 100's of nanometers in size in a wide variety of disciplines, from biology to material science. In this chapter I will begin by providing a brief introduction to the fundamentals of scattering and motivate why a neutron scattering technique is useful for the study magnetic vortices. Then I will summarize some of the more technical details of how SANS is achieved experimentally. Finally, I will introduce the common types of SANS measurements used to study magnetic vortices in this dissertation.

Fundamental scattering theory in this chapter is based on the relevant chapters from Simon [122], Kittel [69], and Ashcroft [9]. For a fantastic introduction into neutron scattering in particular, please check out Pynn [115]. Finally, for a detailed review of the application of SANS to magnetic systems, please read Mühlbauer *et al.* [100].

2.1 Introduction to Scattering

One of the most useful methods to study condensed matter is to measure how a wave deflects from it in a process called "scattering." Since quantum mechanics dictates that any particle with momentum p will demonstrate wave-like behavior with a de Broglie wavelength $\lambda = h/p$, these waves can be photons or massive particles. Generally, scattering measures a change of the incident waves momentum, from its initial state $\vec{k_i}$ to its final state $\vec{k_f}$ due to some interaction with the target material

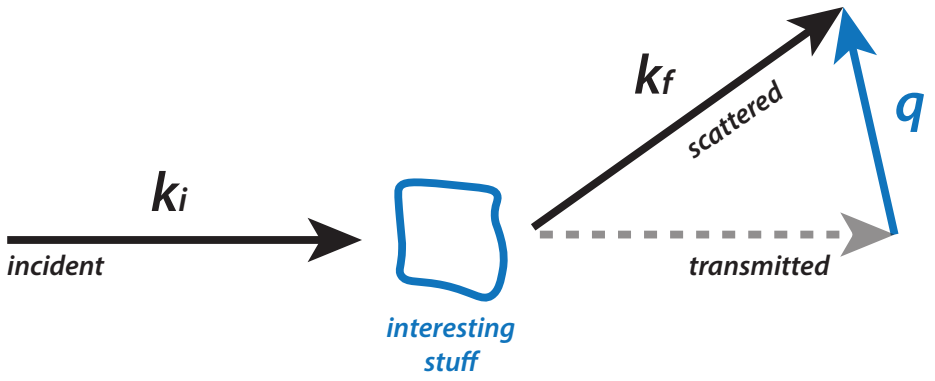

Figure 2.1. General scattering of a particle-wave from $\vec{k_i}$ to $\vec{k_f}$ due to interaction with the target.

(Fig. 2.1). This interaction is quantified by the interaction potential $\hat{V}(\vec{r})$, and therefore we can write down the transition rate $\Gamma_{(i,f)}$ from $\vec{k_i}$ to $\vec{k_f}$ following Fermi's Golden Rule

$$\Gamma_{(i,f)} = \frac{2\pi}{\hbar} | < \vec{k_f} | \hat{V}(\vec{r}) | \vec{k_i} > |^2 \ \rho(\vec{k_f}) \tag{2.1}$$

where $\rho(\vec{k_f})$ is the density of states of the outgoing wave. If we assume that both the incoming and outgoing waves are plane waves, then the matrix element can be computed as the integral

$$\begin{aligned} < \vec{k_f} | \hat{V}(\vec{r}) | \vec{k_i} > &= \int A^* e^{-i\vec{k_f}\cdot\vec{r}} \ V(\vec{r}) \ A \ e^{i\vec{k_i}\cdot\vec{r}} d\vec{r} \\ &= |A|^2 \int e^{-i(\vec{k_f}-\vec{k_i})\cdot\vec{r}} \ V(\vec{r}) d\vec{r} \end{aligned} \tag{2.2}$$

where A is the normalization factor of the plane waves. At this point, it useful to introduce the "scattering vector" $\vec{q} \equiv \vec{k_f} - \vec{k_i}$ which measures the change in the wavevector of the scattered particle.

$$< \vec{k_f} | \hat{V}(\vec{r}) | \vec{k_i} > = |A|^2 \int e^{-i\vec{q}\cdot\vec{r}} \ V(\vec{r}) d\vec{r} \tag{2.3}$$

In the special case where V is periodic throughout the material (i.e. $V(\vec{r}) = V(\vec{r}+\vec{R})$ where $\vec{R}$ is any lattice vector), this integral can be performed over each unit cell separately

$$\begin{aligned} < \vec{k_f}|\hat{V}(\vec{r})|\vec{k_i} > &= |A|^2 \sum_{\vec{R}} \int_{cell} e^{-i\vec{q}\cdot(\vec{r}+\vec{R})}\ V(\vec{r}+\vec{R})d\vec{r} \\ &= |A|^2 \sum_{\vec{R}} \int_{cell} e^{-i\vec{q}\cdot\vec{r}} e^{-i\vec{q}\cdot\vec{R}}\ V(\vec{r})d\vec{r} \\ &= |A|^2 [\sum_{\vec{R}} e^{-i\vec{q}\cdot\vec{R}}]\ [\int_{cell} e^{-i\vec{q}\cdot\vec{r}}\ V(\vec{r})d\vec{r}] \end{aligned} \tag{2.4}$$

The first term in brackets here is defined as the "structure factor" $S(\vec{q},\vec{R})$, and it contains all information regarding the periodicity of the lattice.

$$S(\vec{q},\vec{R}) \equiv \sum_{\vec{R}} e^{-i\vec{q}\cdot\vec{R}} \tag{2.5}$$

The second term in brackets is named the "form factor" $F(\vec{q},V(\vec{r}))$ and contains all information regarding the physical interaction of the scattered particle with the material.

$$F(\vec{q},V(\vec{r})) \equiv \int_{cell} e^{-i\vec{q}\cdot\vec{r}}\ V(\vec{r})d\vec{r} \tag{2.6}$$

2.1.1 Elastic Scattering

In the special case that scattered particle exchanges no energy with the target ($E_i = E_f$ and therefore $|k_i| = |k_f|$), the scattering process is said to be "elastic". It can be shown that the structure factor for elastic scattering is only nonzero when the scattering vector $\vec{q}$ coincides with a reciprocal lattice vector $\vec{G}$ of the real space lattice $\vec{R}$.

$$\vec{k_f} - \vec{k_i} = \vec{q} = \vec{G} \tag{2.7}$$

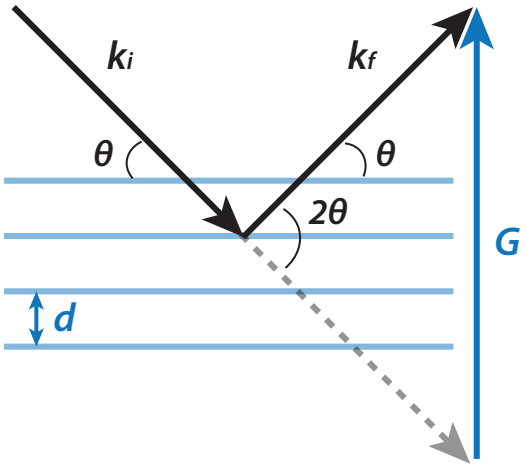

Figure 2.2. Elastic scattering of a wave from periodic symmetry planes.

This is known as the Laue condition, and it allows us to predict the discrete set of elastic reflections that will occur for any periodic structure. To get a feel for the implications of this, let us consider a plane wave with wavevector $\vec{k}$ incident at an angle θ to a set of symmetry planes with reciprocal lattice vector $\vec{G}$ (Fig. 2.2). Using some simple geometry, we find:

$$\vec{k_f} - \vec{k_i} = \vec{G} \tag{2.8}$$

$$\vec{k_{f_y}} - \vec{k_{iy}} = \vec{G}_y \tag{2.9}$$

$$|k| \sin\theta - (-|k| \sin\theta) = |G| \tag{2.10}$$

$$2|k| \sin\theta = |G| \tag{2.11}$$

By definition, the magnitude of G is given by the spacing of the symmetry planes $|G| = 2\pi/d$, and the magnitude of the wavevector is given by wavelength $|k| = 2\pi/\lambda$,

so we find

$$2\frac{\sin\theta}{\lambda} = \frac{1}{d} \tag{2.12}$$

$$2d\sin\theta = \lambda \tag{2.13}$$

This is of course Bragg's Law[1], and so the Laue and Bragg formalisms of elastic scattering are consistent and predict the same scattering angles 2θ.

The Laue condition allows us to simplify our definition of the form factor if we consider only those q's which will produce reflections.

$$F(\vec{G}, V(\vec{r})) \equiv \int_{cell} e^{-i\vec{G}\cdot\vec{r}}\, V(\vec{r})d\vec{r} \tag{2.14}$$

From here, it is clear that the form factor represents (and in fact by definition is) a Fourier transform of the interaction potential $V(\vec{r})$. Therefore, by measuring the form factor experimentally, insights can be gained into the interior structure of the unit cell.

2.1.1.1 The Ewald Sphere

A useful tool for visualizing elastic scattering is "Ewald's sphere" (Fig. 2.3). In this construction, the incident wavevector $\vec{k_i}$ is placed in reciprocal space with its head starting at a point in the reciprocal lattice. All potential elastically scattered $\vec{k_f}$'s will have the same length and can therefore can be represented as a sphere centered at the tail of $\vec{k_i}$. However, due to the Laue condition, scattering will only occur if the surface of this sphere intersects a second point in the reciprocal lattice so that $\vec{k_f} - \vec{k_i} = \vec{G}$ (Fig. 2.3).

The Ewald sphere is particularly helpful in understanding the different types of

[1]For the case of first order reflections (n=1). Considering integer multiples of $\vec{G}$ allows to find the higher nth order reflections

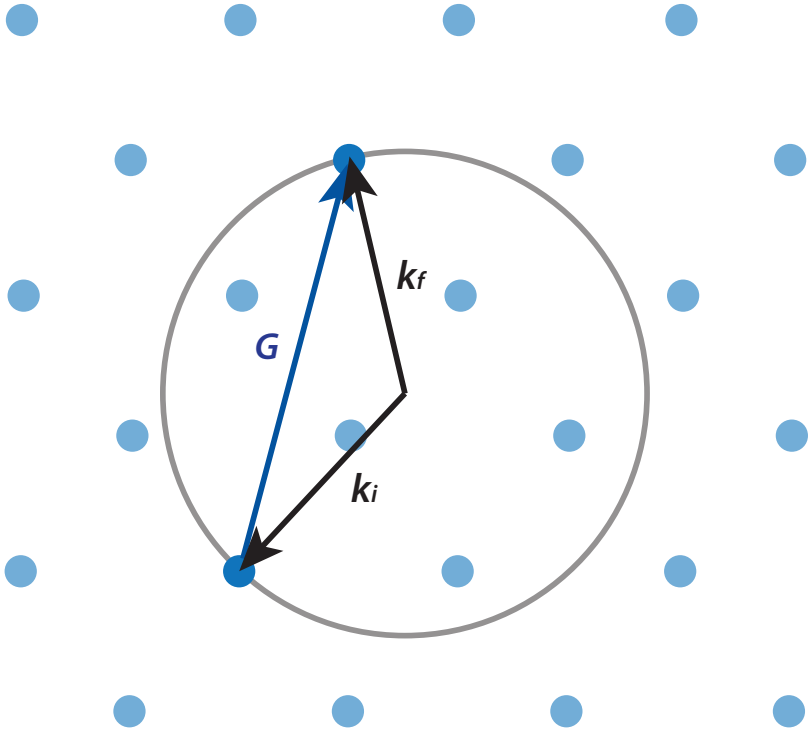

Figure 2.3. Ewald's sphere of elastic scattering. Each dot is a point in the reciprocal lattice. The sphere is drawn as a 2D circle for clarity, but in principle it extends into three dimensions.

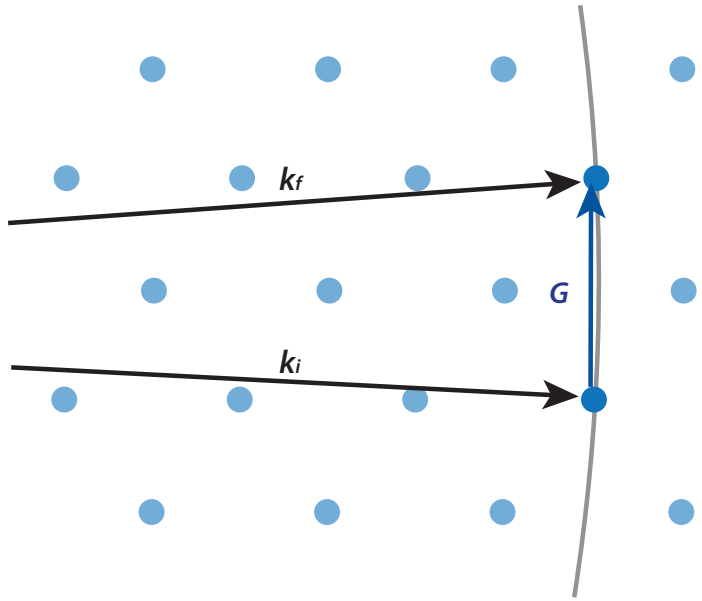

Figure 2.4. Ewald's sphere for small-angle scattering. The center of the sphere is far to the left of the figure.

scattering experiments commonly performed. One way to map reciprocal space is to measure the scattered intensity while rotating the sample with respect to the beam, as is done with single crystal x-ray diffraction. This is equivalent to changing the incident vector $\vec{k_i}$, so the Ewald sphere will rotate about the head of $\vec{k_i}$, with different symmetry planes producing a scattering signal as the sphere sweeps through the corresponding lattice point in reciprocal space. An alternative approach, called Laue white-beam scattering, is to shine a wide range of wavelengths onto the sample rather than a monochromatic beam. This forms a continuum of Ewald spheres with a range of radii, allowing many Bragg peaks to be illuminated at once. One final example that is of direct interest to this dissertation is small angle scattering, where $\theta \ll 1$ radian. In this limit the radius of the sphere is much larger than the spacing of the reciprocal lattice since $|\vec{k}| \gg |\vec{q}|$. From the perspective of any lattice point, the surface of sphere can be well approximated as a plane that rotates to stay perpendicular with $\vec{k_i}$ (Fig. 2.4).

2.1.2 Neutrons Scattering from Magnetic Order

To carry our discussion of scattering further, we must get more specific about both the type of wave we are scattering and how it interacts with the target material ($V(\vec{r})$). Since we are interested in studying magnetic structures (Chapters 1.1 and 1.2), a natural choice of particle-wave is the neutron. Neutrons have an intrinsic magnetic dipole moment that allows them to couple with the local magnetization in a material, while their neutral charge allows them to avoid interacting with electrons.

Neutrons scatter via predominantly two mechanisms in a material: strong-force scattering with the nuclei, and magnetic scattering from the local magnetic field $\vec{B}$. Nuclear scattering enables neutrons to study crystal structure much like x-rays, but with the advantage that the strength of the scattering signal is not dictated by merely the number of electrons the target atom has, but rather the magnitude of the strong force coupling with the nuclei. This short-range interaction potential is normally modelled as a Dirac delta function for each atom i within the unit cell:

$$V_{nuc}(\vec{r}) \propto \sum_i b_i(Z,N)\ \delta(\vec{r}-\vec{r_i}) \tag{2.15}$$

Here, b_i is called the "nuclear scattering length", and it measures the strength of the coupling between the neutron and the nucleus. Since the strength of the strong force coupling depends on the complex inner workings of the nucleus, b is a function of both atomic number and isotope, and can be either positive or negative. This allows neutrons to scatter strongly from some elements that are too light to study with x-rays. Additionally, the background scattering can often be reduced through isotopic enrichment and/ or through scattering length contrast matching.

More relevant to this dissertation is how neutrons can also scatter from magnetic order in materials. Assuming a dipolar interaction with the local field, this interaction

takes the form

$$V_{mag}(\vec{r}) = -\mu_n \gamma B(\vec{r}) \tag{2.16}$$

where $\mu_n = e\hbar/2m_p$ is the neutron magnetic moment and γ is the gyromagnetic ratio. Plugging this into Equation 2.14, it is clear that the form factor for magnetic dipole scattering is simply a Fourier transform of the local field $B(\vec{r})$.

$$F(\vec{G}, B(\vec{r})) = -\mu_n \gamma \int_{cell} e^{-i\vec{G}\cdot\vec{r}}\, B(\vec{r}) d\vec{r} \tag{2.17}$$

Since the field B is a function of the local magnetization M, the scattering signal contains information about the microscopic magnetic structure of the target. As the scattering signal is summed over the entire illuminated sample volume, neutron scattering provides a true probe of the magnetic properties of the bulk of the sample, rather than being limited to the surface like microscopy. This makes neutron scattering a powerful tool for studying periodic magnetic order like vortices.

2.1.3 Neutron Scattering from Magnetic Vortices

Combining everything that we have discussed so far, it is possible to predict the scattering signal that should be expected from a periodic magnetic vortex lattice, such as a SkL or a VL. Since any real world neutron detector has finite size, it is impossible to measure the scattering rate of a transition $\Gamma_{(i,f)}$ independently from all other $\Gamma_{(i,f')}$s with similar scattering angles. Therefore we must introduce the measurable quantity of the scattering "cross section", which sums over all scattering rates within a given solid angle Ω. In the limit that the solid angle is infinitesimally small, we end up with the differential cross section $\frac{d\Sigma}{d\Omega}$, which by definition is normalized to the neutron flux

incident on the sample ϕ_n.

$$\frac{d\Sigma}{d\Omega} = \frac{1}{\phi_n} \sum_{\vec{k_f} \in d\Omega} \Gamma_{(i,f)} \tag{2.18}$$

Combining this expression with Equations 2.1, 2.4, and 2.17, we find the magnetic scattering differential cross section:

$$\frac{d\Sigma}{d\Omega} = \frac{1}{\phi_n} \frac{2\pi}{\hbar} |A|^2 |S(\vec{q}, \vec{R})|^2 |F(\vec{q}, B(\vec{r})|^2 \tag{2.19}$$

From here, by using a proper normalization for the plane waves, and going through loads of algebra, we can find a final form of the cross section

$$\left(\frac{d\Sigma}{d\Omega}\right)_{\text{vortex}} = (2\pi)^3 (\frac{\gamma}{4\Phi_0})^2 V_{\text{sample}} \sum_{\vec{G}} \delta(\vec{q} - \vec{G}) [\frac{1}{\Phi_0 t} \int_{cell} e^{-i\vec{q}\cdot\vec{r}} B(\vec{r}) d\vec{r}]^2 \tag{2.20}$$

where Φ_0 is the flux quantum for the relevant vortex (i.e. Φ_0^{sc} for VLs and Φ_0^e for SkLs). In this expression, the Laue condition of elastic scattering has been added explicitly in the form of the Dirac delta function.

2.1.4 Small Angle Scattering

So far, we have discussed neutron scattering from magnetic vortices as if it is a straightforward diffraction experiment. However, in practice, the de Broglie wavelength of neutrons from any user facility is much smaller than the lattice constant of VLs/ SkLs ($\lambda \sim$0.5 nm vs $d \sim$50 nm). Applying the condition that $\lambda \ll d$ to Braggs Law

$$\frac{\lambda}{2d} = \sin\theta \ll 1 \tag{2.21}$$

reveals that the first order reflections must occur at very small θ. In the small angle limit, Bragg's law can be simplified even further by approximating $\sin\theta \approx \theta$.

$$\frac{\lambda}{2d} = \theta \tag{2.22}$$

Since the scattered beam lies only a few degrees from the transmitted beam, small angle scattering poses experimental challenges that are unique amongst scattering techniques. For this reason, neutron scattering facilities construct beamlines solely to address these challenges and perform precise small angle neutron scattering (SANS) (Fig. 2.5). The following section covers the experimental techniques used to achieve this feat.

2.2 Experimental Details

From Bragg's Law we can get a clear picture of the experimental requirements to measure SANS from nanoscale structures. First, if we assume that we are experimentally capable of resolving a minimum scattering angle $\theta = 1^\circ$ from the unscattered beam, then the de Broglie wavelength of our incoming neutrons (λ) needs to be at least 1% of the size of structures we are interested in studying d. For structures in the ballpark of 50 nm, this means we will need to produce neutron wavelengths of

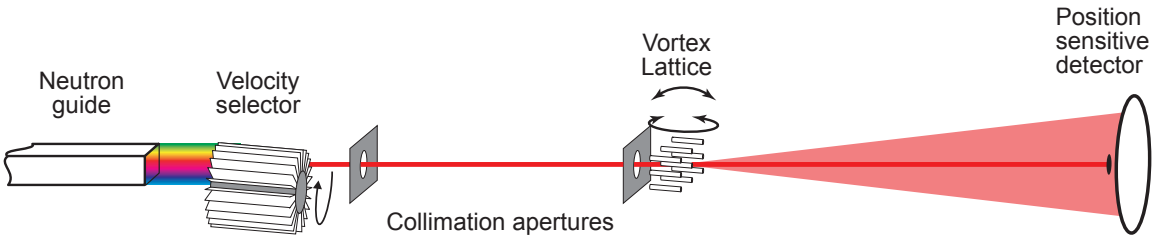

Figure 2.5. Magnetic SANS schematic *From M.R. Eskildsen*[35]

order $\lambda = 5$ Å.

2.2.1 Cold Neutron Production

Since free neutrons naturally decay into protons in roughly 10 minutes, neutrons to be used for scattering must be continuously produced for user operation. There are two types of experimental facility that can produce high enough quantities of neutrons to be suitable for scattering applications: nuclear fission reactors and particle accelerators.

Fissionable elements are able to maintain a chain reaction because the splitting of each nucleus releases energetic neutrons which can go on to trigger another fission event elsewhere. When a fission reactor is operating in a state of criticality, each fission event triggers exactly one more fission event, so the power output remains constant. However, fission of Uranium-235 produces on average three free neutrons per event, and so these additional two neutrons must either be absorbed or directed elsewhere to maintain criticality. These extra neutrons are exploited in a reactor-based neutron source by adding an opening to the reactor to allow some of the neutrons to escape. Neutron moderation will be discussed in further detail later.

Accelerator based sources operate by first producing a beam of protons that can then be accelerated to high energies (∼500 MeV) via a cyclotron. This beam is directed into a target made of a heavy, neutron-rich element like mercury or lead, and the collision of the high energy protons with the heavy elements splits the nuclei and produces a cascade of smaller elements through a process called spallation. Among these fission products are many neutrons that can be used for scattering. Spallation neutron sources often do not produce as many total neutrons per second as fission reactor sources. However, many spallation sources are "pulsed" sources which means the proton beam (and therefore the resulting neutron beam) is produced in short[2],

[2]Normally on the order of microseconds in length.

high intensity bursts. By producing these pulses of neutrons periodically, the different wavelengths of neutrons can be separated by time of flight to the detector, and so a wider range of the beam can be used simultaneously for measurement. Alternatively, in monochromatic mode, high speed time-dependent measurements are possible.

Both fission and spallation produce very high energy neutrons, and so to reach our desired wavelength of 5 Å we must dramatically reduce the energy of these neutrons. This is accomplished through "moderation", which is the process of allowing high energy neutrons to collide with other particles to give off energy. The first stage of moderation occurs inside the reactor/ spallation source itself as the neutrons thermalize with the water (or heavy water) moderator. This process continues until the neutrons are in thermal equilibrium with the water ($\sim$ 290 K), producing "thermal neutrons". These neutrons have wavelength of order 1 Å, and so for SANS we must cool the neutrons even further. To achieve this a second moderator, called a "cold source" ($\sim$ 20 K) is installed at the beginning of the SANS beamline. The cold source contains a light cryogenic liquid, often liquid hydrogen, which further cools the neutrons down to a kinetic energy of roughly 5 meV. This is the "cold neutron" regime, and cold neutrons have wavelengths precisely in the 5-10 Å range that we are interested in. The resulting wavelength distributions due to thermal and cold neutron moderation are shown in Fig. 2.6.

2.2.2 Guiding the Neutrons

After leaving the cold source, the neutrons enter an evacuated tube called a neutron guide. While neutrons are harder to "steer" than photons in many regards, the different neutron scattering lengths of various materials does produce an effective index of refraction for neutrons than can be exploited for some limited optics. The inside of the neutron guide is lined with a material with a particularly high scattering length so that neutrons incident at shallow angles will be almost entirely reflected,

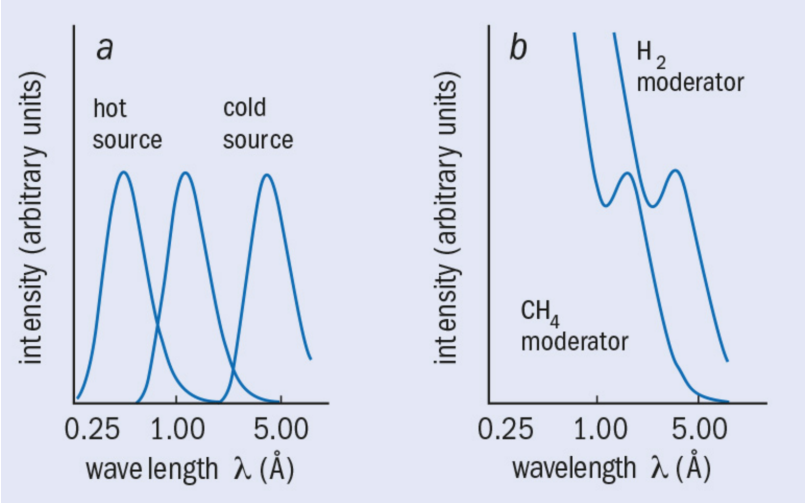

Figure 2.6. A) Distribution of neutron wavelength due to hot, thermal, and cold neutron moderators. B) The combined distribution due to all three levels of moderation, for a liquid methane cold source ($\sim$ 100 K), and liquid hydrogen cold source ($\sim$ 20 K). *From J. Finney* [42].

producing total internal reflection within the guide. This effect allows the guides to slowly bend as they move away from the reactor/ spallation target with very little loss of total cold neutron flux. Curving the beamline isolates the cold neutrons from other particles leaving the reactor (mainly gamma rays) by eliminating line of sight to the cold source, and therefore protects the detector at the end of the beamline from being overwhelmed with radiation.

2.2.3 Wavelength Selection

The next step in SANS is to isolate a narrow band of neutron wavelengths so that we can perform monochromatic Bragg scattering. Fortunately, since neutrons are massive particles, their de Broglie wavelength is directly related to their speed v:

$$\lambda = \frac{h}{p} = \frac{h}{mv} \tag{2.23}$$

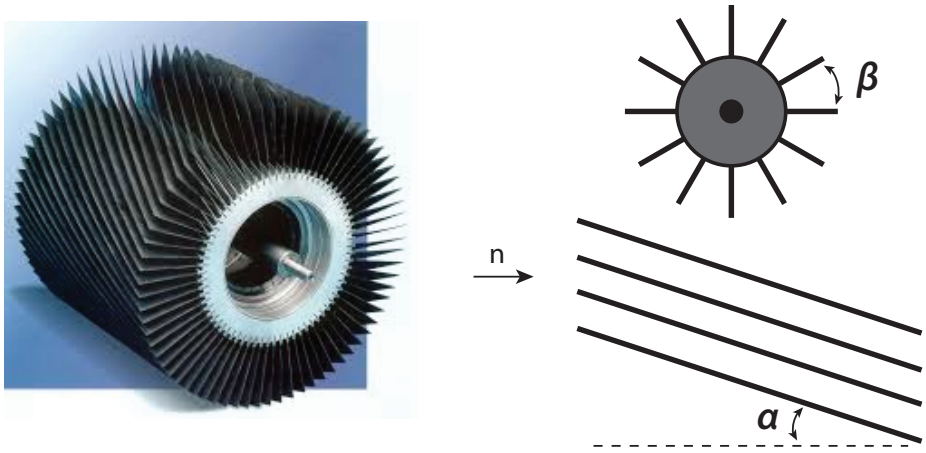

Figure 2.7. Neutron velocity selector. *From EADS Astrium.*[1]

An efficient method to isolate neutrons based on this speed is to use a neutron "velocity selector". The velocity selector is a simple device consisting of many thin fins of neutron absorbing material wrapped in a helix pattern around a central axle (Fig. 2.7). This drum is then spun at high frequency such that only neutrons of a particular speed can pass through the device without colliding into one of the fins. Resolution of a velocity selector is typically measured in "wavelength spread" $\frac{\Delta\lambda}{\lambda}$, where $\Delta\lambda$ is the full-width, half-maximum (FWHM) of the resulting wavelength distribution. Wavelength spread is chosen in particular because it does not depend on wavelength or the speed of the drum, only on geometric parameters of the velocity selector itself. Specifically

$$\frac{\Delta\lambda}{\lambda} = \frac{\beta}{\alpha} \tag{2.24}$$

where α is the pitch angle of the helical fins and β is the angular fin spacing. Typical values of $\frac{\Delta\lambda}{\lambda}$ are around 10%, although this can be increased to increase neutron flux.

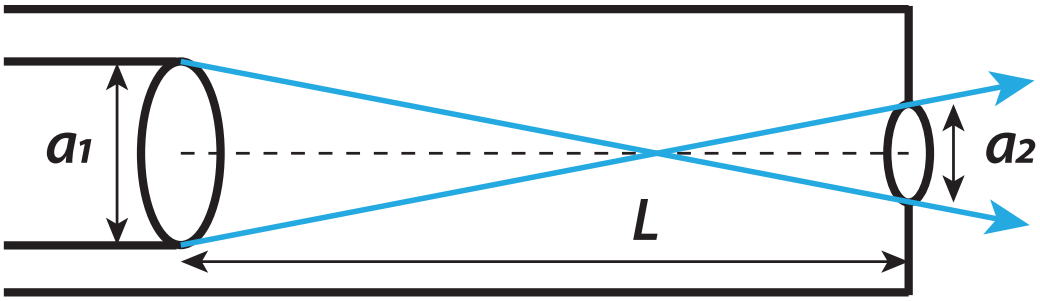

Figure 2.8. Neutron collimation through two pin holes (not to scale). The maximal angular spread of the neutron beam is shown in blue.

2.2.4 Collimation

After producing a monochromatic beam neutrons, it is now important to collimate the beam to ensure that our incoming beam has a well defined incident angle. Since neutrons cannot be steered easily with optics like a photon might be, collimating the beam once again relies on absorbing all neutrons that that do not meet our requirements. In particular, the beam is passed through two apertures in a neutron absorbing material that are placed meters apart from each other (Fig. 2.8). By reducing the size of the apertures (a_1, a_2) and increasing their separation (L), the collimation of the beam can be increased at the cost of neutron flux. The first aperture the neutrons encounter is naturally referred to as the "source aperture" while the second is called the "sample aperture". In practice, the source aperture is normally the inner diameter of the neutron guide leaving the velocity selector, and the separation L is controlled by how far this guide extends into a wider region of beamline. This has the advantage of keeping the sample aperture fixed so that the sample space and detector do not need to move.

2.2.5 Sample Environment

SANS facilities are equipped to provide a wide variety of sample environments corresponding to the many fields of study that regularly use SANS. Of particular relevance to this dissertation are cryomagnets, as both SkLs and VLs require low temperatures and magnetic fields to form. To be used with neutron scattering, cryomagnets must be equipped with special windows which minimize background scattering. This is particularly challenging for SANS as potential window materials must avoid both nuclear Bragg peaks from crystalline order, and small angle scattering from large scale order. For these reasons, single crystal sapphire (Al_2O_3) or silicon windows are normally used for SANS as their constituent elements have very low neutron scattering cross sections and their crystallinity prevents scattering from grains. Similar considerations must also be made in selecting a substrate to hold the sample in the beam, and for all experiments discussed in this dissertation we have used a sapphire substrate for its low SANS background and high thermal conductivity.

If studying an anisotropic magnetic structure it is critical that the cryomagnet be installed on a rotation stage so that the incident neutron angle can be changed relative to the field. For periodic structures where Bragg diffraction is produced (like SkLs and VLs), rotations must be possible in both axes which are orthogonal to the neutron beam so that sample can be rotated arbitrarily through reciprocal space until the Bragg condition is satisfied. Though not essential, it also often useful for the entire cryostat/ rotation assembly to be installed on a 3 axis translation stage so that the sample can be easily moved into the center of the neutron beam.

2.2.6 Detecting Neutrons

The final hurdle in measuring SANS is detecting the scattered neutrons in a spatially (and sometimes temporally) resolved fashion. This is trickier than detecting other forms of ionizing radiation as neutrons lack electric charge, so their presence

must be detected through daughter products of their interaction with matter. Due to its very high neutron absorption cross section, helium-3 is the usual choice as a converter gas for neutron detection. Absorbing a neutron converts the helium-3 to hydrogen-3 and releases a proton in the following reaction:

$$\mathrm{n} + {}^{3}\mathrm{He} \longrightarrow {}^{3}\mathrm{H}^{-} + \mathrm{p}^{+} + 0.764 \ \mathrm{MeV} \tag{2.25}$$

These daughter products carry roughly 0.7 MeV of kinetic energy and go on to produce a cloud of ionized particles which can be detected as a current pulse across the high voltage of a Geiger counter or similar detector. In order to spatially determine where a neutron is detected, the neutron detectors are arranged in an array. If the detectors are small enough, each detector can be one pixel in the array. However, another common solution is to use long tube detectors which span one dimension of the array. In order to determine how far along the length of the tube a neutron is detected, the current pulse is measured from both ends and the difference of pulse arrival time indicates how close the neutron was to each end.

Standard pixel size for a neutron detector is around 1 cm, so to resolve the small scattering angles necessary for SANS the detector must be moved tens of meters away from the sample. In order to avoid secondary scattering from air molecules, the detector array is placed at the back of an evacuated tank. Within this tank, the detector array is placed on rails which allow it to be driven closer or further away from the detector depending on the desired scattering angle range. On these same tracks a small neutron absorbing "beam stop" is placed in front the detector at the center of incident beam to shield the detector from the bright, un-scattered neutron beam (as well as any other unwanted radiation that has made it this far).

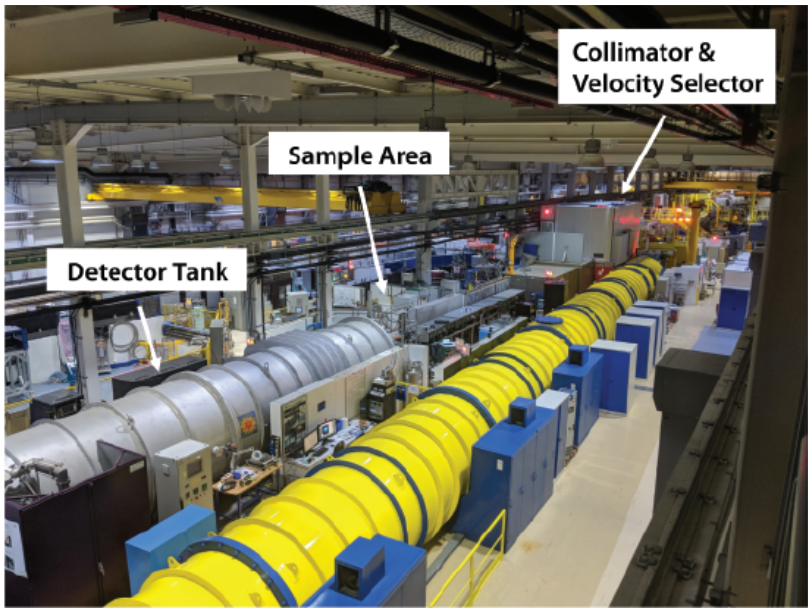

Figure 2.9. D33 and D22 SANS beamlines at the Institut Laue Langevin. The large cylinders are the evacuated detector tanks of the two beamlines. The reactor sits behind the far wall in the distance.

2.2.7 SANS Resolution

SANS, like all experimental techniques, has its own resolution limits. Since wavelength selection and beam collimation both rely "throwing away" neutrons that do not meet set criteria, neither can be achieved perfectly without eliminating all usuable neutron flux. Therefore, the finite resolution of these two steps contribute most heavily to the resolution of SANS. Additionally, as discussed before, cold neutron detectors have finite pixel size on the order of a few mm up to a cm. However, as long as measurements are performed on truly small angle (low q) systems and the detector is positioned towards the back of the detector tank, this pixel size is normally negligible compared to the size of the Bragg peak produced from resolution limits upstream. For a full derivation of the following expressions, please consult the dissertation of P. Harris [50].

2.2.7.1 Wavelength Resolution

As mentioned previously, velocity selectors are designed to have a fixed wavelength spread $\frac{\Delta\lambda}{\lambda}$ independent of the selected wavelength. From Bragg's Law in the small angle θ limit:

$$2\theta = \frac{\lambda}{d} = \frac{q\lambda}{2\pi} \tag{2.26}$$

Working from here, it is possible to derive the resolution limit due to wavelength spread:

$$\Delta_{2\theta}(\lambda, \frac{\Delta\lambda}{\lambda}) = \frac{q\lambda}{4\pi}\sqrt{\frac{4\ln 2}{3}}\frac{\Delta\lambda}{\lambda} \tag{2.27}$$

Here, the resolution is expressed as the full width at half maximum (FWHM) $\Delta_{2\theta}$, which introduces the $\sqrt{\ln 2}$-related coefficients.

2.2.7.2 Collimation Resolution

As shown in Figure 2.8, the two pinhole collimation approach allows a finite angular spread of neutrons to continue onto the sample. The resolution of this approach is a function of the pinhole sizes a_1 and a_2, as well as their separation L.

$$\Delta_{2\theta}(a_1, a_2, L) = \frac{1}{2}\sqrt{2\ln 2}\sqrt{(\frac{a_1}{L})^2 + (\frac{a_2}{L})^2} \tag{2.28}$$

2.2.7.3 Resolution of $\vec{q}$

It is important to note here that while the spread of wavelengths impacts the outgoing scattering angle θ, the spread of neutron collimation impacts the incoming neutron vector $\vec{k_i}$. This limits resolution in both the scattering angle θ and the azimuthal angle ϕ, since $\vec{k_i}$ is uncertain in both directions. Assuming these resolution limits are Gaussian in nature and act independently, we can add them in quadrature to determine the resolution limit of $\vec{q}$ in all three directions in reciprocal space (shown

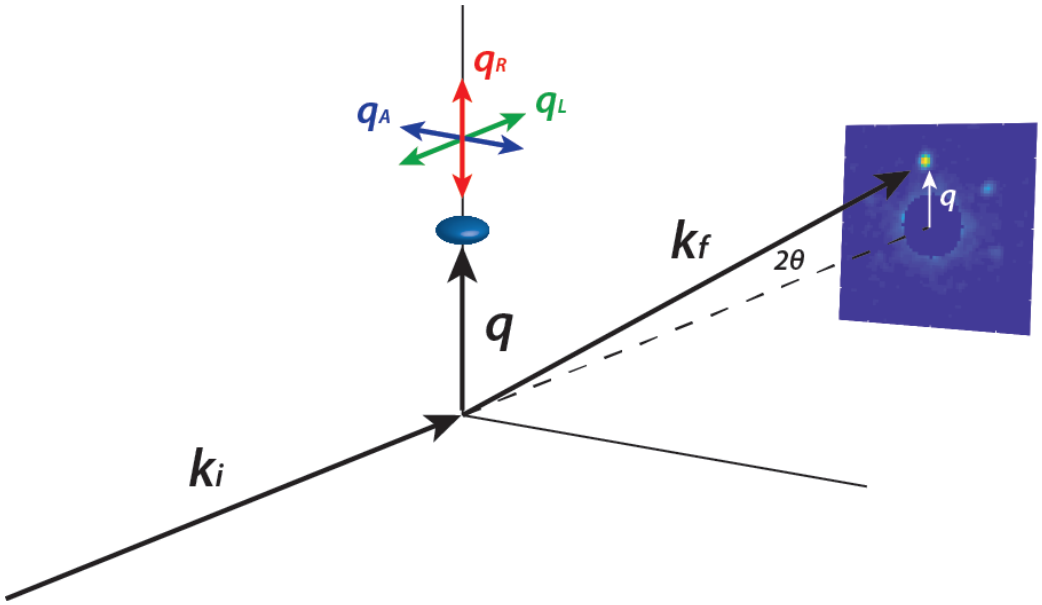

Figure 2.10. Uncertainty of the reflected $\vec{q}$ in three directions of reciprocal space, indicated by the finite dimensions of the ellipsoid. Wavelength spread broadens the uncertainty in q_R and q_L, while collimation spread broadens the uncertainty on q_R, q_L, and q_A.

in Fig 2.10): radially,

$$\Delta q_R = \sqrt{[k\Delta_{2\theta}(\lambda, \frac{\Delta\lambda}{\lambda})]^2 + [k\Delta_{2\theta}(a_1, a_2, L)]^2} \tag{2.29}$$

azimuthally,

$$\Delta q_A = \sqrt{[k\Delta_{2\theta}(a_1, a_2, L)]^2} \tag{2.30}$$

and longitudinally.

$$\Delta q_L = \sqrt{[q\Delta_{2\theta}(\lambda, \frac{\Delta\lambda}{\lambda})]^2 + [q\Delta_{2\theta}(a_1, a_2, L)]^2} \tag{2.31}$$

Comparing these equations, it is clear that the longitudinal resolution for SANS (Δq_L) will be much better than along the other directions, as by definition $q \ll k$ in small angle scattering. For this reason, it is best practice to align the neutron beam

along the axis of magnetic order that you are most interested in studying with SANS.

2.3 SANS on Magnetic Vortices

As discussed previously, SANS is an ideal tool for studying the bulk properties of large scale magnetic order. For SkLs, the periodicity of the helimagnetic precession Q directly leads to the scattering vector magnitude $q = Q$. In VLs, since the density of vortices is a function of magnetic field, so too is the scattering vector. In the case of square VLs, the largest spacing symmetry planes (and therefore the lowest q Bragg peaks) lie perpendicular to the [100] vectors, so

$$q_0^{sqr} = \frac{2\pi}{a_0^{sqr}} = 2\pi\sqrt{\frac{\mu_0 H}{\Phi_0^{sc}}} \tag{2.32}$$

For triangular VLs, the largest spacing planes lie perpendicular to the [110] vectors, so

$$q_0^{tri} = \frac{2}{\sqrt{3}}\frac{2\pi}{a_0^{tri}} = 2\pi\sqrt{\frac{2\mu_0 H}{\sqrt{3}\Phi_0^{sc}}} \tag{2.33}$$

In MnSi, the triangular SkL leads to a six-fold symmetric Bragg pattern in reciprocal space. Similarly, the triangular VL of MgB_2 produces six-fold symmetric Bragg patterns.

Due to the finite volume and imperfect periodicity of real world magnetic vortex lattices, Bragg scattering does not only occur at the exact points in reciprocal space suggested by Equation 2.20. Rather, each reciprocal lattice point has a finite width in all three directions in reciprocal space that is proportional to the disorder[3] of the magnetic lattice in that direction. This disorder is normally expressed in terms of the correlation length ζ in each direction (ζ_R, ζ_A and ζ_L), which is inversely proportional to the width of the lattice point. Studying the structure of a magnetic lattice with

[3]Or inversely proportional to the finite length of the sample in the case of highly-ordered magnetic lattices.

SANS therefore becomes a matter of measuring the shape and size of each reciprocal lattice point in these three dimensions. Below I discuss a few of the most typical magnetic SANS measurements and what we can gain from performing them.

2.3.1 Individual SANS Images

Since the Ewald sphere is much larger than the reciprocal lattice spacing in the small angle limit ($|k| \gg |q|$), the flat 2D SANS detector maps well onto the surface of the Ewald sphere without significant distortion. Therefore, the SANS detector can be understood as a plane that "slices" through reciprocal space, detecting neutrons whenever that plane intersects a reciprocal lattice point (Fig. 2.11).

To understand this, it is useful to map reciprocal space with spherical coordinates (q, θ, ϕ), where q is the length of the scattering vector, θ is the angle of incidence relative to the applied field, and ϕ is the azimuth, which by convention is measured clockwise from the vertical. In this way, a single SANS image captures the scattered neutron intensity as a function of q and ϕ, for a fixed value of θ (Fig. 2.11).

Since a SANS image is only one 2D "slice" of reciprocal space, it does not contain all information about the structure of the lattice. However, individual images can be collected very quickly[4] and therefore can be incredibly useful when what you are interested in measuring falls within that plane. For example, in Chapter 3, the scattered intensity within individual Bragg peaks is used as a measure of the number of skyrmions within a crystal of MnSi as a function of field, since the intensity of Bragg scattering is proportional to the number of scattering sites. In Chapter 4, individual SANS measurements are used to confirm the azimuthal alignment of the VL with respect to the crystal lattice as a function of field.

[4]Anywhere from a few minutes to a few seconds per image for the samples discussed in this dissertation.

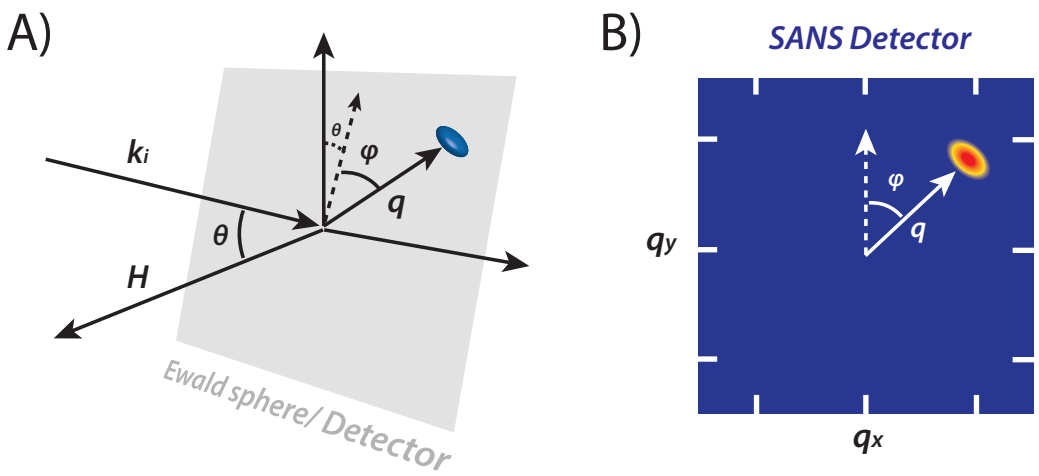

Figure 2.11. A) The Ewald sphere intersecting one reciprocal lattice point at an incident neutron angle θ. B) The resulting scattered neutron intensity in the detector plane.

2.3.2 Rocking Curves

Sometimes it is necessary to measure the full, three dimensional size and shape of a reciprocal lattice point to understand the structure of a magnetic lattice. Due to the resolution limits discussed in Section 2.2.7, the size of the corresponding measurable Bragg peaks are a convolution of both the widths of the reciprocal lattice points and the resolution limits of SANS. Often[5], the resolution limit in the azimuthal and radial directions are much greater than the width of the reciprocal lattice points in these directions. Therefore, only limited information can be gained about the shape of the lattice points in these directions. However, as discussed previously, the resolution of SANS in the longitudinal direction (Δq_L) is much better, and so precise measurement of the longitudinal order is very feasible.

To measure the longitudinal shape of a Bragg peak, the sample must be rotated within the scattering plane of the Bragg peak (i.e. the plane formed by k_i and k_f) to explore a range of scattering angles θ. This causes the Ewald sphere to move

[5]In all experiments discussed in this dissertation.

along the k_f direction through the lattice point. By recording the scattered intensity of the Bragg peak as a function of θ, one can generate a so called "rocking curve" of the Bragg peak[6]. This process is shown in Figure 2.12, where each set of colors corresponds to a separate SANS measurement which are then combined to form the rocking curve.

The shape of the rocking curve is dictated by which contribution to peak broadening (experimental resolution or sample disorder) is more significant in a given experiment. If experimental resolution dominates, the rocking curve will be predominately Gaussian in shape due to normally distributed uncertainties on the experimental parameters. If longitudinal disorder is greater, the rocking curve will be predominately Lorentzian in shape due to the finite correlation length of the vortices in the field direction. In intermediate cases where both broadening effects are significant, the rocking curve is a convolution of Gaussian and Lorentzian profiles, called a Voigt function.

Rocking curves provide much more in depth information about the structure of a VL or SkL than an individual diffraction pattern. By summing the SANS images taken at each point in a rocking curve, multiple Bragg peaks can be observed at once, allowing for a full determination of the VL/SkL symmetry. In Chapter 4, this process is used to show the distortion of the VL unit cell in MgB_2 from an equilateral triangular lattice to a scalene triangular lattice. Additionally, measurement of the rocking curve width can provide priceless information about how a magnetic structure is changing. In Chapter 3, measurement of the longitudinal correlation length in MnSi is used to better understand the microscopic dynamics of the SkL-conical phase transition. One final use of rocking curves worth mentioning is that by integrating

[6]If the sample is not rotated within scattering plane of a given peak, the Ewald sphere will not rotate through the lattice point in an a purely longitudinal direction. To account for this, the rocking curve must be rescaled by the "Lorenz factor" to generate the true longitudinal rocking curve.

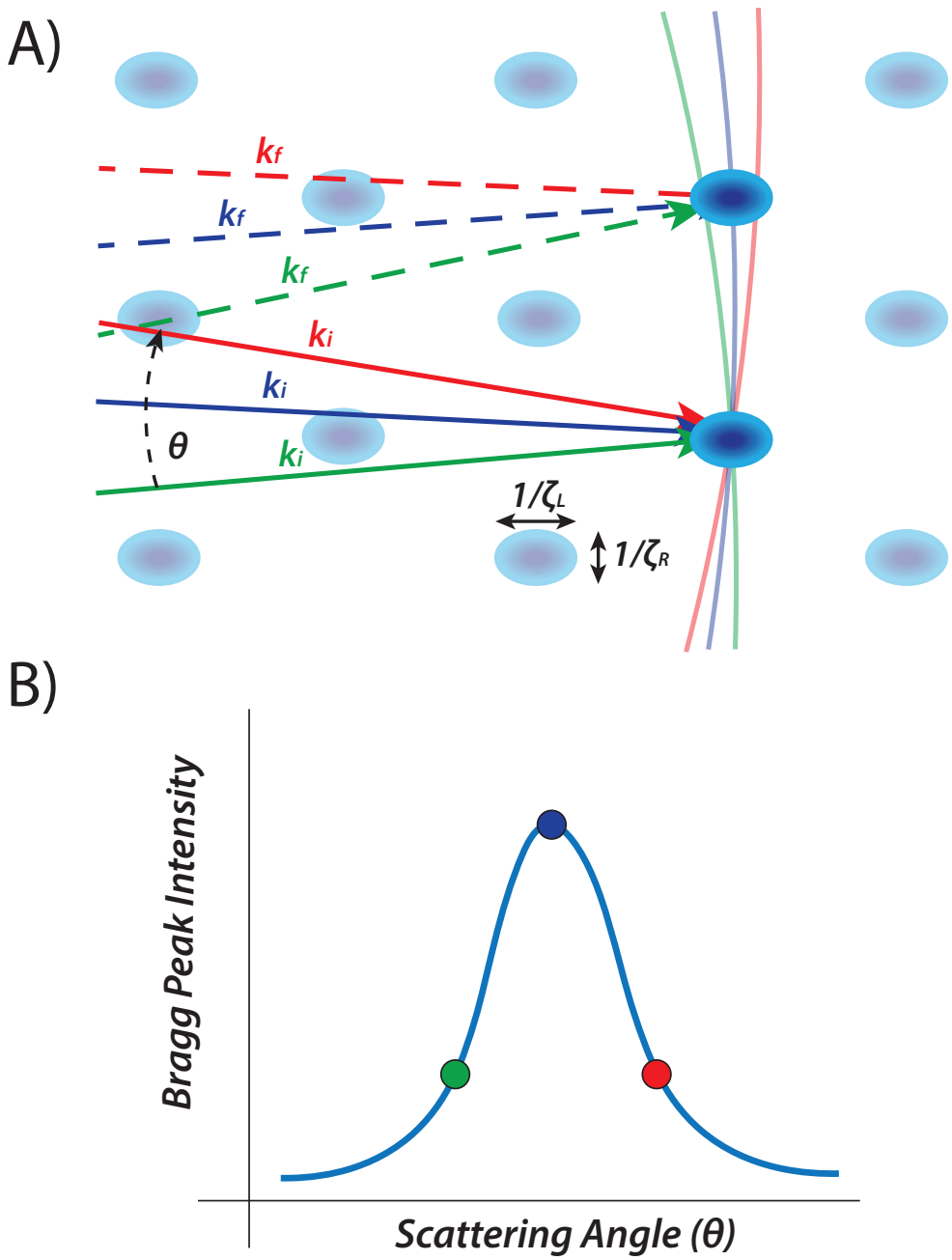

Figure 2.12. A) Ewald sphere rotating by angle θ through reciprocal space and taking different slices through the Bragg peak. Each color represents a separate SANS image, and by summing the scattered intensity in each image, a rocking curve can be plotted as a function of θ (B).

over the scattered intensity at all points within a rocking curve and dividing by the incident neutron flux, the absolute reflectivity of the VL/ SkL can be determined. This allows for a direct measurement of the magnitude of the VL/ SkL form factor $|F(\vec{q}, V(\vec{r}))|^2$.

2.4 Concluding Remarks

This chapter has discussed the application of SANS to study mesoscale magnetic vortices. By mapping the location and shape of magnetic Bragg peaks in reciprocal space, we can gain many insights into the structure and order of these vortex lattices. However, as I highlighted in **bold** in Chapters 1.1 and 1.2, many of the most interesting unanswered questions about superconducting vortex lattices and magnetic skyrmion lattices are not structural in nature but energetic. These questions cannot be directly answered from the reciprocal space information that SANS provides. However, as I discuss in the following chapters, by combining SANS with some simple (but nonetheless informative) modelling we can start to address these more fundamental questions.

In Chapter 3, we have used SANS to observe a hysteresis associated with entering and exiting the SkL phase in MnSi. By fitting this behavior to a Preisach model, we have directly measured the topological energy barrier of skyrmion formation. This demonstrates and quantifies the robust stability of magnetic skyrmions which is integral to the use of skyrmions in memory devices.

In Chapter 4, we have used SANS to explore how anisotropy impacts the VL of MgB_2. We observe that as the field is rotated away from the high symmetry c axis, a twelve-fold anisotropic term in the VL free energy is suppressed and the L phase progressively disappears. This opens the possibility for using the VL of MgB_2 as a model system to study granular systems which experience first-order (discontinuous) structural phase transitions.

Finally, in Chapter 5, we have begun the construction of a new type of skyrmion device that will allow us to more directly observe skyrmion motion due to electric current with SANS. This device will allow us to directly measure the SkL-crystal lattice interaction potential, and observe any elastic deformations of the SkL due to these forces.

CHAPTER 3

ACTIVATION BARRIER OF SKYRMION FORMATION IN MnSi

This Chapter is adapted from Leishman *et al.* [79]. Additions and modifications have been made for clarity and to add further detail.

3.1 Introduction

As discussed in Chapter 1.2, magnetic skyrmions were first observed in the chiral magnet MnSi. Despite the resulting flourish of research into MnSi, no experiments were able to directly measure the magnitude of the most promising property of the SkL: the topological energy barrier. This barrier inhibits the transition to and from the SkL to any non-topological magnetic phase (e.g. the conical, helical, or field-polarized ferromagnetic phases). As a result, both the conical and the SkL phases are bistable as local minima in the free energy over a finite region of parameter space, giving rise to phenomena such as quench metastability and field history dependence [66, 94, 13, 106, 104, 67]. Unique skyrmionic spin structures have even been predicted to be bistable with each other in certain thin film systems [23]. The metastability gives rise to activated behavior reported for $Fe_{1-x}Co_xSi$ [130] and Zn-doped Cu_2OSeO_3 [19], and the activation barrier for the destruction of a metastable SkL in the latter compound was previously determined from time-dependent measurements [132]. Similarly, the activation barrier for single skyrmions in magnetic thin films have been predicted from theoretical calculations [118, 84, 127, 51]. It is the inherent stability provided by the topological energy barrier that makes skyrmions promising candidates for memory applications, and understanding the nature of this

barrier is the key to the development of new skyrmion-based devices. In spite of this need, a complete description of the nucleation mechanism of the SkL in chiral magnets has not yet been fully established.

Here we report direct evidence of the skyrmions' topological energy barrier through a measurement of hysteresis in the SkL-conical phase transition in MnSi, using small-angle neutron scattering (SANS) [100]. Importantly, these measurements were performed on the equilibrium SkL phase rather than metastable configurations as discussed above. The existence of hysteresis is direct evidence of the bistability of the SkL and conical phases. We further employ a minimum-energy path analysis, based on an atomistic spin model, to both understand and quantify the nature of this barrier and the microscopic dynamics of the phase transition itself. The combined data shows unambiguously that it is energetically favorable for the SkL phase to form progressively, in domains consisting of hundreds of skyrmions.

3.2 Experimental Details

Initial, exploratory SANS measurements were performed on the the CG2 General Purpose SANS instrument [53] at the High Flux Isotope Reactor at Oak Ridge National Laboratory, and the D33 instrument at Institut Laue-Langevin [38]. Systematic SANS measurements of the SkL hysteresis were carried out at the SANS-I instrument at the Paul Scherrer Institute (PSI) (neutron wavelength and bandwidth: $\lambda = 0.6$ nm, $\Delta\lambda/\lambda = 10\%$) and the Bilby instrument [125] at the Australian Nuclear Science and Technology Organization (ANSTO) ($\lambda = 0.5$ nm, $\Delta\lambda/\lambda = 10\%$).

The $3.2 \times 2.0 \times 1.3$ mm^3 MnSi single crystal used for the SANS measurements was cut from a larger crystal grown by the Bridgman-Stockbarger method followed by a one week annealing at 900 °C in vacuum. The parent crystal has previously been well characterized confirming its high quality. Specifically, different pieces of the same crystal were investigated by AC magnetic susceptibility and electrical resistivity

measurements [43, 90]. This confirmed that the phase diagram agrees well with those reported in literature [102] ($T_c = 29$ K), and yielded a residual resistivity ratio (RRR) of 87 (defined as the ratio of the electrical resistivity at 300 K and 2 K). This is comparable to samples used in previous neutron scattering studies on the SkL in MnSi performed by other groups [104]. Further pieces were also characterized by resonant ultra sound measurements and energy dispersive X-ray spectroscopy, with the latter confirming the correct stoichiometry [90, 91]. Finally, an earlier SANS study of influence of uniaxial strain on the SkL has been carried out on parts of the same crystal [43]. For the SANS experiments, the MnSi crystal was aligned with the [110] direction parallel to both the applied field and the incident neutron beam, such that only one SkL orientation was energetically favorable, with SkL vector parallel to the crystallographic $[1\bar{1}0]$ direction.

At the beginning of each SANS experiment, temperature sweeps (26–32 K) and field sweeps (130–240 mT) were performed to locate the A phase boundaries. The main SANS results consist of hysteresis loops, obtained by sweeping the field between the SkL and conical phases at constant temperatures. For these loops, temperatures were selected which correspond to the maximal observed scattered intensity of the SkL (28.1 K), and to a 50% reduction of this intensity on the warmer (28.4 K) and cooler (27.8 K) sides of the A Phase. For the "major hysteresis loops", the field was swept between 130 and 240 mT using the superconducting cryomagnet. This traverses the entire A phase, with both field endpoints well within the conical phase. For the "minor hysteresis loops", the Mk 3 resistive coil was used to supplement to the superconducting magnet, and achieve a higher precision of the magnetic field. This coil, as well as the earlier versions that were used for experiments at ILL and ORNL, is described in further detail in Appendix A. A Cernox sensor and a nichrome heater were mounted in direct contact with the sample disk, allowing an independent temperature control of the sample to within ± 10 mK throughout the minor loops.

Prior to the minor hysteresis loops the sample was heated to a temperature above the A phase, and then field-cooled to the center of the upper phase transition in a constant field of 205 mT.

3.3 Experimental Results

A typical SkL diffraction pattern is given in Fig. 3.1. This shows the sum of the scattered intensity as the SkL is rotated about the vertical axis to satisfy the Bragg condition for each of the six peaks. Bragg peaks associated with the conical phase are not visible in this geometry, and therefore do not contribute to the scattering.

Figure 3.2 shows the angular dependence of the intensity of a single peak, as both the sample and applied field are rotated together through the Bragg condition. The rotation is performed perpendicular to the Ewald sphere, eliminating the need for a Lorentz correction of the angular peak width. This so-called rocking curve is well fitted by a Lorentzian line shape, indicating that it is dominated by spatial or temporal fluctuations of the SkL rather than experimental resolution [100]. We believe it unlikely that these fluctuations are temporal like those associated with critical fluctuations observed above T_c [47, 59, 68], but rather are a result of a finite skyrmion correlation length along the field direction due to crystal mosaicity as reported in other studies of MnSi [102].

Full width half maximum (FWHM) rocking curve widths $\Delta\omega$ throughout the conical to SkL transition are shown in Fig. 3.3. Here the horizontal axis is the integrated intensity, where the maximal value corresponds to being fully in the SkL phase and zero corresponds to being fully in the conical phase. The lowest intensity where complete rocking curve measurements are feasible is roughly one tenth of the maximal intensity. From the widths one can estimate the longitudinal correlation length $\zeta_L = 2(q_{\mathrm{SkL}}\,\Delta\omega)^{-1}$, where $q_{\mathrm{SkL}} = (0.388 \pm 0.002)$ nm^{-1} is the magnitude of the SkL scattering vector. As the rocking curve widths greatly exceed $\sigma_R/q_{\mathrm{SkL}} =$

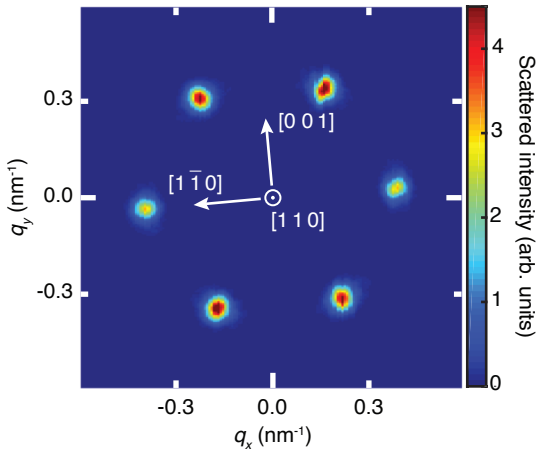

Figure 3.1. (a) Diffraction pattern of the SkL of MnSi at $H = 195$ mT. This is a sum of measurements at different rocking angles, with peaks on the horizontal axis appearing fainter as they were, on average, further from the Bragg condition. Background scattering near the detector center ($q = 0$) is masked off.

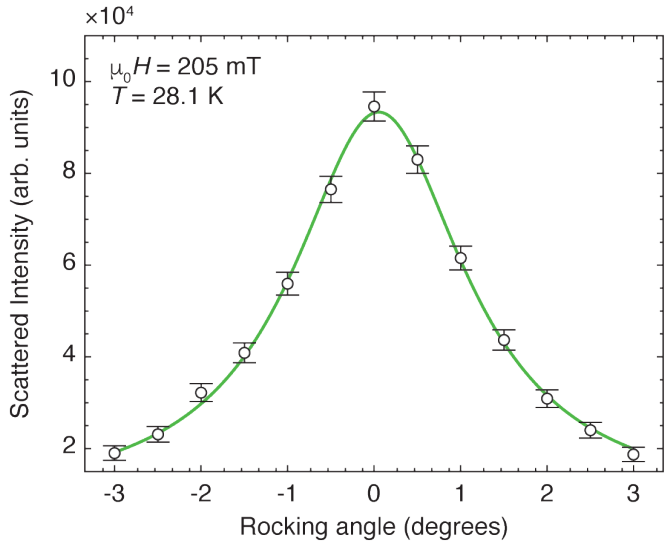

Figure 3.2. Rocking curve at $H = 205$ mT, midway along the upper SkL-conical phase transition. The curve is fit to a Lorentzian distribution with a width $\Delta\omega = 2.44° \pm 0.04°$ FWHM.

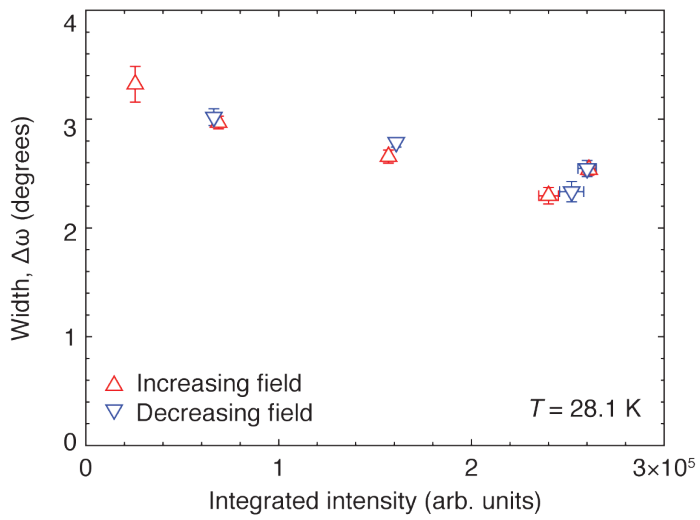

Figure 3.3. Rocking curve widths, obtained from Lorentzian fits to the data, along the upper SkL-conical phase transition for both increasing and decreasing field sweeps.

0.3° FWHM obtained from Eq. (2.31), corrections to $\Delta\omega$ due to the experimental resolution are negligible. The measured widths yield values of ζ_L ranging from 130 nm to 90 nm, indicating a reduction of the average SkL domain length along the field direction by the introduction of conical phase regions within the sample. Similarly, the lateral correlation length ζ_R can be estimated from FWHM of the Bragg peak in the radial direction within the detector plane, Δq_R. Fits of the radial intensity yields $\Delta q_R \sim 6.3 \times 10^{-2}$ nm^{-1} fully within the SkL phase, increasing to $\sim 6.9 \times 10^{-2}$ nm^{-1} upon entering the conical phase [apart from a re-scaling of the vertical axis, the behavior is near identical to that of the rocking curve widths in Fig. 4.4(c)]. Correcting for the comparatively poorer resolution within the detector plane yields $\zeta_R = 2(\Delta q_R^2 - \sigma_R^2)^{-1/2}$, with $\sigma_R = 4.8 \times 10^{-2}$ nm^{-1} obtained from Eq. (2.29). From this, one finds a lateral correlation length decreasing from 50 to 40 nm upon leaving the SkL phase. Together, these results suggest that the phase transition proceeds locally, with nanoscale regions transitioning independently over a range of applied

fields.

The total integrated Bragg peak intensity is proportional to the number of scatterers (skyrmions) in the system [102], and therefore the fraction of the sample volume within the SkL phase. Within the detector plane integration is performed by summing counts in the pixels spanning a Bragg peak (see Fig.3.4). Integration along the third dimension of reciprocal space is obtained from rocking curves. However, as the applied field H is increased into the conical phase and the scattered intensity from the SkL vanishes, the rocking curve widths only change modestly as seen in Fig. 3.3. The SkL volume fraction is thus taken to be proportional to the rocking curve peak intensity for studies of hysteresis associated with the SkL-conical phase transition. While it is possible to make corrections for the systematic variation in the rocking curve width in Fig. 3.3, this is a comparatively small effect and does not influence the analysis of the data in a significant manner as we shall discuss later.

Figures 3.5 and 3.6 shows respectively a major and a minor hysteresis loop at $T = 28.1$ K. In both cases, the intensity was normalized by the maximal observed intensity, which corresponds to the entire sample being in the SkL phase. In the major hysteresis loop, the field was swept from 130 mT to 240 mT and back. Both end points are well inside the conical phase, and this loop covers the entire A phase. Here, a clear separation of the two sweep directions is observed, with the SkL volume fraction lagging in the direction the field is changing. Importantly, thermal relaxation times in MnSi are much shorter than the SANS count times at the measurement temperatures [106], and do not contribute to the hysteresis.

To confirm hysteretic behavior, a series of minor loops were measured, each of which was centered on the high field phase transition into the conical state. Prior to each minor loop, the sample was cooled from the paramagnetic state to the measurement temperature in a constant field (205 mT), followed by a reduction of the field to the starting point. From here, minor hysteresis loops were recorded by raising the

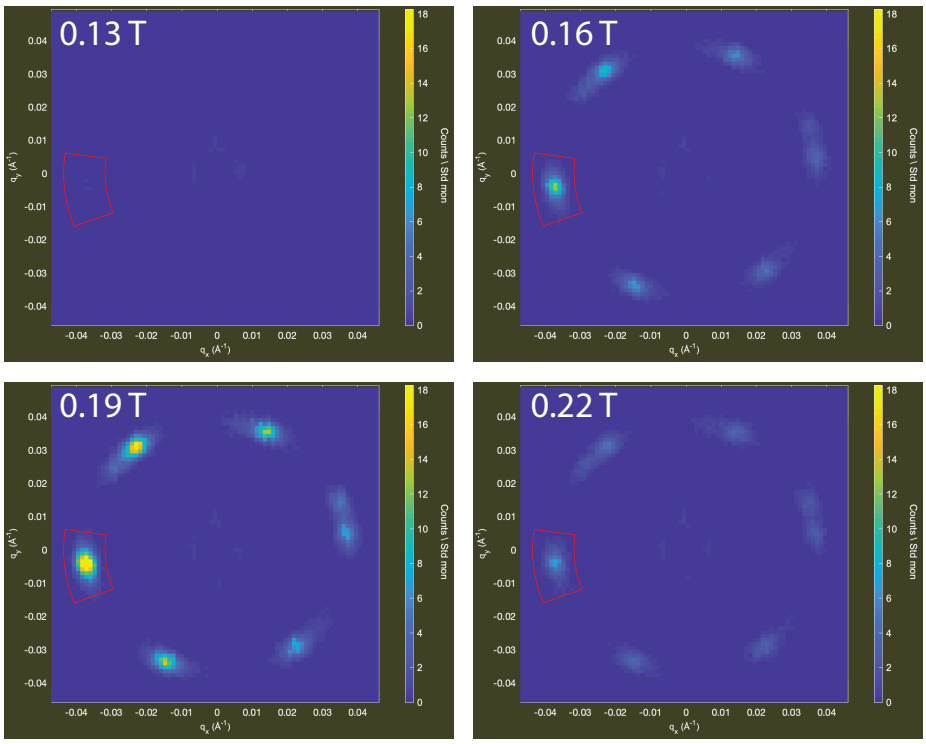

Figure 3.4. Raw diffraction pattern from the SkL as magnetic field is increased through the A Phase. All measurements shown correspond to the 28.1 K measurement at ANSTO. Also shown in red is the polar coordinate box within which all pixels are summed to calculate the scattered intensity for each data point in the hysteresis loops.

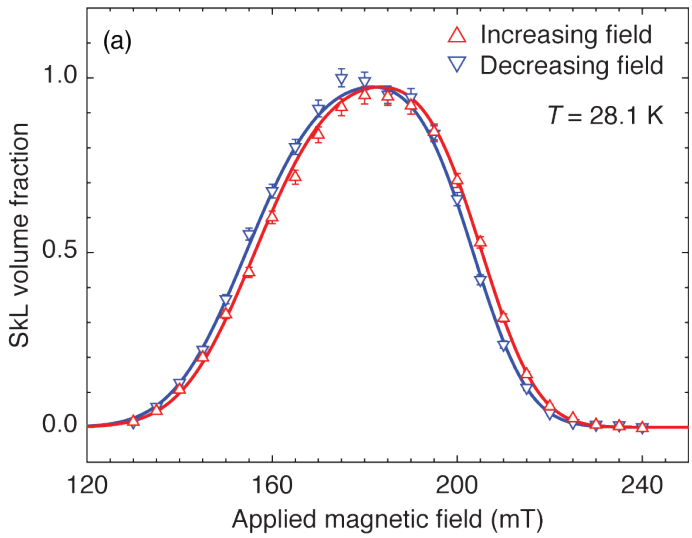

Figure 3.5. Major hysteresis loop for $T = 28.1\ K$ recorded at PSI. Curves shown are fits to an adapted Preisach model described in the text.

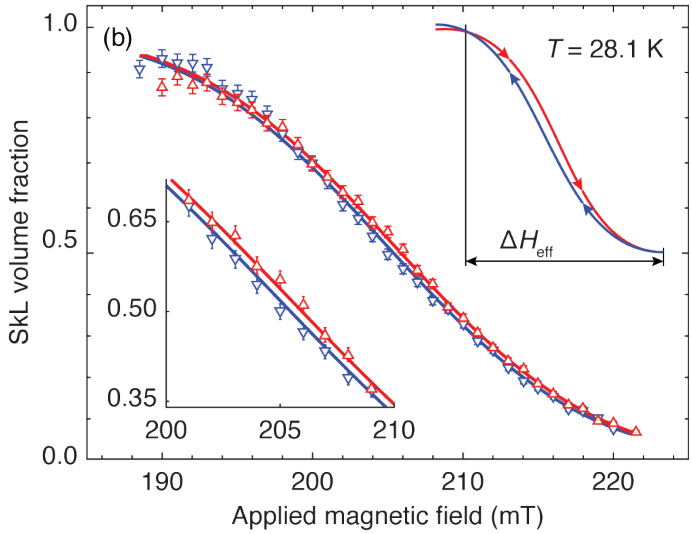

Figure 3.6. Minor hysteresis loop at the same temperature, centered around 205 mT and with an field sweep range of 33 mT. Symbols are the same as in Figure 3.5. Bottom left inset: Expanded view of the central part of the loop. Top right inset: Schematic showing field sweep direction and effective sweep range ΔH_{eff}. Curves shown are fits to an adapted Preisach model described in the text.

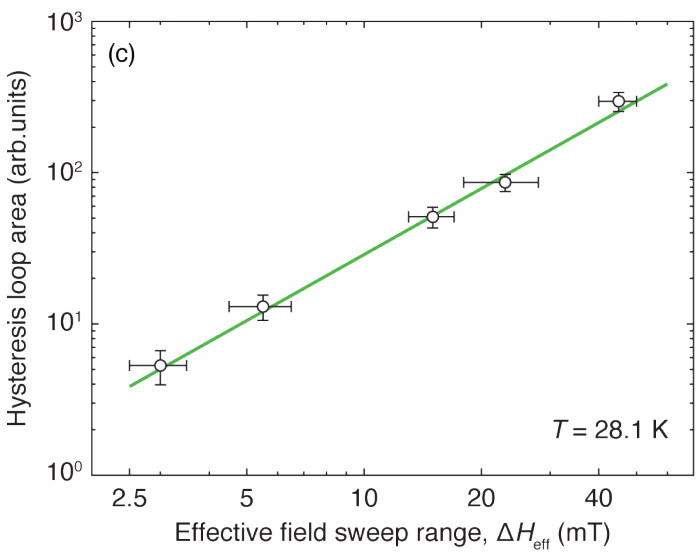

Figure 3.7. Area of the minor and major hysteresis loops as a function of the effective sweep range.

field to partially leave the SkL phase and then decreasing it to reenter. An example of a minor loop is show in Fig. 3.6. Minor loops of four different lengths were performed, and the area of each of these loops is plotted in Fig. 3.7. The areas are plotted as a function of the effective length of the loop ΔH_{eff}, defined as the separation between the two crossing points of the different field sweep directions illustrated in the Fig. 3.6 inset, which were determined from fits to the data. As seen in Fig. 3.7, the area of these loops grows superlinearly, following a power law $\propto \Delta H_{\text{eff}}^{1.45\pm0.1}$. This shows that as the loops grow longer, they must also become wider, and therefore nest inside each other as expected for a true hysteresis.

To quantify the activation barrier for skyrmion formation and destruction, the SANS hysteresis loops are analyzed using an adapted Preisach model. This is suitable for transitions in bistable systems, where two phases coexist as local free energy minima over some range of the external field [17]. In the region of bistability, the free

TABLE 3.1

MAJOR HYSTERESIS LOOP FITS

Facility	T (K)	$\overline{H}_{c1}$ (mT)	σ_{c1} (mT)	$\overline{H}_{a1}$ (mT)
ANSTO	27.8	188 ± 8	19 ± 2	1.1 ± 0.3
PSI	28.1	155.3 ± 0.2	12.5 ± 0.2	0.94 ± 0.14
ANSTO	28.1	160.2 ± 0.5	13.7 ± 0.3	1.1 ± 0.2
ANSTO	28.4	168 ± 9	21 ± 3	1.0 ± 0.3
		$\overline{H}_{c2}$ (mT)	σ_{c2} (mT)	$\overline{H}_{a2}$ (mT)
ANSTO	27.8	211 ± 3	14 ± 1	1.0 ± 0.2
PSI	28.1	204.4 ± 0.2	9.5 ± 0.2	0.96 ± 0.12
ANSTO	28.1	212.5 ± 0.4	12.0 ± 0.3	0.8 ± 0.2
ANSTO	28.4	200 ± 6	19 ± 2	0.7 ± 0.3

Preisach parameters obtained from fits to major hysteresis loops. Uncertainties indicate the one sigma confidence interval provided by the fitting algorithm.

energy F is assumed to be linearly proportional to the magnetic field B:

$$F(B, T, \ldots) = F(B_c, T, \ldots) \mp (X - X_0/2)(B - B_c). \tag{3.1}$$

Here, X is an order parameter with dimensions of a magnetic moment, used to distinguish the conical ($X = 0$) and skyrmion ($X = X_0$) phases. The sign of the second term in Eq. (4.5) corresponds to respectively the lower (-) and upper (+) transition between the SkL and conical phases. The Preisach free energy as a function of applied field is shown in Fig. 3.8(a). A similar picture was previously proposed to describe temperature-quenched metastable SkL phases in MnSi [106].

The low- and high-field transitions are treated independently, with each one gov-

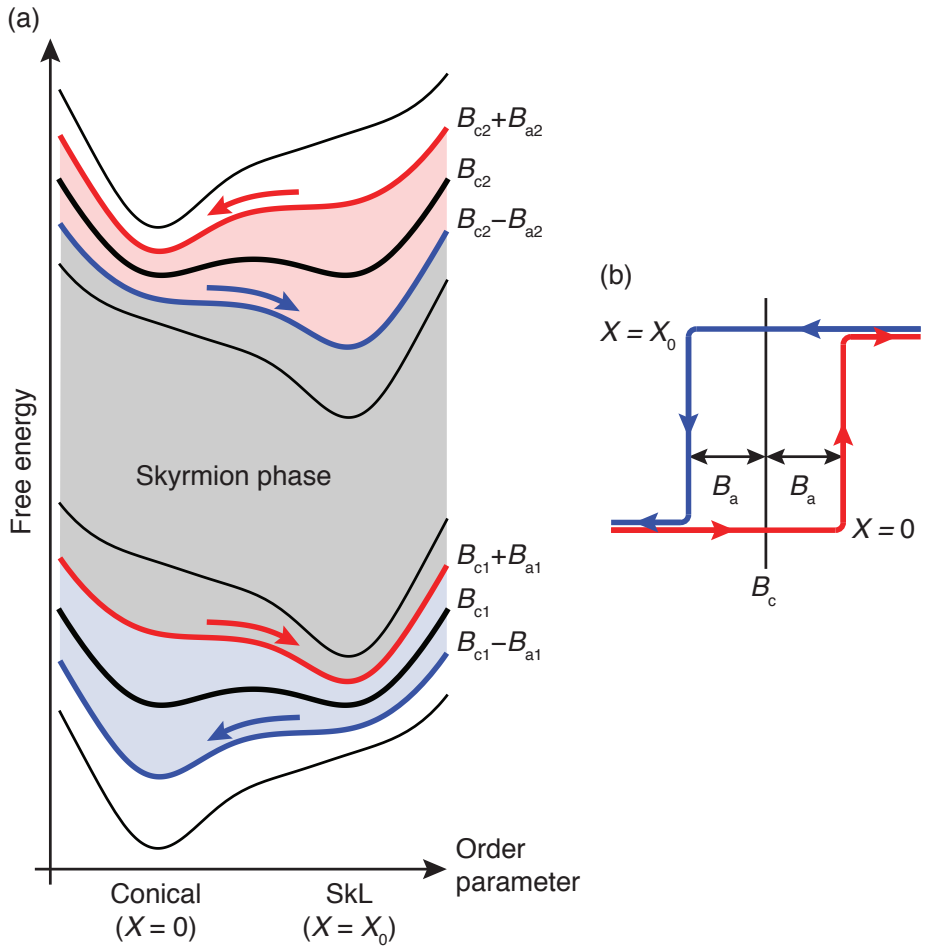

Figure 3.8. Behavior of an individual Preisach unit. (a) Free energy for different values of the applied field. Black curves correspond to fields where the conical and SkL phases have the same energy. Red (blue) curves indicate the location of the phase transition for increasing (decreasing) field. (b) Hysteretic response of the order parameter.

erned by a pair of parameters: the critical field ($B_{c1/c2}$) where the two phases have the same free energy, and the height of the activation barrier ($B_{a1/a2}$) that inhibits the transition. As the external magnetic field is increased from zero and approaches the lower conical-to-SkL phase transition, the conical state free energy increases and the SkL state free energy decreases. At $B = B_{c1} + B_{a1}$, the conical phase minimum vanishes and the system transitions to the skyrmion phase. For decreasing fields, the transition occurs at $B = B_{c1} - B_{a1}$. Similarly, the upper SkL-to-conical transition occurs at $B = B_{c2} \pm B_{a2}$, where the situation is reversed and the conical and SkL free energies respectively decrease and increase with increasing field. The Preisach model is an inherently zero-temperature model, and a transition between the states only occurs when one minima disappears and the system is no longer bistable. This is appropriate for the SkL as reported activation barriers are much greater than $k_B T$ [132] for $T \leq T_N$.

Preisach free energy curves produce perfectly rectangular hysteresis loops, centered around B_c and with width $2B_a$, as shown in Fig. 3.8(b). Rounded loops are obtained by considering the sample to be composed of microscopic, independently-acting, "Preisach units", each with its own $B_{c1/c2}$ and $B_{a1/a2}$. Since the magnetization is approximately linear across both the upper and lower field phase transitions [16], we express $B_{c1/c2}$ and $B_{a1/a2}$ in terms of the corresponding applied fields $H_{c1/c2}$ and $H_{a1/a2}$. To model the SANS hysteresis loops, Preisach units are assumed to follow a Gaussian distribution in both critical and activation fields. These distributions are characterized by their mean values ($\overline{H}_{c1/c2}, \overline{H}_{a1/a2}$) and standard deviations ($\sigma_{c1/c2}, \sigma_{a1/a2}$). The hysteretic behaviour of a system can be predicted given the set of ($\overline{H}_{c1/c2}, \overline{H}_{a1/a2}, \sigma_{c1/c2}, \sigma_{a1/a2}$), and therefore we can use least squared fitting to uniquely determine these parameters. Performing these predictions and fitting such a large parameter space is quite an interesting computational problem and it is discussed in detail in Appendix B.

A fit to the PSI major hysteresis loop for $T = 28.1$ K is shown in Fig. 3.5, and the resulting parameter values are summarized in Table 3.1. Values of $\sigma_{a1/a2}$ converge to zero during the fit, and this parameter was therefore eliminated. This suggests that the activation barrier has a constant value throughout the entirety of the illuminated sample. Differences between the fit and the data near the maximum SkL volume fraction are due to the assumed Gaussian Preisach distribution fitted to the data. A skewed distribution, introducing additional degrees of freedom, could improve the overall fit. However, the values of $\overline{H}_a$, which is the principal variable of interest, would most likely remain unchanged as they depend on the width of the hysteresis (separation of up- and down-sweeps) at half SkL volume fraction, where the current fits are very good. Finally, rescaling the data to account for the changing rocking curve width previously discussed only effects the Preisach fits minimally. Specifically, $\overline{H}_{c1}/\overline{H}_{c2}$ are shifted by $\sim 2\%$ in opposite directions to increase the width of the SkL phase, σ_{c1}/σ_{c2} are both reduced by $\sim 5\%$, and $\overline{H}_{a1}/\overline{H}_{a2}$ remain within uncertainty of the values in Table 3.1.

Also included in Table 3.1 are results of fits to the major loops recorded at ANSTO at three different temperatures. The difference in the fitted values of $\overline{H}_{c1/c2}$ at 28.1 K may be attributed to variations in the remnant field of the cryomagnets used, supported by the similar separation between the upper and lower transitions for the PSI and ANSTO results. The larger uncertainty on $\overline{H}_{c1}/\overline{H}_{c2}$ and greater values of σ_{c1}/σ_{c2} at 27.8 K and 28.4 K are due to the weaker scattering and therefore lower statistics at these temperatures. Importantly, the least affected parameters are the two activation fields, which remains consistent and with modest uncertainties across all the measurements.

As the upper and lower phase transitions are treated entirely independently in this model, some Preisach units could, in principle, return to the conical phase before others have entered the SkL phase. At 28.1 K, where the separation of the tran-

sition fields is much greater than $\sigma_{c1/c2}$, this rarely occurs. However, at 27.8 K and 28.4 K the transitions overlap significantly, preventing the intensity from reaching the maximum at 28.1 K, which is reflected in the increased values of σ_{c1}/σ_{c2}. More importantly, the good agreement between $\overline{H}_{a1}$ and $\overline{H}_{a2}$ supports a topological origin for the activation barrier which should be similar for both phase transitions. Further support for this conclusion comes from the consistent values of the activation fields at different temperatures. This indicates that the finite temperature range of the A Phase is not due to a significant reduction of the activation barrier, but rather a convergence of the two critical fields as the energy separation between the conical and SkL phases is reduced.

While applying the Preisach model does not require prior knowledge about the nature of individual units, it is nonetheless relevant to consider their nature. In the original application to ferromagnetic hysteresis, magnetic domains behave sufficiently independent to be treated as Preisach units. By analogy, we anticipate that in the present case they correspond to microscopic SkL domains, within which the cascade of individual skyrmion formation occurs much faster than the measurement time. In this way, each domain experiences the phase transition quasi-instantaneously and independent of other domains. This is consistent with the longitudinal and lateral correlation lengths discussed previously, providing a characteristic length scale for the SkL domains of the order 100 and 50 nm, respectively. In such a scenario, variations of the local magnetic field due to crystal inhomogeneities and demagnetization effects give rise to a range of different transition fields and therefore a non-zero σ_c. This explanation is supported by the observations of Reimann *et al.* [117], where demagnetization causes the SkL to form progressively as field increases, first along the outside edges of the crystal before saturating to the center. An estimate of the demagnetizing effects in our samples is discussed in Appendix C. It is likely that both the distribution of SkL domains throughout the sample as well as their sizes

TABLE 3.2

MINOR HYSTERESIS LOOP FITS

ΔH_{eff} (mT)	$\overline{H}_{c2}$ (mT)	σ_{c2} (mT)	$\overline{H}_{a2}$ (mT)
5.5 ± 1.0	203.6 ± 0.2	11.5 ± 0.2	0.18 ± 0.05
15 ± 2	204.8 ± 0.1	10.5 ± 0.1	0.16 ± 0.05
23 ± 5	205.1 ± 0.2	10.5 ± 0.1	0.25 ± 0.04

Preisach parameters obtained from minor hysteresis loops at $T = 28.1$ K (PSI).

depend on the field and temperature history, which may affect the activation barriers observed in the SANS experiments. To explore this possibility Preisach model fits were performed on the minor hysteresis loops, where the initial configuration was obtained by a field cooling to the midpoint of the upper SkL-conical transition. In contrast, the major loop has a starting point entirely within the conical phase. The results of the minor loop fits are summarized in Table 3.2. While the values of $\overline{H}_{c2}$ agree with those obtained from the major loop, $\overline{H}_{a2}$ is reduced significantly, confirming that the barrier to create or destroy SkL domains depends on the field history. We return to this point later.

3.4 Theoretical Modeling

To complement the SANS data, we established a collaboration with M. V. Milošević and R. M. Menezes from the University of Antwerp to perform atomistic spin dynamics simulations of MnSi. These simulations were performed by R. M. Menezes to investigate the transition between the conical and SkL states using a homemade simulation code [127] as well as the *Spirit* package [101]. The extended Heisenberg

Hamiltonian that describes the system of classical spins can be written as

$$\mathcal{H} = -J\sum_{\langle i,j\rangle}\mathbf{n}_i\cdot\mathbf{n}_j - \sum_{\langle i,j\rangle}\mathbf{D}_{ij}\cdot(\mathbf{n}_i\times\mathbf{n}_j) - \sum_i \mu\mathbf{B}\cdot\mathbf{n}_i, \tag{3.2}$$

where μ_i is the magnetic moment of the i^{th} atomic site with $|\mu_i| = \mu$, and $\mathbf{n}_i = \mu_i/\mu$ is the i^{th} spin orientation. Here J represents the first-neighbors exchange stiffness, $\mathbf{D}_{ij}$ is the DMI vector, $\mathbf{B}$ is the perpendicular external magnetic field, and $\langle i,j\rangle$ denotes pairs of nearest-neighbor spins i and j. For the simulations, the parameters $J =$ 1 meV and $D = 0.18J$ were adopted, which are reasonable values for MnSi [58, 57]. Although intrinsic exchange and cubic anisotropies [11] may define a preferential direction for the spin rotation in MnSi at zero field, such high-order contributions are much weaker than the energy terms in Eq. 3.2 and were therefore neglected in the calculations. Similarly, the small contribution from a dipolar interaction was also not included [95, 48]. The dynamics of the spin system is governed by the Landau-Lifshitz-Gilbert equation

$$\frac{\partial\mathbf{n}_i}{\partial t} = -\frac{\gamma}{(1+\alpha^2)\mu_i}\left[\mathbf{n}_i\times\mathbf{B}_i^{\text{eff}} + \alpha\mathbf{n}_i\times(\mathbf{n}_i\times\mathbf{B}_i^{\text{eff}})\right], \tag{3.3}$$

where γ is the electron gyromagnetic ratio, α is the damping parameter and $\mathbf{B}_i^{\text{eff}} = -\partial\mathcal{H}/\partial\mathbf{n}_i$ is the effective field.

The MnSi crystal, shown in Fig. 3.9, consists of a B20 structure (space-group $P2_13$) with four Mn atoms and four Si atoms [60]. For the simulations, only Mn magnetic moments were considered. The spin dynamics simulations were performed in a mesh of $N\times\sqrt{3}N\times N$ unit cells with $N = 26$, and the SkL state consists of two skyrmion tubes located at respectively the center and corners. The choice of N was verified to minimize the SkL energy. Periodic boundary conditions were considered along the three dimensions. To obtain the ground state of the spin model, the energy of the considered states were minimized for different values of the applied

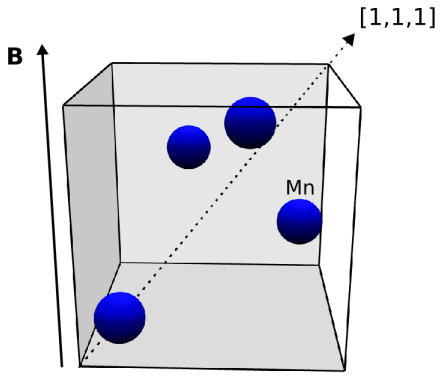

Figure 3.9. Unit cell of the B20-structure of MnSi showing only the location of the Manganese atoms. The magnetic field **B** was applied along the [001] direction.

field **B** ∥ [001]. The choice of field direction parallel to one of the unit cell main axes ensured that skyrmions form as uniform tubes within the simulation box. However, the direction of the applied field is not expected to have much impact on the energetics as long as a high-symmetry direction of the crystal is chosen. Figure 3.10(a) shows the energy obtained in the simulations for the field-polarized ferromagnetic, conical and SkL states, from where the ground state was found to be conical for $\mu B < 0.007J$ and $0.018J < \mu B < 0.028J$, SkL for $0.007J < \mu B < 0.018J$, and field-polarized ferromagnetic for $\mu B > 0.028J$.

Next, the transition between the conical and SkL states was considered. At the critical fields $\mu B_{c1} = 0.007J$ and $\mu B_{c2} = 0.018J$, both states had approximately the same energy. The activation barrier between the two states was calculated by the geodesic nudged elastic band (GNEB) method [18, 127] and a climbing image method [54], which allowed for a precise determination of the highest energy saddle point along the minimal energy path connecting the two states. Here, the reaction coordinate defines the normalized (geodesic) displacement along the formation path. Figure. 3.10(b) shows the activation barrier calculated between the two states in both critical fields. From this, our collaborators found that it is energetically favorable to

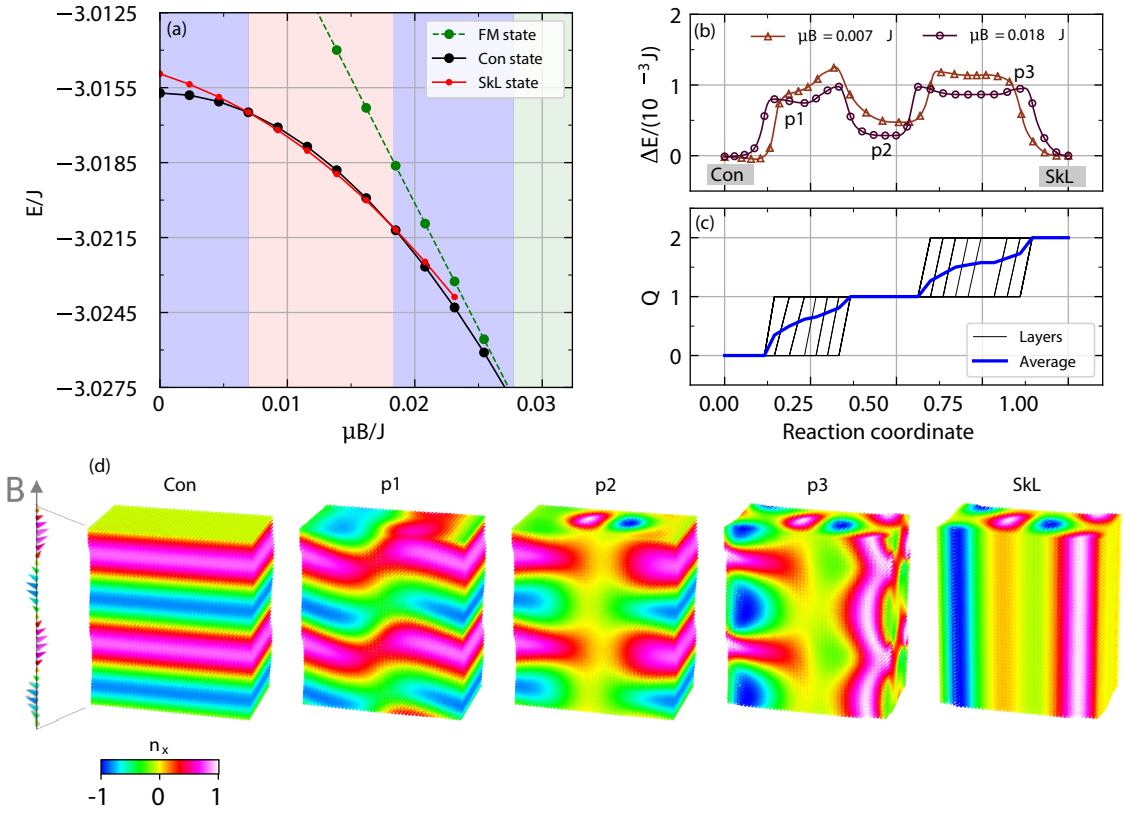

Figure 3.10. (a) Energy per spin vs applied field for each state. The ground state is indicated by the colored shading with blue for the conical (Con) state, red for the SkL and green for the field-polarized ferromagnetic (FM) state. (b) Minimal energy path between conical and SkL states for $\mu B = 0.007J$ and $\mu B = 0.018J$. (c) Topological charge as a function of the reaction coordinate for $\mu B = 0.018J$. (d) Spin configurations in a $N \times \sqrt{3}N \times 2N$ mesh along the formation path for $\mu B = 0.018J$, as indicated in panel (b) (see also animated data in Supplemental Material in Reference [3]).

break the conical state locally in different stages, nucleating the skyrmions individually instead of the whole lattice at once (see also animated data in the Supplemental Material in Reference [3]). Figure 3.10(c) shows the topological charge, given by [41]

$$Q = \frac{1}{4\pi} \int \mathbf{n} \cdot \left(\frac{\partial \mathbf{n}}{\partial x} \times \frac{\partial \mathbf{n}}{\partial y}\right) dx\, dy, \tag{3.4}$$

calculated along the formation path for each xy-layer of the sample for $B = B_{c2}$. Notice that the tube of the first skyrmion was formed gradually, layer-by-layer, in a conical background and the average topological charge approaches $Q = 1$, giving rise to the first elongated maximum in the minimal energy path. This was consistent with previous works suggesting that skyrmions are nucleated or annihilated by the formation and subsequent motion of Bloch points (magnetic monopoles) [97, 121, 119]. After that, the second skyrmion was formed in a similar way, after which the average topological charge approaches $Q = 2$ and the transition is completed. Energetically equivalent paths were obtained for the first skyrmion nucleating either at the center or the corners.

As recognized previously, the transitions between the SkL and conical states are not expected to occur in a spatially homogeneous fashion. As a result, the average energy per spin necessary to nucleate a single skyrmion depends on the lateral size of the domains. An estimation of the activation barrier can be obtained by comparing the energy separation $\Delta E_a = |E_{\mathrm{SkL}} - E_{\mathrm{Con}}|$ of the SkL and conical states near the critical field, due to an activation field B_a equivalent to the one obtained from the SANS experiments. Adjusting for the difference between the transition fields obtained experimentally and from the simulations one finds $B_a \approx (B_{c2} - B_{c1})/50 \approx 2\times10^{-4} J/\mu$, and from there $\Delta E_a \approx 10^{-5} J$. This value is roughly two orders of magnitude smaller than the activation energy calculated in the GNEB simulation where the SkL was formed in two steps. Therefore, to nucleate one skyrmion with a 100 times smaller activation field in the simulations we need to consider a phase transition that occurs in

100 times as many steps as previously. This is exactly equivalent to using a 100 times larger simulation box, as the activation energy is given by the number of skyrmion nucleations per area. Considering the SkL periodicity of 19 nm in MnSi [102], this corresponds to skyrmion domains of order $\sim 0.05\ \mu\text{m}^2$. This is the same order of magnitude as the correlation length determined directly from the SANS rocking curve widths.

As the formation barrier for the individual skyrmions along the reaction coordinate are all roughly the same height (see Fig. 3.10(b)), once the system has sufficient energy to overcome the initial barrier skyrmions will continue to nucleate in a cascade until defects or demagnetization makes it energetically unfavorable. This limits the size of the SkL domains, and we speculate that this mechanism is responsible for the discrete Preisach units observed in the SANS measurements. This likely also explains the difference in activation barrier between the major and minor loops. In the major loops, new SkL domains are being pushed into the sample from the outside edge of the crystal [117]. However, with the minor loops, since the loop starts with the SkL volume fraction at $\approx 50\%$, the crystal is already "seeded" with SkL domains, so the change of SkL volume fraction during the loop is due to the expansion/reduction of already present domains formed during the field cooling. This results in a smaller activation barrier, which persists since the crystal never reaches a fully saturated conical or SkL phase throughout the minor loop. Spatially resolved measurements would be required to confirm this picture.

The topological energy barrier for each skyrmion can be estimated by multiplying ΔE_a by the number of spins within a SkL unit cell, and increasing the length of the skyrmions in the simulations to the thickness of the single crystal used in the SANS experiments. Using the above relationship between B_a and J/μ with $\mu = 0.4\mu_B$ [85], this yields $\Delta E_a \approx 7$ eV per skyrmion. By the nature in which it was obtained, the activation energy above should be considered as an estimate rather than an exact

value. Taking into account that ΔE_a scales linearly with the sample thickness, our estimate for MnSi is roughly 3–4 times greater than the $\sim$ 1.6 eV reported for zinc-substituted Cu_2OSeO_3 [132]. This difference may be due to the higher temperature ($\sim$ 53 K vs $\sim$ 28 K) and lower fields ($\sim$ 25 mT vs $\sim$ 180 mT) at which the A phase exists in Cu_2OSeO_3. Skyrmions in GdO_x/Gd/Co/Pt heterostructures were also recently found to have a formation energy of $\sim$1.4 eV [139].

3.5 Conclusion

In summary, we presented the first direct observation of the hysteresis in the formation and destruction of the skyrmion lattice in MnSi. The measured hysteresis proves that skyrmion lattice and the conical phase are bistable over a finite range of parameters, with a finite *topological* activation barrier inhibiting the phase transition in either direction. This observation validates the topological stability of skyrmions. Comparing the experimental data to the results of atomistic spin simulations indicates that skyrmion lattice is formed progressively in smaller domains, containing hundreds of skyrmions, with an activation barrier of several eV/mm for a single skyrmion.

Our results advance the understanding of the nucleation mechanism of the SkL in chiral magnets, and we expect that our findings will instigate further measurements of topological energy barriers between different (chiral) magnetic states. Such studies are key to understanding the evolution of magnetic states in bulk and ultrathin materials and will establish definitively the feasibility of high-density devices based on topological spin structures.

CHAPTER 4

ANGLE DEPENDENT VORTEX LATTICE PHASE DIAGRAM IN MgB_2

This Chapter is adapted from Leishman *et al.* [80], which has been submitted for review at *Physical Review B*. Additions and modifications have been made for clarity and to add further detail.

4.1 Introduction

Vortex matter in type-II superconductors is highly sensitive to the environment provided by the host material. An example is the vortex lattice (VL) symmetry and orientation, which is governed by anisotropies in the screening current plane perpendicular to the applied field and the associated nonlocal vortex interactions [71, 72]. Such anisotropies may arise from the Fermi surface or, in non-s wave superconductors, from nodes in the superconducting gap. A rich VL phase diagram often arises when this anisotropy is incommensurate with an equilateral triangular VL, as seen in Nb with the applied field along the [100] crystalline direction [77, 78, 99]. However, structural transitions between different VL configurations can also arise when the field is applied perpendicular to a sixfold symmetric crystal plane. In such cases, the free energy landscape is so isotropic that higher-order contributions to the screening current plane anisotropy become relevant, affecting the orientation of the triangular VL relative to the crystalline axes as seen in UPt_3 [45, 10] and MgB_2 [29, 30].

As discussed in Chapter 1.1, three different triangular VL phases (labeled F, L and I) were observed in MgB_2 for $H \parallel c$, distinguished by their orientation relative to the crystalline axes [30]. These three phases are shown in the $H-T$ plane of Fig. 4.1.

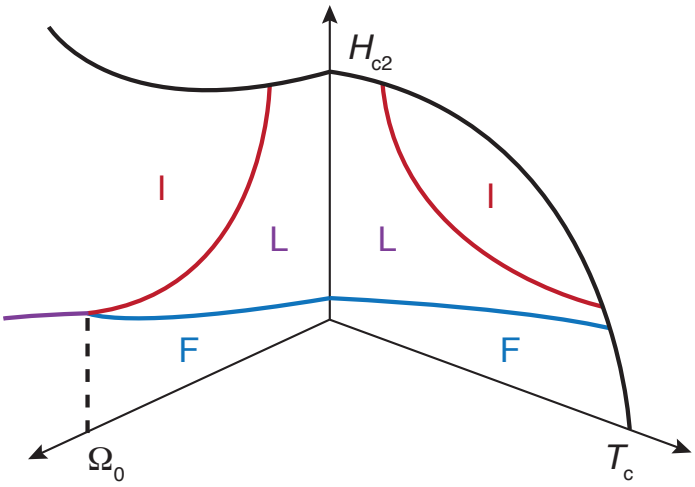

Figure 4.1. Qualitative MgB_2 VL phase diagram in the $\Omega = 0$ ($H \parallel c$) and $T = 0$ planes. The former was determined previously [30], and the latter is discussed in this work. The VL L phase vanishes at the critical angle, Ω_0.

Due to the hexagonal crystal structure of MgB_2 and the s-wave pairing, the VL free energy for $H \parallel c$ can be expanded in term with anisotropies that are multiples of six[1] [137]. Moreover, as discussed in Chapter 1.1, the continuous rotation in the L phase implies that at least the six- and twelvefold terms are sufficiently strong to influence the VL orientation, as the transition would otherwise be discontinuous. Here, we have sought to explore the evolution of the VL phase diagram as the twelvefold anisotropy is suppressed by rotating the applied field away from the c axis. We find that the twelvefold anisotropy decreases linearly as the rotation angle is increased, reducing the size of the L phase until it disappears entirely from the phase diagram at a critical value. Above the critical angle, the VL undergoes a first order phase transition directly from the F to I phase.

[1]Free energy terms that are not $6n$ rotation symmetric lead to a contradiction, as the total energy of the triangular VL would no longer be constant under 30 degree rotations

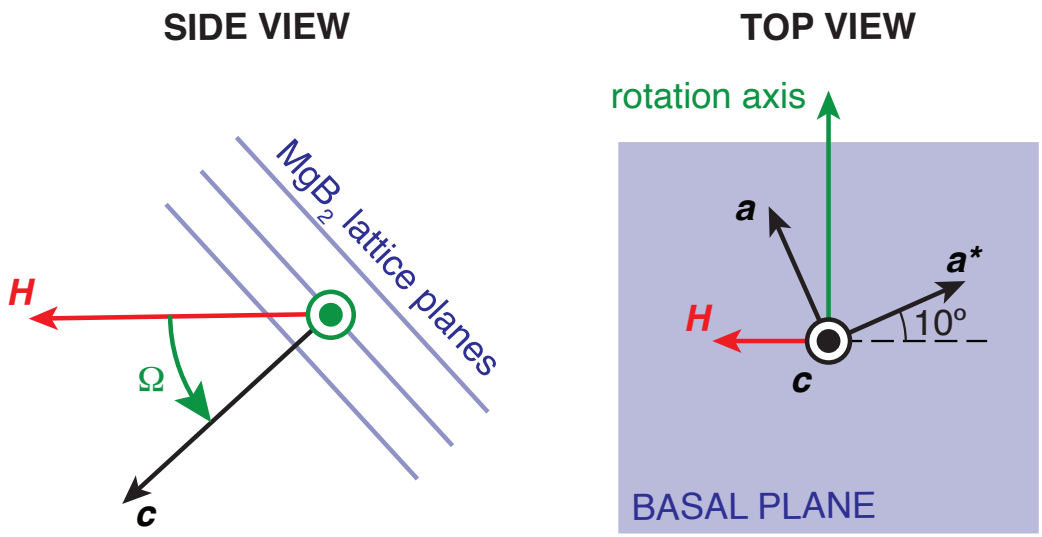

Figure 4.2. Experimental geometry, indicating the direction and rotation axis of the magnetic field relative to the crystalline axes.

4.2 Experimental Details

The VL was studied using small-angle neutron scattering (SANS) [100]. The SANS measurements were performed at the Bilby instrument [125] at the Australian Nuclear Science and Technology Organization. Preliminary SANS measurements were carried out at the NG7 beam line [46] at the National Institute of Standards and Technology Center for Neutron Research.

The experimental geometry used for the SANS measurements is shown in Fig. 4.2. Here the magnetic field is applied along the horizontal neutron beam direction, and at an angle Ω relative to the crystalline c axis achieved by rotating the sample about the vertical axis *in situ*. The SANS measurements used a neutron wavelength $\lambda_n =$ 0.6 nm and bandwidth $\Delta\lambda_n/\lambda_n = 10\%$. All measurements were performed at 2 K.

Measurements were performed on a 200 μg single crystal of MgB_2 grown using a high pressure cubic anvil technique [65]. The crystal has a platelet geometry, roughly 1 mm $\times$ 1 mm wide and 50 μm thick along the c axis, and is isotopically enriched

with ^{11}B to reduce neutron absorption. The the superconducting critical temperature of the sample is $T_c \approx 38$ K, and the upper critical field increases from $H_{c2} = 3.1$ T to $\sim$18 T as the field is rotated from the c axis ($\Omega = 0$) to the basal plane ($\Omega = 90°$).[65]

4.3 Experimental Results

Figure 4.3(a) shows a VL diffraction pattern obtained for $H \parallel c$, with all six Bragg peaks lying on a circle of radius $q = 2\pi(2\mu_0 H/\sqrt{3}\Phi_0)^{1/2}$ where $\Phi_0^{sc} = h/2e = 2069$ T nm^2 is the superconducting flux quantum. Here, the field and crystal have been rotated together through the Bragg condition of all six VL peaks. The crystal was deliberately mounted with the a axis roughly 10° from the vertical to investigate whether the degeneracy of the two VL domain orientations in the L phase can be lifted by rotating the applied field away from the c axis. Specifically, at an applied field of 0.5 T, one of the split peaks of the L phase would lie close to the vertical axis of rotation, which is preferred by London theory [24], while the other would lie off of it (see Fig. 4.4(a)). We anticipated that this difference would be enough to measurably alter the fraction of the VL that was in each configuration, perhaps eliminating the off-axis domains entirely.

The field rotation introduces a distortion of the VL due to the different penetration depth within the basal plane vs perpendicular to it [24]. This is seen in the SANS diffraction patterns in Fig. 4.3(b) as a relocation of the six Bragg peaks such that they lie on an ellipse with the minor axis parallel to the axis of rotation. We note that the diffraction patterns in Fig. 4.3 were obtained following a field cooling, which for $H \parallel c$ left the VL in a metastable F phase [30].

To test the effect of the field rotation on the VL phase diagram, measurements were made with $\Omega = 0°, 30°, 45°, 60°$, and 70° and fields between 0.3 T and 1.2 T. Prior to each measurement, the magnitude of the applied field was oscillated about the desired value to ensure that the VL was settled into an equilibrium state [81, 30].

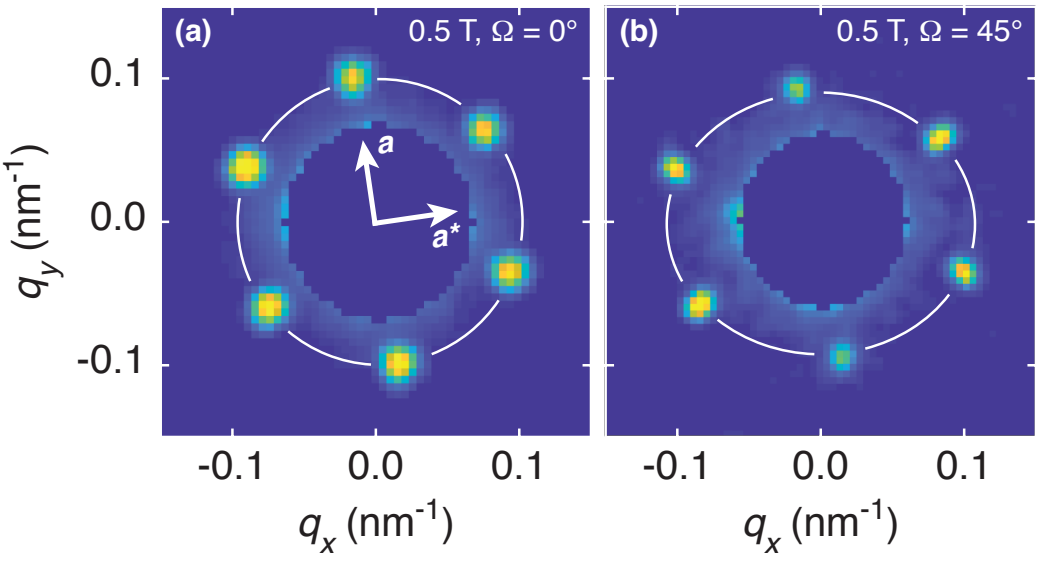

Figure 4.3. Vortex lattice diffraction patterns at $H = 0.5$ T and (a) $H \parallel c$ and (b) $\Omega = 45°$. The orientation of the crystalline axes is indicated in (a). Both measurements were performed following a field cooling from above T_c. Background scattering near the detector center is masked off.

As seen in Figs. 4.4(a)-4.4(d), the elliptical distortion increases with Ω. It is useful to quantify this distortion by the geometric anisotropy of the ellipse ε, defined as the ratio of its major and minor axes. At $\Omega = 90°$, ε is expected to reach the penetration depth anisotropy [24]. To conserve beam time, not all VL peaks were rocked through the Bragg condition for all measurements; however their location can be determined from symmetry and the analysis discussed below, and are indicated by open circles in Figs. 4.4(a)-4.4(d). Within the L phase, split Bragg peaks corresponding to the two degenerate VL orientations are observed as seen in Figs. 4.4(a) and 4.4(c).

The angular rotation $\Delta\varphi$ of the VL Bragg peak as a function of field and Ω is summarized in Fig. 4.5. At each Ω, the rotation is measured relative to the peak position in the F phase at 0.3 T, corresponding to the projection of the a axis onto the scattering plane, as shown in Figs. 4.4(c) and 4.4(d). For $\Omega = 0$, we observe the same VL rotation reported earlier [30], associated with the progression through the L

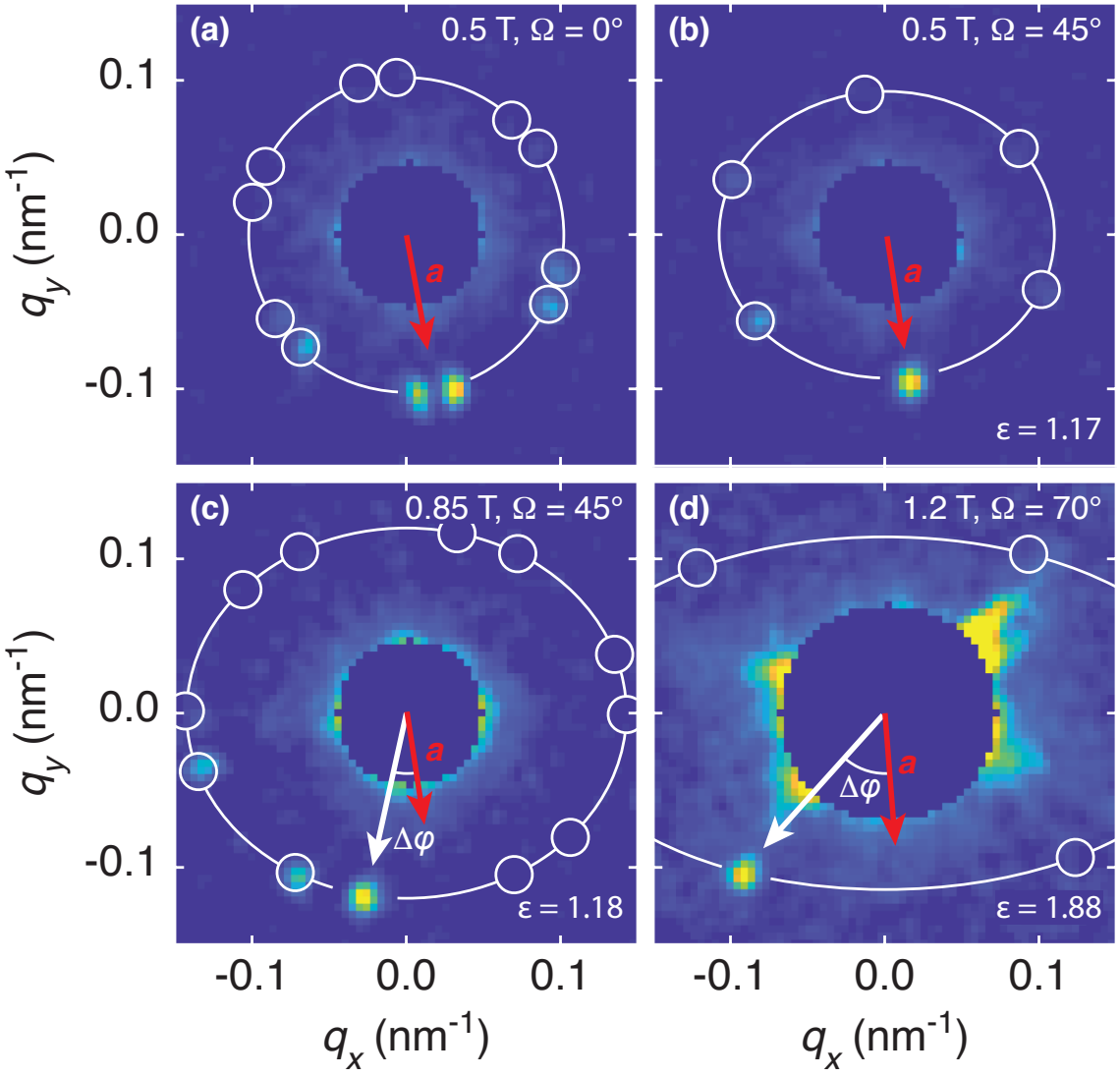

Figure 4.4. Vortex lattice diffraction patterns at (a) $H = 0.5$ T and $\Omega = 0°$, (b) 0.5 T and 45°, (c) 0.85 T and 45°, and (d) 1.2 T and 70°. In all cases only a single (in (a) and (c) split) peak fully satisfy the Bragg condition. The other peaks are indicated by open circles in their predicted locations. For each diffraction pattern the fitted geometric anisotropy (ε) is indicated. All measurements were performed following a damped field oscillation. Background scattering near the detector center is masked off.

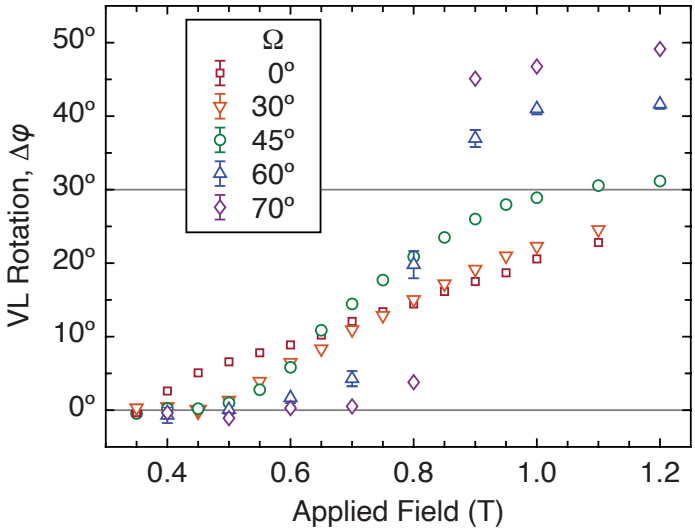

Figure 4.5. Rotation of the VL Bragg peaks around $q = 0$ as a function of field for different Ω. Angles are measured with respect to the VL orientation at 0.3 T (F phase). Error bars represent one standard deviation.

phase. In the L phase, where the VL Bragg peaks are split, we show the orientation of the clockwise rotating domain. As Ω is increased, the VL distortion allows the rotation of peaks which start near the minor axis to exceed the 30° range for the F to I transition when $H \parallel c$. This is seen most clearly at $\Omega = 70°$, where the VL rotation approaches 50° at 1.2 T.

The location of the VL peak positions in the SANS data are governed by two separate effects: the VL rotation transition within the L phase, and the geometric distortion due to the penetration depth anisotropy discussed above. To analyze the progression of the rotation transition it is useful to first remove the effect of the geometric distortion, which corresponds to mapping the VL Bragg peaks positions from lying on an ellipse back onto a circle. Due to flux quantization, the area of the circle in reciprocal space must be the same as the original ellipse, and the transformation can treated as a squeeze mapping of all points (q'_x, q'_y) in the circle to all points (q_x, q_y)

in the ellipse:

$$\begin{pmatrix} q'_x \\ q'_y \end{pmatrix} = \begin{pmatrix} \varepsilon^{-1/2} & 0 \\ 0 & \varepsilon^{1/2} \end{pmatrix} \begin{pmatrix} q_x \\ q_y \end{pmatrix}. \tag{4.1}$$

Converting to polar coordinates (q', φ') and (q, φ), and solving for ε yields a transcendental equation that can be solved numerically given any point on the ellipse:

$$\varepsilon^{1/2} = \frac{q'}{q \sin\varphi} \sin\left(\arccos\left[\frac{q\,\cos\varphi}{q'\,\varepsilon^{1/2}}\right]\right). \tag{4.2}$$

Values of q and φ are determined from 2D Gaussian fits to VL Bragg peaks on the SANS detector, and q' is determined from the measurement performed at the same applied field with $\Omega = 0$. Once ε is determined, the re-scaled VL orientation φ' is given by

$$\varphi' = \arccos\left[\frac{q\,\cos\varphi}{q'\,\varepsilon^{1/2}}\right], \tag{4.3}$$

Finally, the rescaled VL rotations can be calculated by subtracting the VL orientation at 0.3 T

$$\Delta\varphi'(H, \Omega) = \varphi'(H, \Omega) - \varphi'(0.3\ T, \Omega), \tag{4.4}$$

and are shown in Fig. 4.6. The transformation rescales the VL rotation so that the phase transition always occurs in the range $\Delta\varphi' = 0°$ to $30°$ for all Ω, consistent with the L phase behavior for $H \parallel c$. It is important to note here that nowhere in the squeeze mapping analysis have we specified that the rotations should fall on the range $\Delta\varphi' = 0°$ to $30°$. Rather, the fact these rotations do fall into that range serves as verification that we are suitably isolating the behavior of the L phase from the elliptical distortion.

From Fig. 4.6 it is clear that the VL phase diagram changes dramatically with increasing Ω. Firstly, the onset of the rotation transition moves to higher fields, indicating that the F phase ($\Delta\varphi' = 0°$) is expanding. Secondly, once the rotation does begin, it occurs more rapidly at high Ω. Thirdly, the L phase ($0° < \Delta\varphi' < 30°$)

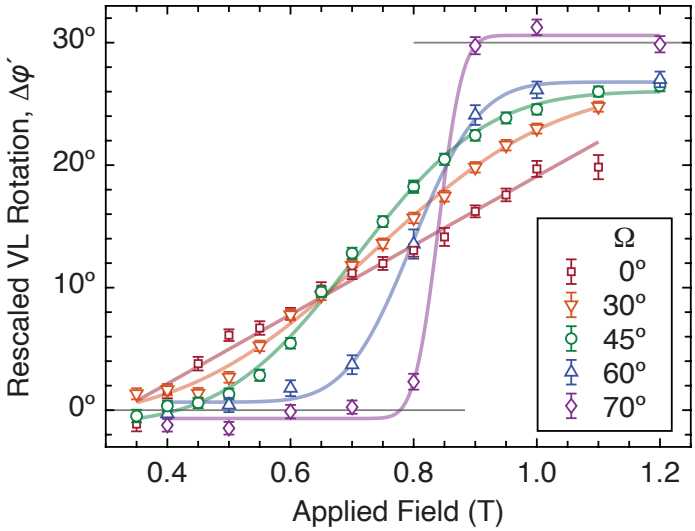

Figure 4.6. Rescaled VL rotation corresponding to Fig. 4.5 using Eqs. (4.2) – (4.4), showing the evolution of VL rotation transition.

either becomes very narrow or vanishes entirely for $\Omega > 70°$. This would correspond to a discontinuous phase transition directly from the F to the I phase ($\Delta\varphi' = 30°$).

The increasingly abrupt rotation transition is also evident in the extracted VL distortion $\sqrt{\varepsilon}$, which is plotted as a function of field and Ω in Fig. 4.7. This graph shows an abrupt jump in the slope of $\sqrt{\varepsilon}$ versus field for $\Omega \geq 60°$. Here we note that the field dependence of ε at *constant* Ω is due to the gradual suppression of superconductivity on the π-band.[29] This rise in ε with respect to field is similar to phenomena observed in V_3Si [27], $2H$-$NbSe_2$ [44], and Sr_2RuO_4 [74].

4.4 Discussion

As discussed in 1.1, the VL phase diagram in MgB_2 can be modeled by a free energy

$$\delta F(\Delta\varphi') = K_6 \cos(6\,\Delta\varphi') + K_{12} \cos(12\,\Delta\varphi'), \tag{4.5}$$

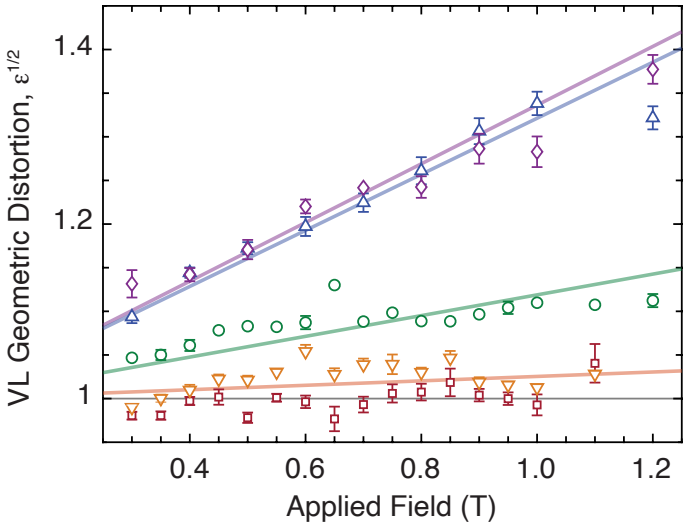

Figure 4.7. Square root of the geometric distortion, ε, as a function of field and field angle Ω. Linear fits to each curve are also shown.

containing six- and twelve-fold anisotropy terms. This expression is the same as Equation 1.39, with the substitution that φ is our measurable quantity $\Delta\varphi$. This form of the free energy was originally proposed for $H \parallel c$ where $\varphi' = \varphi$ [137, 30, 108], but here it is generalized to non-zero Ω. In this model K_{12} is positive, and the continuous rotation transition in the L phase occurs when the anisotropy ratio $\kappa = K_6/K_{12}$ is varied between -4 and 4. Note that if K_{12} was negative, the VL would undergo a discontinuous reorientation transition between the F and I phases when K_6 changes sign. For each measurement it is possible to calculate the anisotropy ratio

$$\kappa = -4\cos\left(6\,\Delta\varphi'\right), \tag{4.6}$$

obtained from a minimization of the free energy in Eq. (4.5). This is shown in Fig. 4.8, and is seen to mimic the behavior of the re-scaled rotation angle $\Delta\varphi'$. We note that actual values of κ most likely extend outside the ± 4 range allowed by Eq. (4.6). However, this does not affect the analysis below as it focuses on the region where κ

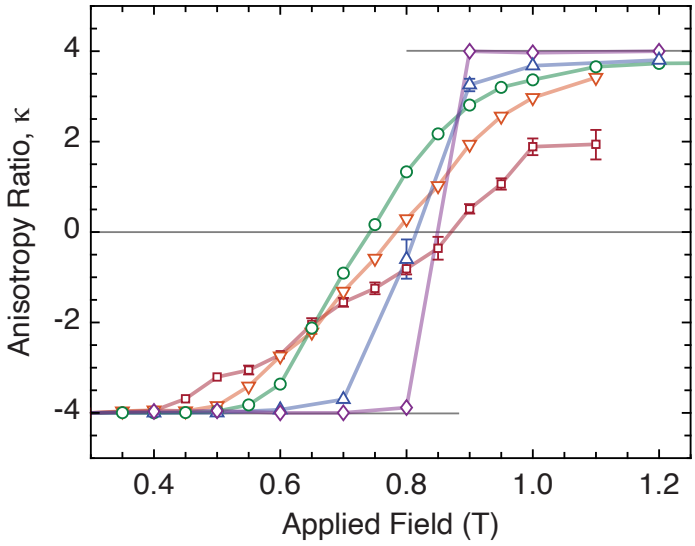

Figure 4.8. Anisotropy ratio, κ, as a function of field and field angle, calculated from Equation 4.6.

is close to zero.

The increasingly abrupt transition seen in Figs. 4.6 and 4.8 suggests a reduction and possible sign change of K_{12} as Ω increases. It is possible to model the increasingly rapid reorientation transition by Taylor expanding K_6 to linear order around the critical field H_0 where K_6, and thus κ, vanish:

$$K_6(H) \approx \alpha_6(H - H_0) \tag{4.7}$$

Here, α_6 is an undetermined constant. The slope of κ with respect to field near the transition at $H = H_0$ is then an indirect measure of K_{12}:

$$\left.\frac{\partial \kappa}{\partial H}\right|_{H=H_0} = \frac{\alpha_6}{K_{12}}, \tag{4.8}$$

where we have taken K_{12} to be field independent. Figure 4.9 shows the inverse slope $(\partial\kappa/\partial H)^{-1}$ measured near $\kappa = 0$ for each Ω. The inverse slope depends linearly

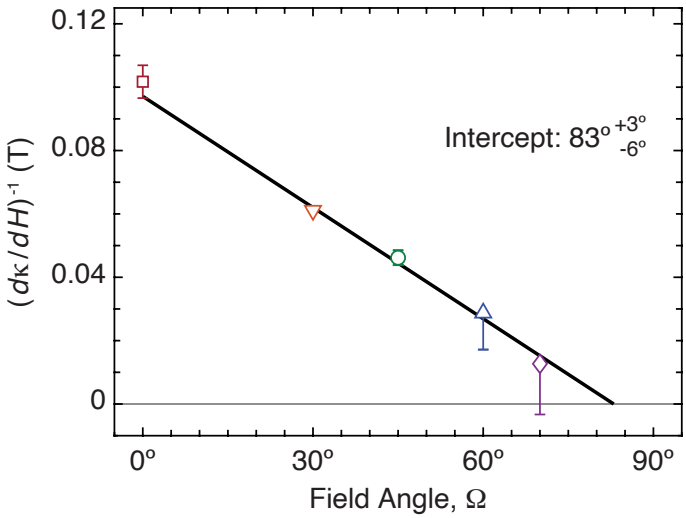

Figure 4.9. Inverse slope of the anisotropy ratio near $\kappa = 0$ as a function of Ω. The linear fit is then extrapolated to a $K_{12}/\alpha_6 = 0$ intercept of $\Omega = \left(83^{+3}_{-6}\right)^{\circ}$.

on Ω, suggesting a functional form for K_{12}:

$$K_{12}(\Omega) = \alpha_{12}(\Omega - \Omega_0) \tag{4.9}$$

Extrapolating to $K_{12}/\alpha_6 = 0$, we find an estimate for $\Omega_0 = \left(83^{+3}_{-6}\right)^{\circ}$. For values of $\Omega > \Omega_0$, K_{12} will be negative and the VL transition will become first-order between the F and I phases. We note that it is possible that this is already the case at $\Omega = 70°$, as the uncertainly on $(\partial\kappa/\partial H)^{-1}$ at this angle extends to negative values. Qualitatively similar behavior has been observed in YBCO [133], where a triangular to square VL transition switches from second to first order at a critical angle of 10°. The much smaller Ω_0 for YBCO is likely due to the highly two-dimensional nature of this material, making in relatively more susceptible to field rotations away from the c axis.

Finally, we return to the question of whether rotating the applied field away from the c axis will break the VL domain degeneracy within the L phase. Such an

effect was previously observed in $TmNi_2B_2C$ where the VL undergoes a triangular to square transition with a degenerate intermediate rhombic phase [36], and where rotating the field away from the c axis by $\approx 10^\circ$ is sufficient to suppress one of the two rhombic domains [32]. In an ideal uniaxial superconductor with an isotropic basal plane, London theory predicts that the two-fold anisotropy introduced by field rotation will favor a VL orientation with Bragg peaks on the minor axis of the ellipse in reciprocal space [24]. However, any real material will exhibit some basal plane anisotropy which may compete with the uniaxial effect, and the relative strength of the two will determine the VL orientation. As example one can consider $NbSe_2$, where the triangular VL is oriented in a manner corresponding to the maximal energy according to the London theory [44].

In our SANS measurements the MgB_2 crystal was mounted such that within the L phase Bragg peaks for one of the domains lie near the vertical axis, as seen in Fig. 4.4(a), and are thus favored by the uniaxial effect. However, peaks corresponding to both L phase domains were clearly observed at $\Omega = 45^\circ$and 0.6 T and at 60° and 0.9 T, indicating that the degeneracy is not readily lifted in MgB_2. This suggests that at these values of Ω the uniaxial anisotropy is weaker than K_{12}, and that a suppression of the degeneracy will only occur near Ω_0. It is also consistent with the inability of the uniaxial effect to cause a VL reorientation in the F phases to have the Bragg peaks on the minor axis of the ellipse, since K_6 and K_{12} are of the same order of magnitude except in the immediate vicinity of H_0 and Ω_0. That said, the uniaxial anisotropy does appear to lower the free energy of the F phase relative to the I phase, causing H_0 to shift to higher fields in Fig. 4.6 and 4.8 as $\Omega \to \Omega_0$. This conclusion is supported by previous SANS measurements where the magnetic field was rotated about the a^* [111]. Here the L phase (rather than the F phase) is favored by the uniaxial anisotropy, and at 0.4 T the critical angle is shifted to a lower value $\Omega_0 \sim 70^\circ$.

4.5 Conclusion

In summary, we have demonstrated how the continuous (second order) VL rotation transition observed in MgB_2 for $H \parallel c$ gradually evolves towards and finally becomes discontinuous (first order) as the applied magnetic field is rotated away from the c axis by $\sim 83^\circ$. For rotation angles below this critical value, domain formation in the intermediate L phase persists. We speculate that the long lived metastable VL phases, attributed to domain formation in the L phase, will thus no longer occur above the critical angle, and should be the subject of further SANS studies.

CHAPTER 5

SKYRMION LATTICE DYNAMICS IN NOVEL CURRENT FIELDS

5.1 Motivation

Numerous SANS measurements have used electric current to drive motion of the skyrmion lattice (SkL) in MnSi [63, 107]. However, since linear translation of the SkL is not visible in reciprocal space, all of these experiments have relied on secondary effects to convert the force exerted by the current into a net rotation of the SkL. Some of the clever techniques used to achieve this include applying a thermal gradient across the sample so the spin current density is no longer constant [63] and measuring SANS only near the edge of the sample where the outermost skyrmions get pinned [107].

In these cases, it hard to decouple the impact of the current on the SkL from the impact of the secondary effects. For this reason, we have sought to build a device which could exert a net torque on the SkL without relying on other physics. In pursuit of this, we have collaborated with W.-K. Kwok and U. Welp at Argonne National Laboratory to build Corbino disks [28] out of single crystal MnSi (Fig. 5.1). By driving current radially through the sample, the SkL will experience a Magnus torque about the center of the disk which will drive the SkL into rotation.

The direct coupling between the current and the SkL enabled by this device has numerous advantages. Firstly, we anticipate that the direct coupling will produce SANS-observable skyrmion motion at lower current densities than previously reported. This opens the door to explore skyrmion motion at current densities that are higher proportional to j_c than previously observed. Furthermore, since the SkL

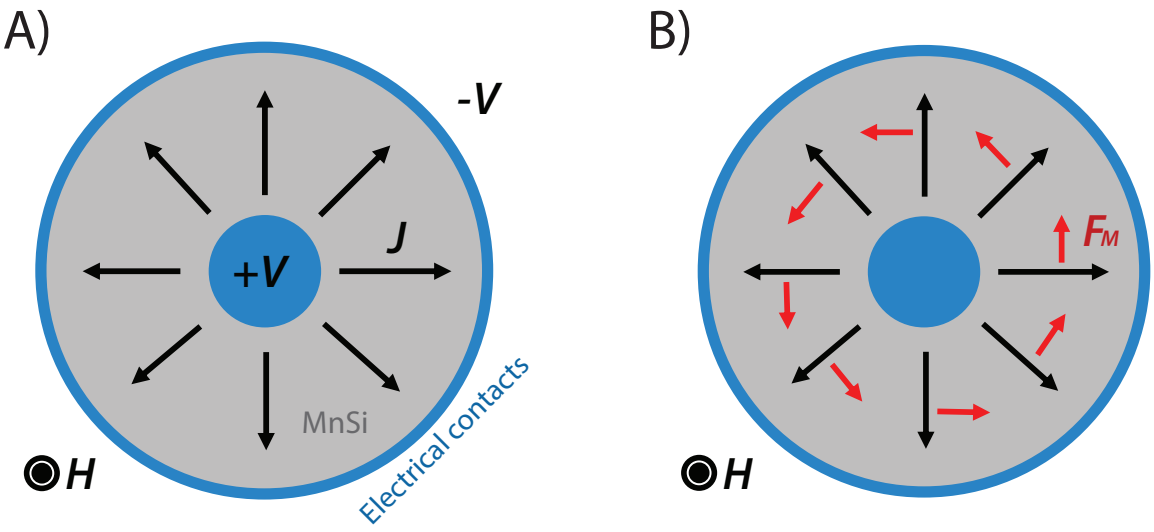

Figure 5.1. A) Current flow through a Corbino disk of MnSi. B) Magnus force F_M exerted on the SkL.

alignment will now be determined by the balance between the Magnus torque and the SkL-crystal lattice force, we will be able to map the free energy of the crystal lattice interaction by measuring the rotation angle as a function of current. Finally, the radial decay of current density through the Corbino device can be used as a probe of the elastic properties of the SkL. Since the drag force will be greater at the center than the outside edge, the drag force will exert a net compressive strain (or tensile strain depending on current direction) on the lattice. Similarly, the radial decay of the Magnus force will result in a net shear strain on the SkL. Pushed to the extreme, these forces could even result in a breakdown of the crystallinity of the SkL, first into domains, and then perhaps into a skyrmion-fluid phase by analogy to what occurs in superconducting VLs [93]. Both of these effects could be independently observed with SANS, as shown in Fig. 5.2.

The following chapter discusses the protocols that have been developed at Argonne National Laboratory for constructing a Corbino device out of MnSi single crystals.

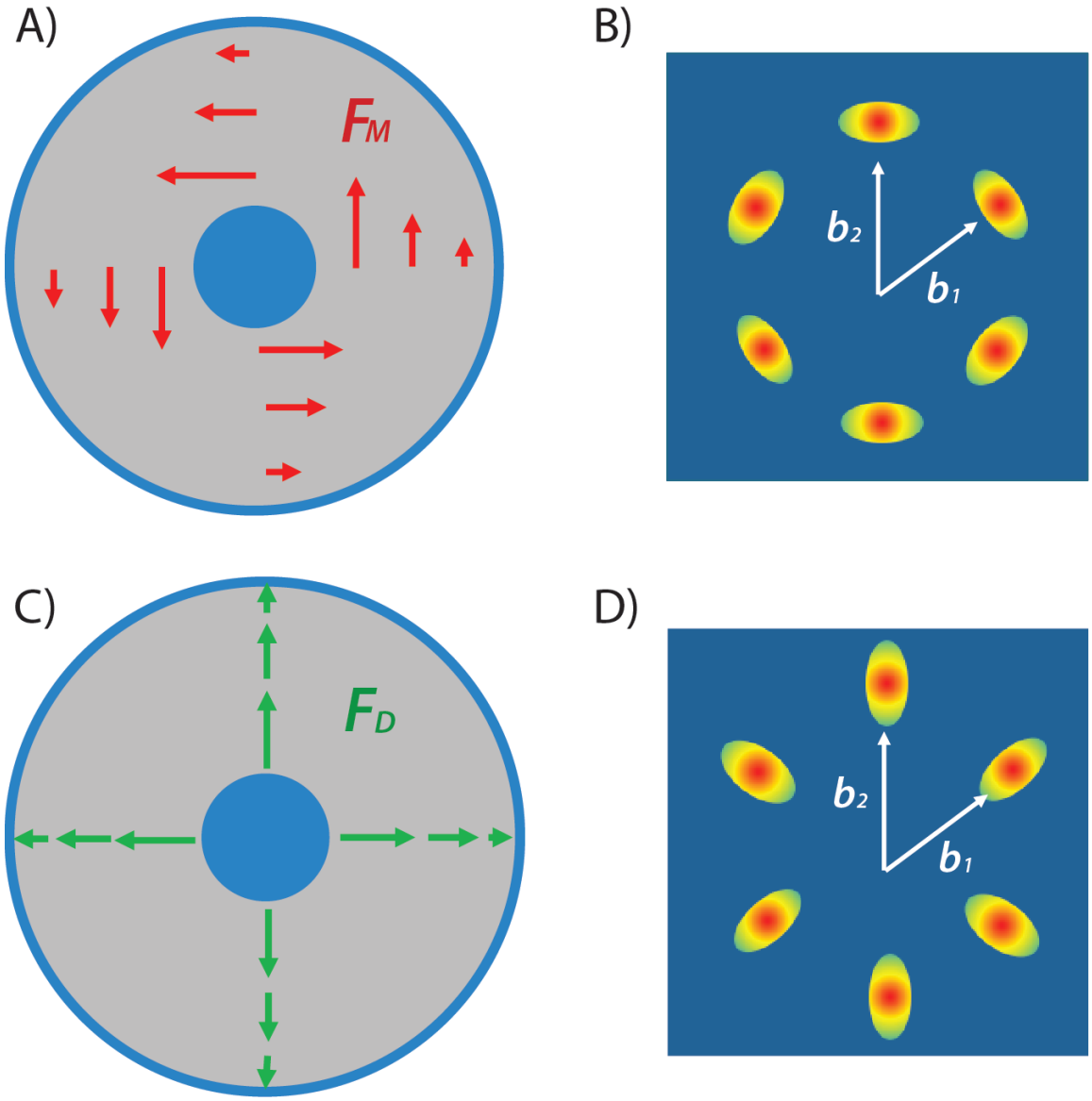

Figure 5.2. A) Radially decaying Magnus force F_M. B) Resultant azimuthal broadening of SANS diffraction pattern due to shear strain. C) Radially decaying drag force F_D. B) Resultant radial broadening of SANS diffraction pattern due to compressive/ shear strain.

Additionally, magnetotransport measurements have been performed to characterize the behavior of these devices at different temperatures and applied fields. Finally, a prioritized list of future SANS experiments on these Corbino devices is discussed. Due to the COVID-19 pandemic, these experiments have not yet been performed, however they have been scheduled for the Summer of 2021 at the Insitut Laue Langevin and the Paul Scherrer Institute.

5.2 Corbino Device Construction

5.2.1 Crystal Growth and Cutting

To produce single crystals of MnSi with suitable radii for a Corbino device, large crystals have been grown via the Bridgman method [21]. This method produces long cylindrical ingots with a radius determined by the inner diameter of the crucible ($\sim$6 mm). From here, the ingot is then cut into circular slices using a diamond wire saw. As these slices are eventually going to be polished very thin, it is important that each disk be cut as thin as possible to minimize wasted crystal. On the other hand, cutting the slices too thin risks fracturing the naturally delicate crystals during the cutting process. Trial and error have found the optimal thickness to be between 1 and 1.5 mm.

5.2.2 Crystal Polishing

In order to minimize the total input current required to produce the critical current density required to move the SkL, and to maximize the cooling of the sample while in situ, it is critical to polish the sample as thin as possible. On the other hand, SANS from the SkL is directly proportional to the illuminated sample volume, and so polishing too thin may make measurements take unfeasibly long. Based on experience with other SANS measurements of MnSi (Chapter 3), reasonable length

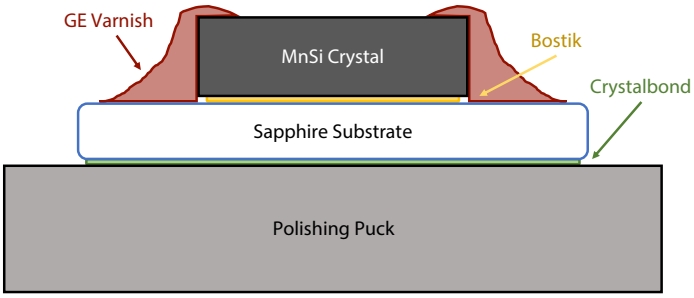

Figure 5.3. Crystal mounting schematic for precise polishing of large MnSi crystals.

measurements of the SkL can achieved with roughly 1 mm^3 MnSi. Assuming the maximum Bridgman ingot width of 6 mm, a reasonably strong SANS signal could be produced from a 50 μm thick disk. However, to account for the additional sample volume that will have to be masked off from the neutron beam to avoid background scattering (e.g. all electrical contacts and temperature probes), samples have been polished to roughly 200 μm.

In order to polish the crystal to such a large aspect ratio (roughly 30:1), precautions must be taken. The developed procedure is as follows:

1. *Ensure the starting faces are parallel.* This is most easily accomplished by cutting the second face immediately after the first, using the translation stage of the wire saw to move the crystal exactly perpendicular to the blade between cuts.

2. *Mount the disk to a sapphire substrate with a low-scattering adhesive.* Sapphire is an ideal substrate as it is near-invisible in SANS, and it provides extremely high thermal conductivity at low temperatures for heat sinking. In the preliminary work, Meller Optics, Inc sapphire windows have been used [2]. For adhesive, Bostik glue diluted with acetone to reduce viscosity has been used.

3. *Reinforce edges of crystal with a rigid adhesive.* In order to ensure that the crystal edges do not get rounded off and to minimize the risk of fracturing the entire crystal during polishing, the disk needs to be supported on all sides by a hard adhesive. Here, Lakeshore VGE-7031 varnish has been applied along the edges of the crystal and allowed to cure overnight at room temperature. DO NOT attempt to accelerate this cure via heating, as large bubbles will form and weaken the support of the crystal.

4. *Mount the sapphire substrate onto the polishing puck using Crystalbond.* It is very important to press the sapphire into the Crystalbond firmly in order to ensure that it is flush against the puck. At this point, the system should look like Fig. 5.3.

5. *Level off the polishing surface* Starting with a moderately smooth sandpaper (600 grit), polish the sample until the entire surface of the MnSi has made contact with the polisher. MnSi becomes visibly shinier as it begins polishing, and so once the entire surface of the disk is shiny the surface is now polishing uniformly.

6. *Measure the starting crystal thickness* At this point, it is good to take a preliminary measurement of the thickness of the crystal. This can be accomplished in one of two ways after removing the puck from the polisher.

   Firstly, the mounted crystal-sapphire-puck system can be placed into an digital caliper. It is good practice to protect the surface of the crystal from the blades of the caliper by sandwiching a KimWipe or weighing paper between the surfaces. Repeating this measurement technique can provide a precise measurement of the amount of material removed, however it is not easy to measure the absolute thickness of the MnSi.

   Alternatively, an optical microscope can be use to measure the absolute thickness of the MnSi crystal due to the transparent nature of VGE varnish. This can be done by focusing the microscope on the surface of the MnSi and then counting the rotations of the fine focus adjustment required to focus on the sapphire substrate underneath. This technique needs to be calibrated for each microscope using a transparent object of known thickness (microscope cover glasses work well).

   In practice, it is often useful to use a combination of these techniques, first the microscope to determine the starting thickness of the crystal, then the caliper to quickly and precisely measure the removed material.

7. *Polish to desired thickness.* From this point, polishing technique is a matter of preference and patience. I normally polish to a thickness of roughly $\sim$500 μm with 600 grit before switching to 1200 grit out of caution, checking the thickness every 15-30 minutes depending on how fast the thickness is reducing. Here, it is important to note that both the sandpaper and crystal become smoother through polishing, so polishing rate will decay rapidly the longer a sheet of sandpaper is used.

8. *Remove from polishing puck.* Once the desired thickness is achieved, return the polishing puck to a hotplate and remove the sample.

5.2.3 Applying Electrical Contacts

To minimize Joule heating of the Corbino disk during operation, it is critical that the current leads have a very low contact resistance to the crystal. MnSi like

most metals forms a thin, insulating oxide layer when exposed to atmosphere, which inhibits easy electrical connection. Soldering with flux is an ideal technique for simultaneously removing the oxide layer from a metal and then applying a strong electrical contact to the pure metal surface, however the high temperatures required to melt tin-lead solders risks cracking thin crystals. For this reason, a protocol has been developed for soldering indium to MnSi at much lower temperatures:

1. *Preparation.* Preheat a hot plate to 200 °C. Cut In 97/ Ag 3 solder into very small pieces, roughly the size of desired contacts.
2. *Place flux at desired contact points.* Working under a microscope, use a sharp point to place a small droplet of Indium Corp. Flux #3. This is an aggressive, water soluble flux intended to be used on strong oxides like that of stainless steel, however it works well on MnSi. Generally, it is best to start with minimal flux to avoid causing the solder point to spread too broadly across the crystal surface.
3. *Apply the solder.* Use tweezers to place a piece of solder onto the droplet of flux. The viscosity of the flux generally allows the solder to stick to the surface well once placed.
4. *Melt the solder.* Once satisfied with the solder placement, transfer the sample to the preheated hot plate and cover with a beaker to trap heat. Once the solder has melted ($\sim$10 minutes), remove from heat.
5. *Rinse the sample.* Once the sample has cooled for $\sim$5 minutes, use tweezers to gently swirl the sample in room temperature deionized water to remove excess flux.
6. *Inspect the connection.* Like any other good solder connection, the indium solder point should be shiny, well adhered, and domed on the surface of the crystal. Bad solder connections will bead up on the surface of the MnSi and fall off at the slightest poke (or during the rinsing process).

In order to apply the outer ring Corbino contact, many separate solder connections are made to the outside edge of the crystal (Fig. 5.4.B). These contacts must be separate, for if they are allowed to touch during the soldering process the surface tension of the molten indium will distort the contact placement. Once the solder connections to the crystal are satisfactory, the current leads must be soldered into position. This follows another procedure

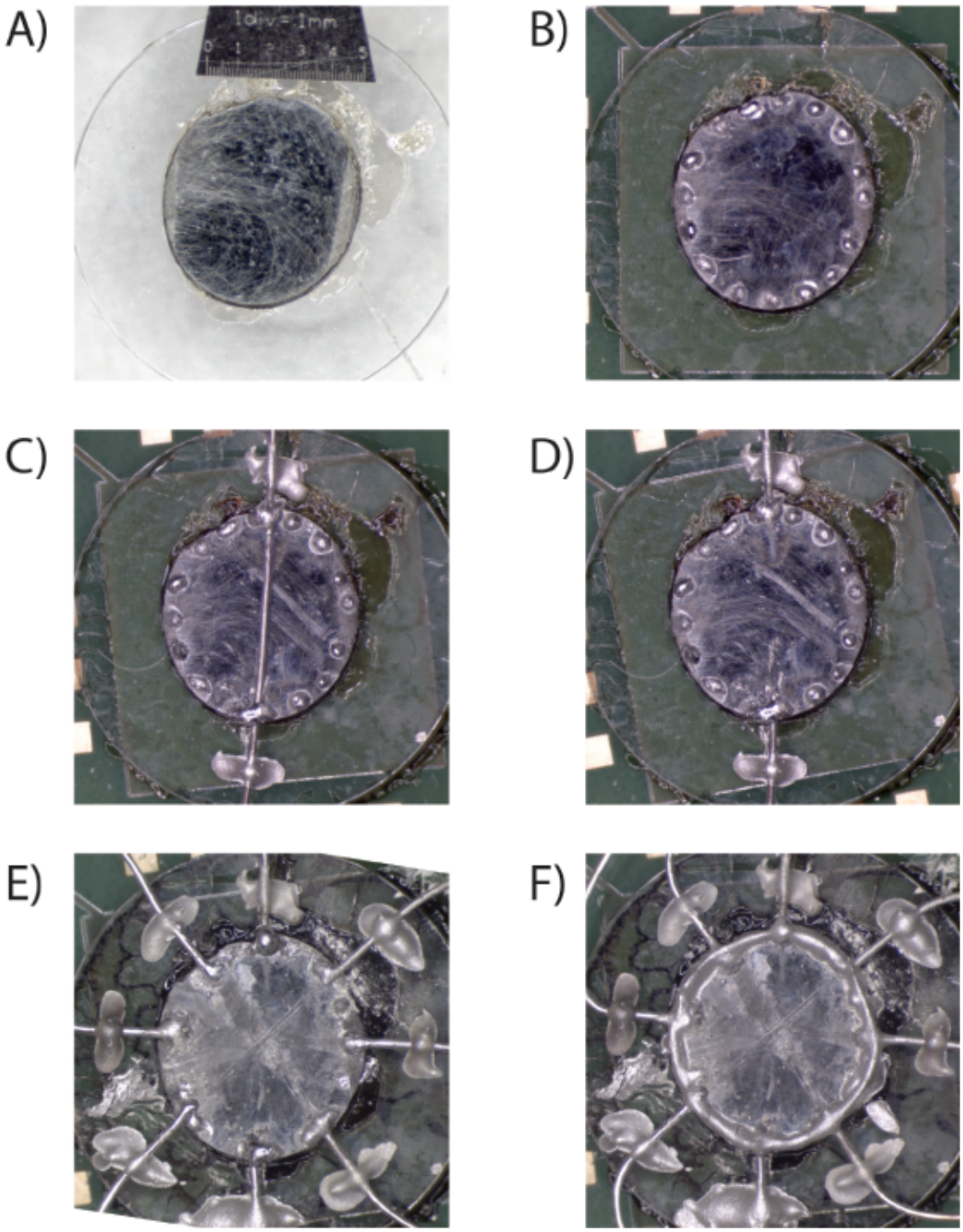

Figure 5.4. A) Polished MnSi crystal mounted onto a sapphire substrate. Crystal is 350 microns thick. B) Solder points applied along the edges of the crystal. C) Silver wire mounted and soldered. D) Cut wire, splitting it into two separate contacts. E) All eight contacts applied to the crystal. F) Contacts reinforced with silver epoxy.

1. *Position wire* A silver wire is mounted to the sapphire substrate using EPOTEK H20E epoxy such that it spans the crystal radially. This will provide the mechanical support for the solder connection (Fig. 5.4.C).
2. *Solder the wire* Add slightly more solder and flux to the points on the wire where the connection is to be made, and reheat on the 200 °C hotplate. After a few minutes, the solder connection should be made (Fig. 5.4.C).
3. *Inspect the connection* After cooling, a shiny clean solder connection should be rigidly holding the wire to both sides of the crystal. If connection is poor, reheat and add slightly more flux.
4. *Cut excess wire* Once both connections seem good, cut the excess wire spanning the crystal to produce two separate contacts (Fig. 5.4.D).

This process is repeated four times to produce eight separate radial contacts to the crystal (Fig. 5.4.E). At this point, the contact resistance between each pairs of wires should be checked to make sure all eight connections are good. If not, reheat and try adding slightly more flux. Once all connections are good, they are reinforced with a layer of EPOTEK H20E conductive epoxy to connect all the solder points together and further ensure an even current distribution (Fig. 5.4.F).

For the central Corbino contact, one slightly larger solder point is made at the center of the disk. Choice of wire to connect this contact is a bit more complicated than for the outer wires. On one hand, this wire must be able to handle all the current of the eight outer wires combined. However, the thicker this wire is made, the larger the "shadow" it casts on the crystal underneath, and the more of our sample that has to be masked off from the neutron beam. For these reasons, we have elected to use a thin, high temperature superconducting (HTS) wire from Superpower to connect to the central contact. This ribbon wire is mounted edge-on with Stycast epoxy to minimize shadowing of the sample, and then an indium solder connection is made (Fig. 5.5).

Finally, it is useful to add two voltage leads to the crystal so that its resistance (and therefore temperature) can be monitored in situ. Since these leads will not carry much current, contact resistances do not pose as much of a problem, and thin gold

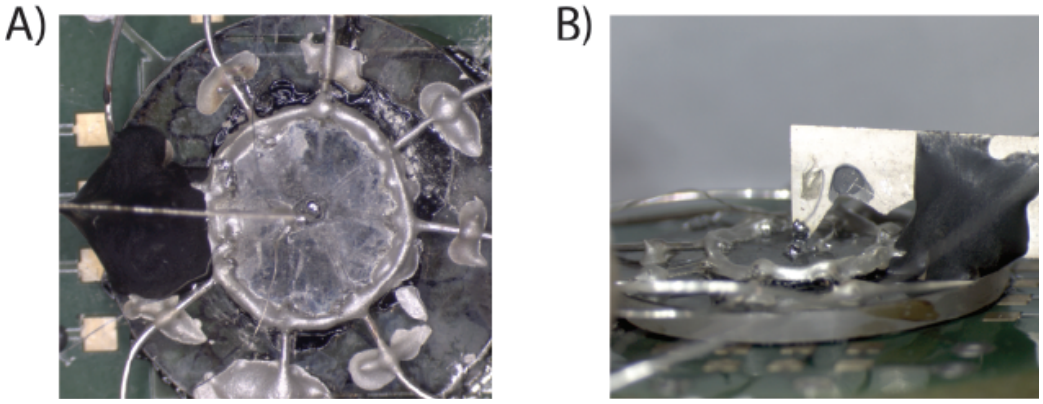

Figure 5.5. A) Top view of HTS wire soldered to Corbino disk. B) Side view of HTS wire.

wires can be attached directly to the MnSi surface with EPOTEK conductive epoxy. For experimental convenience, these contacts are placed in the shadow of the central contact wire. Additionally, similar voltage probes have been added to the HTS wire so that its resistance (or hopefully lack thereof) can be monitored during operation.

5.3 Device Characterization

In order to confirm that a Corbino device is performing adequately, it is necessary to take several characterization measurements before the SANS experiment.

The first and easiest measurement to perform is to check the contact resistances of the electrical leads. This can be done by using a digital multimeter to measure the resistance between each pair of wires on the Corbino. By measuring all possible pairs of wires (and by neglecting the resistance of the crystal which is negligible), it is possible to determine the contact resistance of each wire. Contact resistances for the current leads must be below 1 Ohm to ensure minimal Joule heating while the device is in operation. Contact resistances for the voltage leads can be greater, as much less current will be passing through them, however good quality contacts should be connected to the crystal with less than 50 Ohms of resistance.

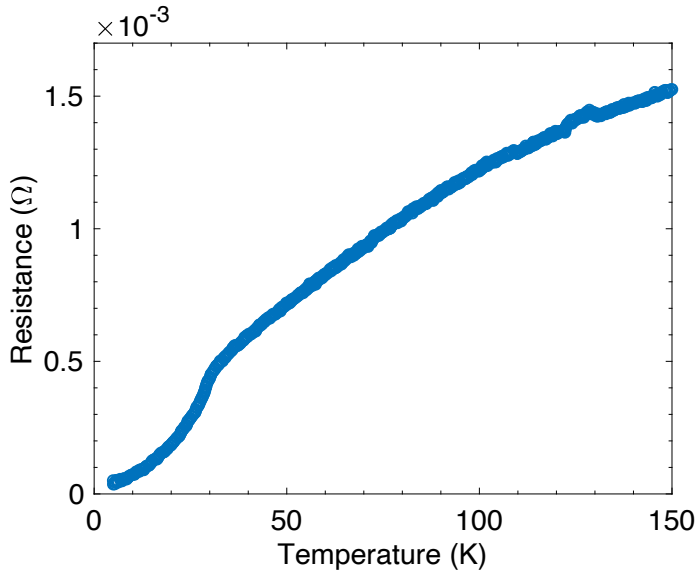

Figure 5.6. R vs T curve for single crystal MnSi. Note the kink in resistivity near 28 K corresponding to T_N. For this sample, $RRR \approx 70$.

The next step to characterizing the device is to confirm that the quality of the MnSi single crystal has been maintained. This can be done by measuring the four point resistance of the Corbino as it is cooled from room temperature to ∼2 K (Fig. 5.6). We can then calculate the residual-resistance ratio (RRR) as

$$RRR = \frac{R(300K)}{R(\sim 2K)} \tag{5.1}$$

As long as the quality of the crystal has been maintained, the RRR of the Corbino should be above $RRR = 50$.

Assuming the previous measurements are promising, the final step to characterize the Corbino is to measure its four-point resistance as a function of temperature in field in the A Phase. Specifically, R vs T curves should be performed at several fields near the A Phase center (e.g. 0.19 T, 0.195 T, 0.20 T, 0.205 T, and 0.21 T etc). These curves can then be used for temperature calibration during the SANS experiments.

5.4 Future SANS Measurements

SANS experiments on the Corbino have been approved at ILL, PSI, and NIST. The combination of these three experiments as well as the possibility to make adjustments to the device between experiments should allow us to explore a wide parameter space during this time. Below are a list of possible SANS measurements in order of priority:

1. *Locate the A Phase.* Once the magnet is aligned, locate the center of the A phase by performing temperature and field sweeps and searching for the maximal SANS intensity. At the A phase center, apply a small current ($\sim$5 mA) and measure the four point resistance of the disk ($R_{corbino}$). This resistance can then be compared to the previous R vs T measurements to determine the true sample temperature.

2. *Confirm SkL rotation at j_c.* Gradually increase current through the device while monitoring $R_{corbino}$ to make sure that it does not leave the A Phase. At some point it may become necessary to increase the cooling power of the cryostat by increasing the exchange gas and/or reducing the setpoint of the variable temperature insert (VTI). Near 0.5 A, the SkL near the center of the disk should start to rotate. It may also be useful at this point to determine the maximal current at which Joule heating causes the SANS signal to disappear (j_{max}).

3. *Map the SkL-crystal interaction.* Illuminating the entire disk, measure the SkL rotation as a function of current from j_c to j_{max}. This can later be used to plot the interaction potential by integrating the Magnus torque along the rotation.

4. *Search for deformations of the SkL.* Precisely measure the radial and azimuthal widths of the Bragg peak both with and without applied current. Additionally, rocking curve measurements could be performed to determine the longitudinal width of the Bragg peaks and determine if the skyrmions are being distorted along the field direction when current is applied.

5. *Measure the spatial variance of rotation.* Place a small aperture in the neutron beam and measure the rotation of the SkL as a function of radius within the disk. This information will help distinguish between elastic deformation of the SkL and fracturing of the SkL into microscopic domains.

6. *Measure properties of the strained SkL A Phase* Set the current to a fixed value above j_c. Perform temperature and field sweeps to determine if the shape of the A Phase has changed, and/or if the activation barrier has changed.

CHAPTER 6

CONCLUSION

In this dissertation we have discussed three projects where SANS has been pushed to its limits to explore the energetics and symmetries of magnetic vortices.

In Chapter 3, we observed a small hysteresis effect associated with crossing the SkL-conical phase transition in MnSi, and were able to demonstrate that this is a direct result of the topological stability of individual skyrmions. The hysteresis was then modelled with an adapted Preisach model, which showed that the activation barrier was uniform throughout the entire crystal and was a function of the field history. Finally, by comparing our activation barrier with atomistic spin simulations, we were able to confirm that the SkL forms progressively in domains of hundreds of skyrmions, with the topological energy barrier of several eV per skyrmion.

In Chapter 4 we discovered that the VL phase diagram of MgB_2 changes dramatically as the applied field is rotated away from the crystalline c axis. The domain-split L phase shrinks as the field gets closer to the ab plane, and above a critical angle $\Omega_0 \approx 83^\circ$ disappears entirely. This can be understood as a result of a decreasing (and possible sign change) of the 12 fold anisotropy in the VL plane. We suspect that this loss of anisotropy will suppress the notable VL metastability in MgB_2, but further measurements are necessary.

Finally, in Chapter 5, we have described a new architecture of skyrmion device which promises to efficiently convert electric current into rotation of the SkL. Constructing this Corbino device out of single crystal MnSi poses several technical challenges, and so a precise protocol has been developed at Argonne National Laboratory

to achieve this. We believe that this device will enable SANS studies of several interesting properties of the SkL, including a direct measurement of the SkL-crystal lattice interaction potential and possible observation of elastic and/or plastic deformations of the SkL.

APPENDIX A

RESISTIVE FIELD COILS

A.1 Mk 1

This coil was designed for the first experiment our group performed on MnSi (ILL June 2018). During the experiment, the coil was used to successfully wiggle the field at faster rates than allowed by the cryomagnet. However, as the coil was ramped, it was observed that usage of the coil was raising the temperature of the sample enough to significantly reduce SkL scattered intensity. By measuring the change in SANS intensity as a function of AC field frequency, it was determined that the coil was heating the crystal both through the induction of eddy currents in the crystal and direct thermal conduction of the heat produced by Joule heating of the copper wire windings. In this design, the copper wires and sample disk were only separated by a thin wall of PEEK plastic, so direct conduction of heat was significant. This motivated the creation of the Mk 2. Note: The magnet wire for this coil broke after the experiment at ILL and had to be repaired by soldering a new jumper wire when the breakage was discovered at NIST in September 2019.

Field calibration: Field[Gauss] = 0.3917*Current[mA] - 0.03 Gauss

Windings: $\sim$650, $\sim$480/cm

$\mathbf{R_{coil}}(@\mathbf{RT}) : \approx 50.5\ \Omega$

Figure A.1. Mk 1 resistive field coil. Bobbin has an oblong "horsetrack" shape to accommodate the large oval shaped crystal of MnSi that was used at ILL.

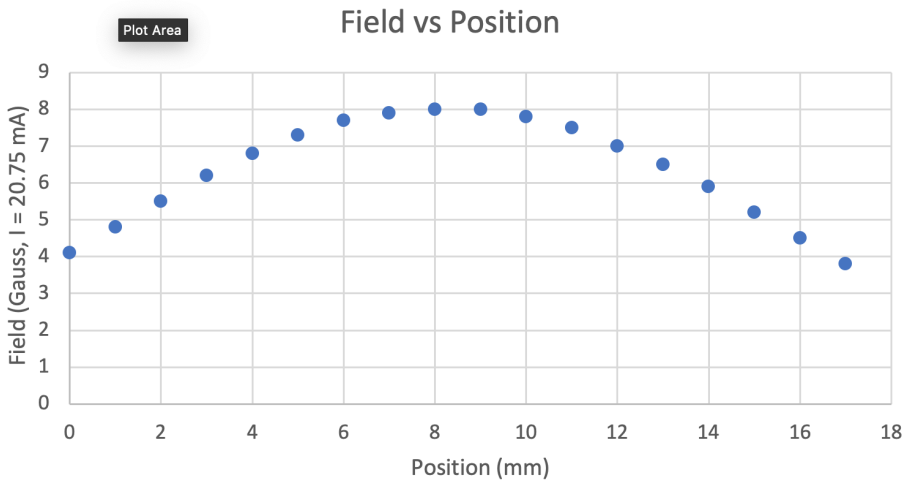

Figure A.2. Homogeneity of field in the Mk 1 coil. Hall probe was translated along the central axis of the coil. For the hysteresis experiment using this coil at ILL, the crystal was 3.5 mm thick and illuminated by a neutron beam with a 1 mm diameter.

A.2 Mk 2 aka The Gorgon

This coil was designed for use in the large bore cryostat at ORNL for our experiment on MnSi in September 2018. In order to insulate the sample from the Joule heating of the coil, the sample was attached to an alumina tube which was then isolated from the rest of the holder by two, three-legged "spider" made of PEEK. As an extra safety measure, a sapphire window was placed over top of the crystal, sealing it inside. Since the sample space was now thermally isolated from the rest of the sample stick, an additional Cernox sensor was mounted directly next to the sample to monitor temperature, and nichrome wire was wound around the outside of the alumina tube to serve as a heater. This heater wire was twisted around itself before winding so that it wound not alter the magnetic field in the sample space. The combination of the heater and Cernox sensor allows the temperature of the sample to be independently controlled by a Lakeshore or similar temperature controller.

Field calibration: Field[Gauss] = 0.871*Current[mA] + 1.89 Gauss

Windings: ∼3500, ∼1100/cm

$\mathbf{R_{coil}}(@\mathbf{RT}) : \approx 366\ \Omega$

$\mathbf{R_{Cernox}}(@\mathbf{RT}) : \approx 91.2\ \Omega$

$\mathbf{R_{heater}}(@\mathbf{RT}) \approx 53\ \Omega$

A.3 Mk 3

The Mk 3, like the Mk 2, uses a spider system to thermally isolate the crystal from the coil and has a Cernox sensor and nichrome heater for independent temperature control. However, the Mk 3 has a much smaller diameter, making it suitable for most cryomagnets.

Field calibration: Field[Gauss] = 0.5753*Current[mA] + 1.73 Gauss

Windings: ∼1000

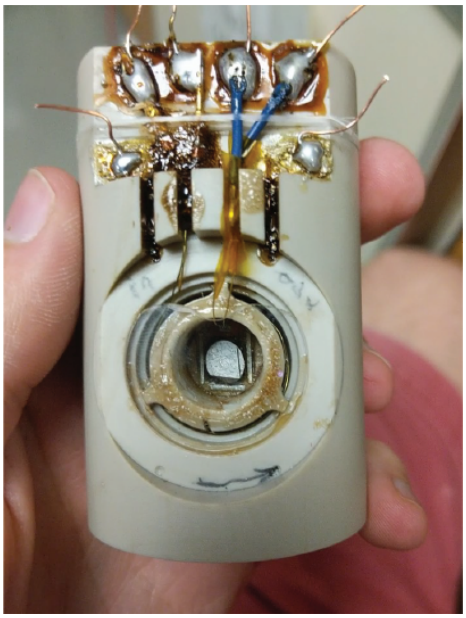

Figure A.3. Mk 2 resistive field coil. Coil has a much larger external diameter than the Mk 1, making it only suitable for cryomagnets with bore $\phi \geq 50$ mm. Mounted inside the coil is the large, roughly cylindrical crystal of MnSi used ILL and ORNL.

Figure A.4. Mk 3 resistive field coil. Coil has a much smaller external diameter than the Mk 2, making it suitable for cryomagnets with bore $\phi \geq$ 25 mm. Mounted inside the coil is the smaller, roughly rectangular crystal of MnSi used PSI and ANSTO.

$\mathbf{R_{coil}}(@\mathbf{RT}) : \approx 43.6\ \Omega$

$\mathbf{R_{Cernox}}(@\mathbf{RT}) : \approx 118\ \Omega$

$\mathbf{R_{heater}}(@\mathbf{RT}) \approx 43.6\ \Omega$

APPENDIX B

HYSTERESIS ANALYSIS SOFTWARE

Modelling the experimentally observed hysteresis with double-transition Preisach model described in Chapter 3 is a particularly challenging computational problem. The adapted Preisach model divides the illuminated MnSi into many microscopic units, each of which acts independently of all others. Each unit can either be in the SkL phase or the conical phase, and the fields at which a unit switches from one phase to the other is given by $H_c + H_a$ ($H_c - H_a$) for the increasing (decreasing) field sweep. One way to visualize a hysteretic system is to plot the distribution of the units as a function of H_a and H_c. The 2D space of (H_a, H_c) is known as the "Preisach plane." The usefulness of this approach to visualizing the hysteresis becomes apparent when considering when field is increased from zero. Assuming that all units start in the conical phase, for any given field H there is a line $H - H_a$ that can be drawn through the distribution separating the units in the SkL phase from those in the conical. As we increase H, this line moves upward, and units that move across the line transition into the SkL phase (Fig. B.1). If we reach a maximum field H_{max} and then begin decreasing the applied field, a new line $H + H_a$ begins moving downwards, transition units back into the conical phase. This line can obviously only transition units that are currently in the SkL phase, so the line dividing the two phases becomes the intersection of $H + H_a$ with $H_{max} - H_a$, which we shall call $z(H_a)$ (Fig. B.2). From here, it is easy to imagine how a complex field history, including many direction changes could result in a very complex, sawtooth form for $z(H_a)$. Making predictions about the SANS response of the system therefore becomes a matter of determining

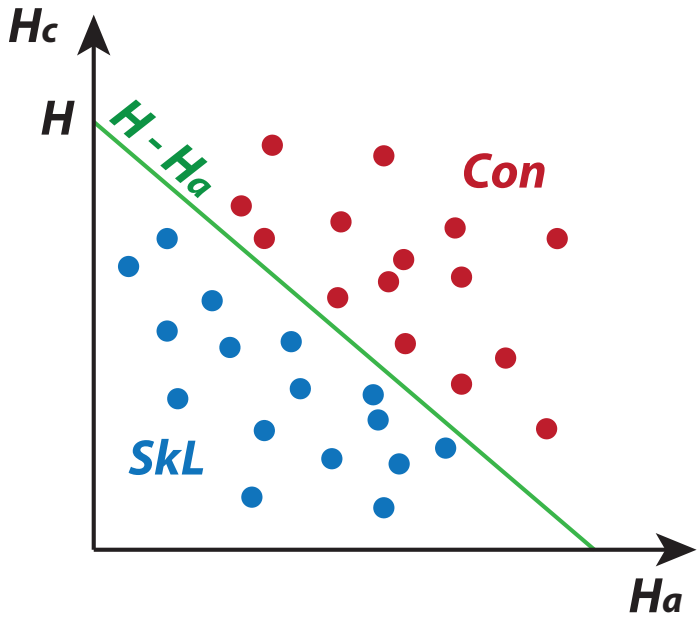

Figure B.1. Distribution of Preisach units within the Preisach plane. The line $H - H_a$ separates the SkL units from the conical units for increasing field sweeps.

the fraction of the Preisach distribution falls on either side of $z(H_a)$.

For our analysis, we assumed that the shape of the Preisach distribution could be estimated as a two dimensional Gaussian distribution, with a maximum located at $(\bar{H}_a, \bar{H}_c)$ and width given by the standard deviation in both directions σ_a and σ_c.

In the simple case of the major loops, the distribution starts entirely on one side of $z(H_a)$, and progresses entirely to the other side. To determine the fraction on either side during the intermediate fields, the 2D Gaussian must be integrated up to $z(H_a)$. However, since our SANS major hysteresis loops cross two phase transitions, the system has to be treated as two competing hysteresis loops, i.e. for any intermediate field, the fraction of the sample in the SkL phase is the fraction of the sample that has entered the SkL phase by crossing H_{c1} *minus* that which has left the SkL phase by crossing H_{c2}. This means that all eight Preisach parameters ($\bar{H}_{a1}$, $\bar{H}_{c1}$, σ_{a1}, σ_{c1}, $\bar{H}_{a2}$, $\bar{H}_{c2}$, σ_{a2}, σ_{c2}) must be fit simultaneously to our data. Additionally, because of the

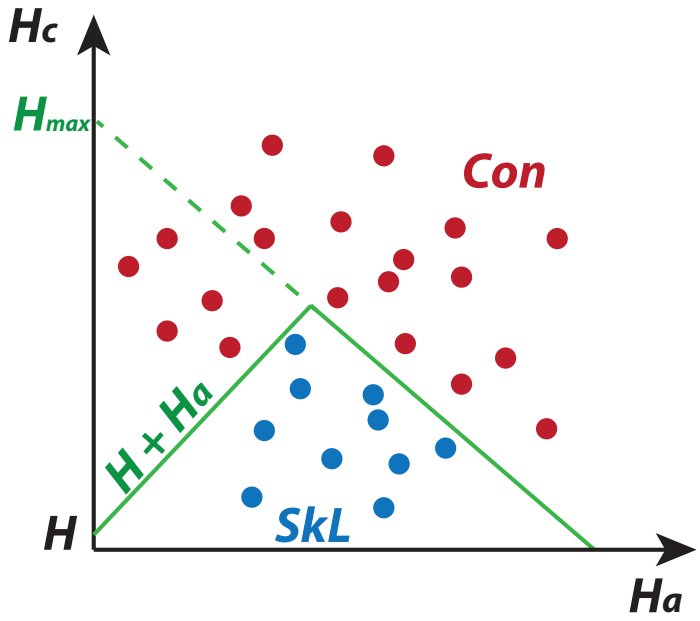

Figure B.2. The effect of changing the field sweep direction from increasing to decreasing at a maximum field H_{max}. The line of separation $z(H_a)$ becomes more sawtooth-ed and complicated with each direction change.

two transitions, we cannot be sure from our SANS signal that the sample ever reaches 100% saturation into the SkL phase before reverting back to the conical phase. This means that a ninth, normalization parameter (called N) must also be added to our calculation.

Combining all of this, we find that we have to fit a nine parameter function to our data, and for every possible solution in this nine dimensional space our algorithm will have to numerically integrate a 2D Gaussian. This is obviously a non-trivial computational challenge. Fortunately, there are a few tricks that I came up with to make the computation converge to a solution more quickly and more consistently.

First, it was necessary to feed the fitting algorithm as much data as possible. This meant giving the algorithm both the increasing and decreasing field sweeps at the same time. I originally experimented with making the data three dimensional as (Field, Direction, SANS signal), however this dramatically slowed the fitting. Even-

tually, I figured out a sort of two-and-a-half dimensional approach, where I switched the sign of the field for all points in the loop where magnetic field was decreasing, and split the prediction function accordingly. This helped quite a bit.

The next trick I found was how to give the least squares optimization good starting guesses for the Preisach parameters. I always started by assuming that the normalization was correct on the data ($N = 1$). Therefore, the H_c's can be extracted from the points in the loop where the SANS intensity was at half maximum. Additionally, the H_a's can be extracted from the field separation of the two sweeps at these points. Both these approximations tend to be good starting points for the fits.

The final trick that came in handy was the accidental discovery that $\sigma_{a1} = \sigma_{a2} = 0$. I was having a very hard time getting my fits to converge consistently, and by running the least squares fit with many randomized starting points I discovered that the $\bar{H}_a$'s were strongly correlated with the corresponding σ_a's. As it turns out, I believe it is extremely difficult to separate these parameters without extensive minor loops. I noticed however that if I plotted the fits in the ($\bar{H}_a$, σ_a) plane, they produced a sort of quarter circle (see Fig. B.3). I decided it might be worth trying the intercepts of this semicircle. It became clear that the $\bar{H}_a = 0$ intercept made no sense physically as this would eliminate all hysteretic behavior. However, by fixing $\sigma_a = 0$ (and therefore going to a Gaussian-Dirac Delta distribution), the fits converged beautifully and rapidly. This has the added bonus of supporting the topological origin of $\bar{H}_a$. The final code used for major loop fits is **DoublePreisach2_5DLsqDirac.m**[1].

The minor loops were fit with a similar algorithm with a few modifications. Firstly, since the sample was field cooled before the loop, its impossible to know the exact starting shape of $z(H_a)$. I decided to assume the simplest shape, which is a straight horizontal line that bisects the Preisach distribution, i.e. $z(H_a) = \bar{H}_c$. Additionally,

[1]This file and all the other functions it calls is located in the 'Eskildsen Group/ SANS/ MnSi SkL Hysteresis Stuff/ grasp 3_20 allan copy' folder on Box

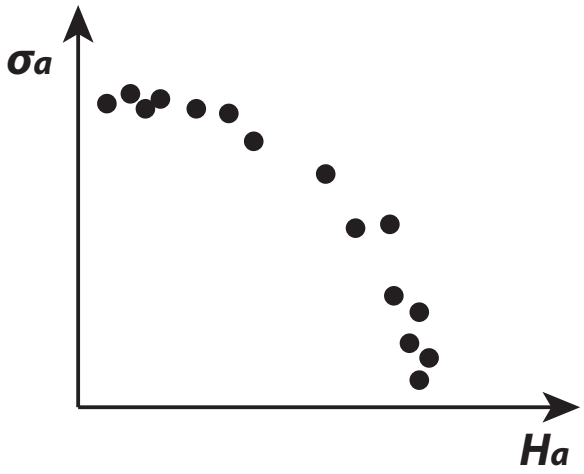

Figure B.3. Cartoon of the distribution of the fitted $\bar{H}_a$ and σ_a when the Preisach fitting algorithm is run many times with randomized starting values. The two parameters are highly coupled.

since I knew the high field transition minor loops would not be very sensitive to the Preisach parameters of the lower transition, I restricted $\bar{H}_{a1}$, $\bar{H}_{c1}$, σ_{a1}, and σ_{c1} to all remain very close to the values determined from the major loops. Besides these changes, the fitting process was the same. The function used to perform the final minor loop fits is **DoublePreisach2_5DMinorLsqDirac.m**[1].

APPENDIX C

DEMAGNETIZATION ESTIMATION

In order to determine the how much of the phase transition broadening observed in Chapter 3 could be explained by demagnetization effects, a script was written to estimate the true, local magnetic field (B) as a function of applied field ($\mu_0 H_0$) for different samples of MnSi. Specifically, we wished to determine:

$$\vec{B} = \mu_0(\vec{M} + \vec{H}) \tag{C.1}$$

where

$$\vec{H} = \vec{H_0} - \hat{N}\vec{M_0} \tag{C.2}$$

Here, $\hat{N}$ is defined as the "demagnetization tensor". Therefore, the true field B within the sample is

$$\vec{B} = \mu_0\vec{H_0} + \mu_0(1 - \hat{N})\vec{M_0} \tag{C.3}$$

Since we are only interested in a rough estimate of the scale of the demagnetization across the sample, we now make several approximations. Firstly, we assume that we only care about how the demagnetization affects the field magnitude in the external applied field direction, as this component should dictate where we are in the phase diagram. Setting the applied field along z, we are therefore interested in finding

$$B_z = \mu_0 H_0 + \mu_0(1 - \hat{N})\vec{M_0} \tag{C.4}$$

Next, we assume that the magnetization of the sample is negligible in all directions except for z. Therefore,

$$B_z = \mu_0 H_0 + \mu_0 (1 - N_{zz}) M_{0,z} \tag{C.5}$$

$M_{0,z}$ can be approximated from measured magnetization curves of MnSi, such as that of Bauer and Pfleiderer [16]. Finally, we can calculate N_{zz} using the first-order approximations derived by Joseph and Schlömann [64].

Two crystals of MnSi were considered in particular: the sample used at ILL, which is roughly cylindrical in shape, and the sample used at PSI and ANSTO, which is roughly a rectangular prism. MATLAB code[1] was used to evaluate the relevant expressions of Joseph and Schlömann [64] (cylinder for ILL and rectangular for PSI/ANSTO) over a discrete set of points within the sample volume. These points were selected such that they would be spaced equal-volumetrically from each other. An example of the calculated local field is shown in Fig. C.1. Finally, to estimate how much this demagnetization would broaden the observed phase transitions, the distribution of field throughout the sample can be plotted as a histogram. This is shown for the PSI crystal in Fig. C.2. This distribution of fields is fit decently well by a Gaussian as shown in Fig. C.3. From the width of this distribution, it seems that a large portion (although not all) of the observed transition broadening σ_c can be explained by demagnetization effects.

[1] **cylfield3D.m** and **prismfield3D.m**, located in the 'Eskildsen Group/ SANS/ MnSi SkL Hysteresis Stuff/ grasp 3_20 allan copy' folder on Box

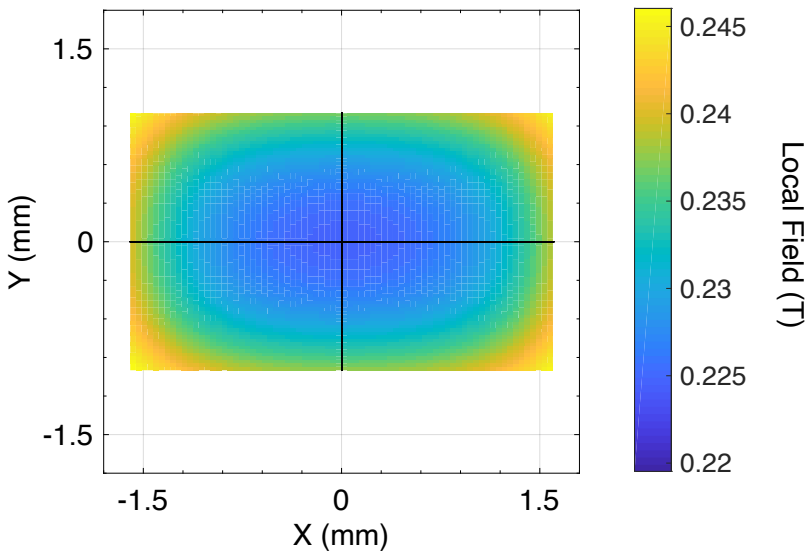

Figure C.1. Magnetic field as a function of position in the central plane of the rectangular PSI/ANSTO crystal. Applied field of $\mu_0 H = 0.2$ T points out of the page along the z axis.

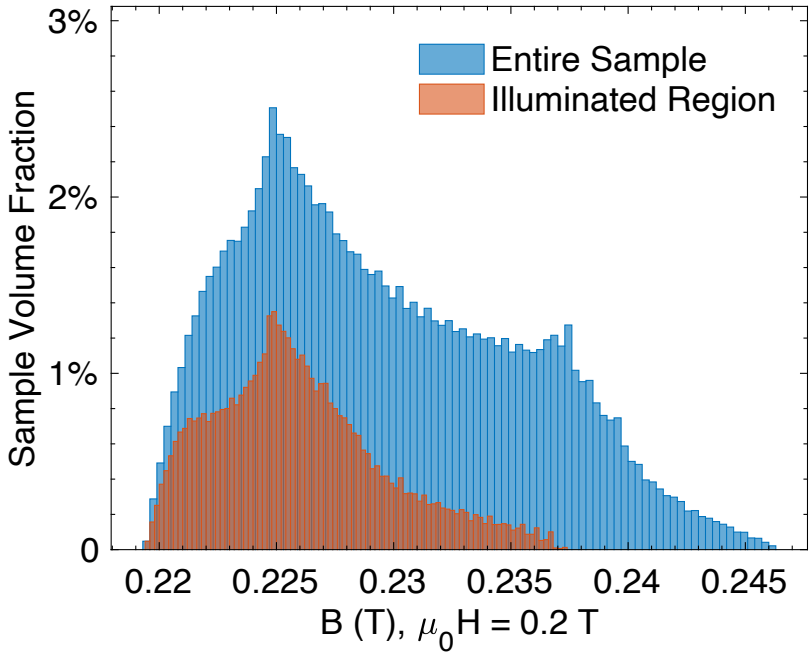

Figure C.2. Distribution of local magnetic field for the entire PSI/ANSTO crystal (blue), as well as the portion of the sample that was illuminated with a 1 mm diameter aperture for SANS (orange). Applied field is $\mu_0 H = 0.2$ T.

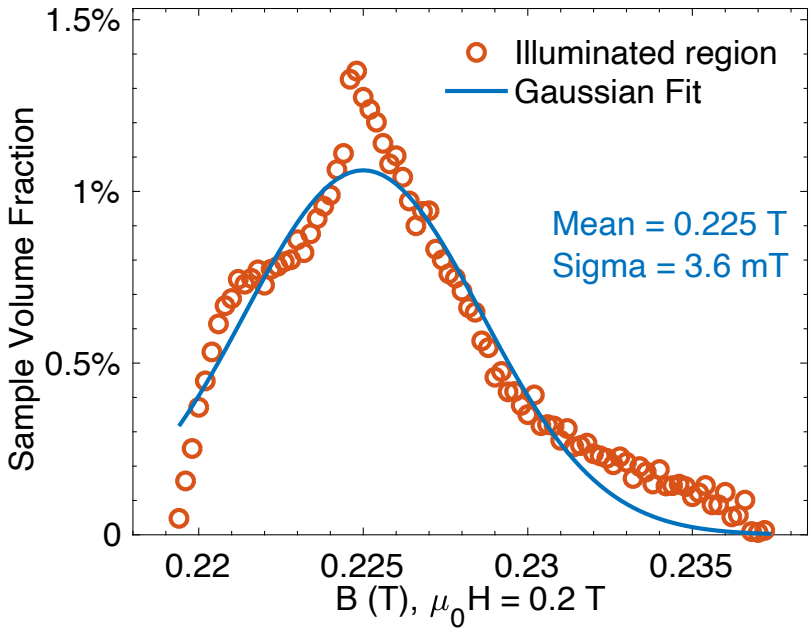

Figure C.3. Gaussian distribution fit to the local magnetic field in the illuminated sample at PSI/ANSTO. Applied field is $\mu_0 H = 0.2$ T.

BIBLIOGRAPHY

1. Neutron Velocity Selector. https://www3.sii.co.jp/jp/segg/files/2013/03/file_PRODUCT_MASTER_1381_GRAPHIC02.pdf. Accessed: 2020-2-12.

2. BASIC QUALITY SAPPHIRE WINDOWS. https://melleroptics.com/product-category/basic-quality-sapphire-windows/. Accessed: 2020-12-31.

3. See Supplemental Material at https://www.dropbox.com/sh/38yc4vjozvmws4m/AACTkUjHcRmphUtBeilQDXV2a?dl=0 for the animation of the transition between Con and SkL states presented in Fig. 5(d).

4. P. M. Abanador, A. R. C. Villagracia, N. B. A. Jr., and M. Y. David. First principle investigation of atomic hydrogen adsorption on Pd-doped MgB_2. *Phillipine Sci. Lett.*, 6(2), 2013.

5. A. Abrikosov. The magnetic properties of superconducting alloys. *J. Phys. Chem. Solids*, 2(3):199–208, 1957.

6. Y. Aharonov and D. Bohm. Significance of Electromagnetic Potentials in the Quantum Theory. *Phys. Rev.*, 115(3):485–491, 1959.

7. P. W. Anderson. New Approach to the Theory of Superexchange Interactions. *Phys. Rev.*, 115(1):2–13, 1959.

8. J. F. Annett. *Superconductivity, Superfluids, and Condensates*. Oxford master series in condensed matter physics. Oxford University Press, Oxford ; New York, 2004. ISBN 0198507550.

9. N. W. Ashcroft. *Solid State Physics*. Holt, Rinehart and Winston, New York, 1976. ISBN 0030839939.

10. K. E. Avers, W. J. Gannon, S. J. Kuhn, W. P. Halperin, J. A. Sauls, L. DeBeer-Schmitt, C. D. Dewhurst, J. Gavilano, G. Nagy, U. Gasser, and M. R. Eskildsen. Broken time reversal symmetry in the topological superconductor UPt_3. *Nat. Phys.*, 16:531–535, 2020.

11. P. Bak and M. H. Jensen. Theory of helical magnetic structures and phase transitions in MnSi and FeGe. *J. Phys. C*, 13(31):L881–L885, 1980.

12. L. Bannenberg, F. Qian, R. Dalgliesh, N. Martin, G. Chaboussant, M. Schmidt, D. Schlagel, T. Lograsso, H. Wilhelm, and C. Pappas. Reorientations, relaxations, metastabilities, and multidomains of skyrmion lattices. *Phys. Rev. B*, 96(18), 2017.

13. L. J. Bannenberg, F. Qian, R. M. Dalgliesh, N. Martin, G. Chaboussant, M. Schmidt, D. L. Schlagel, T. A. Lograsso, H. Wilhelm, and C. Pappas. Reorientations, relaxations, metastabilities and domains of skyrmion lattices. *Phys. Rev. B*, 96:184416, 2017.

14. L. J. Bannenberg, R. Sadykov, R. M. Dalgliesh, C. Goodway, D. L. Schlagel, T. A. Lograsso, P. Falus, E. Lelièvre-Berna, A. O. Leonov, and C. Pappas. Skyrmions and spirals in MnSi under hydrostatic pressure. *Phys. Rev. B*, 100 (5):054447, 2019.

15. J. Bardeen, L. N. Cooper, and J. R. Schrieffer. Microscopic Theory of Superconductivity. *Phys. Rev.*, 106(1):162–164, 1957.

16. A. Bauer and C. Pfleiderer. Magnetic phase diagram of MnSi inferred from magnetization and ac susceptibility. *Phys. Rev. B*, 85:214418, 2012.

17. G. Bertotti. *Hysteresis in Magnetism: for Physicists, Materials Scientists, and Engineers*. Academic Press, 1998. ISBN 978-0-12-093270-2.

18. P. F. Bessarab, V. M. Uzdin, and H. Jónsson. Method for finding mechanism and activation energy of magnetic transitions, applied to skyrmion and antivortex annihilation. *Comput. Phys. Commun.*, 196:335–347, 2015.

19. M. T. Birch, R. Takagi, S. Seki, M. N. Wilson, F. Kagawa, A. Štefančič, G. Balakrishnan, R. Fan, P. Steadman, C. J. Ottley, and et al. Increased lifetime of metastable skyrmions by controlled doping. *Phys. Rev. B*, 100(1):014425, 2019.

20. A. Bogdanov and A. Hubert. Thermodynamically stable magnetic vortex states in magnetic crystals. *J. Magn. Magn. Mater.*, 138(3):255–269, 1994.

21. P. W. Bridgman. Certain Physical Properties of Single Crystals of Tungsten, Antimony, Bismuth, Tellurium, Cadmium, Zinc, and Tin. *Proc. Am. Acad. Arts Sci.*, 60(6):305, 1925.

22. P. Bruno, V. K. Dugaev, and M. Taillefumier. Topological Hall Effect and Berry Phase in Magnetic Nanostructures. *Phys. Rev. Lett.*, 93(9):096806, 2004.

23. F. Büttner, I. Lemesh, and G. S. D. Beach. Theory of isolated magnetic skyrmions: From fundamentals to room temperature applications. *Sci. Rep.*, 8 (1):4464, 2018.

24. L. J. Campbell, M. M. Doria, and V. G. Kogan. *Phys. Rev. B*, 38:2439–2443, 1988.

25. A. Chacon, A. Bauer, T. Adams, F. Rucker, G. Brandl, R. Georgii, M. Garst, and C. Pfleiderer. Uniaxial Pressure Dependence of Magnetic Order in MnSi. *Phys. Rev. Lett.*, 115(26):267202, 2015.

26. H. J. Choi, D. Roundy, H. Sun, M. L. Cohen, and S. G. Louie. The origin of the anomalous superconducting properties of MgB_2. *Nature*, 418(6899):758–760, 2002.

27. D. K. Christen, H. R. Kerchner, S. T. Sekula, and Y. K. Chang. Flux-line lattice anisotropy in V_3Si: observation and interpretation. *Physica B*, 135:369–373, 1985.

28. O. M. Corbino. Azioni Elettromagnetiche Doyute Agli Ioni dei Metalli Deviati Dalla Traiettoria Normale per Effetto di un Campo. *Il Nuovo Cimento (1911-1923)*, 1(1):397–420, 1911.

29. R. Cubitt, M. R. Eskildsen, C. D. Dewhurst, J. Jun, S. M. Kazakov, and J. Karpinski. Effects of two-band superconductivity on the flux-line lattice in magnesium diboride. *Phys. Rev. Lett.*, 91:047002, 2003.

30. P. Das, C. Rastovski, T. O'Brien, K. Schlesinger, C. Dewhurst, L. DeBeer-Schmitt, N. Zhigadlo, J. Karpinski, and M. Eskildsen. Observation of Well-Ordered Metastable Vortex Lattice Phases in Superconducting MgB_2 Using Small-Angle Neutron Scattering. *Phys. Rev. Lett.*, 108(16):167001, 2012.

31. M. Date, K. Okuda, and K. Kadowaki. Electron Spin Resonance in the Itinerant-Electron Helical Magnet MnSi. *J. Phys. Soc. Jpn.*, 42(5):1555–1561, 1977.

32. C. D. Dewhurst. private communication.

33. I. Dzyaloshinsky. A THERMODYNAMIC THEORY OF "WEAK" FERROMAGNETISM OF ANTIFERROMAGNETICS. *J. Phys. Chem. Solids*, 4(4): 241–255, 1958.

34. M. Eskildsen, M. Kugler, G. Levy, S. Tanaka, J. Jun, S. Kazakov, J. Karpinski, and Fischer. Scanning tunneling spectroscopy on single crystal MgB_2. *Physica C: Supercond.*, 385(1–2):169–176, 2003.

35. M. R. Eskildsen. Vortex lattices in type-II superconductors studied by small-angle neutron scattering. *Front. Phys.*, 6(4):398–409, 2011.

36. M. R. Eskildsen, K. Harada, P. L. Gammel, A. B. Abrahamsen, N. H. Andersen, G. Ernst, A. P. Ramirez, D. J. Bishop, K. Mortensen, D. G. Naugle, K. D. D. Rathnayaka, and P. C. Canfield. Intertwined symmetry of the magnetic modulation and the flux-line lattice in the superconducting state of $TmNi_2B_2C$. *Nature*, 393:242–245, 1998.

37. M. R. Eskildsen, N. Jenkins, G. Levy, M. Kugler, Fischer, J. Jun, S. M. Kazakov, and J. Karpinski. Vortex imaging in magnesium diboride with Hc. *Phys. Rev. B*, 68(10):100508, 2003.

38. M. R. Eskildsen, C. Dewhurst, D. Honecker, A. Leishman, and J. White. Institut Laue-Langevin (ILL) doi: 10.5291/ILL-DATA.5-42-477, 2018.

39. K. Everschor-Sitte and M. Sitte. File:2skyrmions.PNG. `https://commons.wikimedia.org/wiki/File:2skyrmions.PNG`.

40. A. Fert, V. Cros, and J. Sampaio. Skyrmions on the track. 8:152–156, 2013.

41. A. Fert, N. Reyren, and V. Cros. Magnetic skyrmions: advances in physics and potential applications. *Nat. Rev. Mater.*, 2:17031, 2017.

42. J. Finney. Neutrons for the future. *Phys. World*, Dec 1997.

43. D. M. Fobes, Y. Luo, N. Leon-Brito, E. D. Bauer, V. R. Fanelli, M. A. Taylor, L. M. DeBeer-Schmitt, and M. Janoschek. Versatile strain-tuning of modulated long-period magnetic structures. *Appl. Phys. Lett.*, 110:192409, 2017.

44. P. L. Gammel, D. A. Huse, R. N. Kleiman, B. Batlogg, C. S. Oglesby, E. Bucher, D. J. Bishop, T. E. Mason, and K. Mortensen. Small Angle Neutron Scattering Study of the Magnetic Flux-Line Lattice in Single Crystal $2H$-$NbSe_2$. *Phys. Rev. Lett.*, 72:278–281, 1994.

45. W. J. Gannon, W. P. Halperin, C. Rastovski, K. J. Schlesinger, J. Hlevyack, M. R. Eskildsen, A. B. Vorontsov, J. Gavilano, U. Gasser, and G. Nagy. Nodal gap structure and order parameter symmetry of the unconventional superconductor UPt_3. *New J. Phys.*, 17:023041, 2015.

46. C. J. Glinka, J. G. Barker, B. Hammouda, S. Krueger, J. J. Moyer, and W. J. Orts. The 30 m Small-Angle Neutron Scattering Instruments at the National Institute of Standards and Technology. *J. Appl. Cryst.*, 31:430–435, 1998.

47. S. V. Grigoriev, S. V. Maleyev, A. I. Okorokov, Y. O. Chetverikov, R. Georgii, P. Böni, D. Lamago, H. Eckerlebe, and K. Pranzas. Critical fluctuations in MnSi near T_C: A polarized neutron scattering study. *Phys. Rev. B*, 72:134420, 2005.

48. S. V. Grigoriev, S. V. Maleyev, A. I. Okorokov, Y. O. Chetverikov, P. Böni, R. Georgii, D. Lamago, H. Eckerlebe, and K. Pranzas. Magnetic structure of MnSi under an applied field probed by polarized small-angle neutron scattering. *Phys. Rev. B*, 74:214414, 2006.

49. S. V. Grigoriev, D. Chernyshov, V. A. Dyadkin, V. Dmitriev, E. V. Moskvin, D. Lamago, T. Wolf, D. Menzel, J. Schoenes, S. V. Maleyev, and et al. Interplay between crystalline chirality and magnetic structure in $Mn_{1x}Fe_xSi$. *Phys. Rev. B*, 81(1):012408, 2010.

50. P. Harris. Neutron and X-Ray Diffraction from Modulated Structures. *Risø National Laboratory*, 1994.

51. B. Heil, A. Rosch, and J. Masell. Universality of annihilation barriers of large magnetic skyrmions in chiral and frustrated magnets. *Phys. Rev. B*, 100:134424, 2019.

52. S. Heinze, K. v. Bergmann, M. Menzel, J. Brede, A. Kubetzka, R. Wiesendanger, G. Bihlmayer, and S. Blügel. Spontaneous atomic-scale magnetic skyrmion lattice in two dimensions. *Nat. Phys.*, 7(9):713–718, 2011.

53. W. T. Heller, M. Cuneo, L. Debeer-Schmitt, C. Do, L. He, L. Heroux, K. Littrell, S. V. Pingali, S. Qian, C. Stanley, V. S. Urban, B. Wu, and W. Bras. The suite of small-angle neutron scattering instruments at Oak Ridge National Laboratory. *J. Appl. Crystallogr.*, 51:242–248, 2018.

54. G. Henkelman and H. Jónsson. Improved tangent estimate in the nudged elastic band method for finding minimum energy paths and saddle points. *J. Chem. Phys.*, 113:9978–9985, 2000.

55. Y. Ishikawa and M. Arai. Magnetic Phase Diagram of MnSi near Critical Temperature Studied by Neutron Small Angle Scattering. 53:2726–2733, 1984.

56. Y. Ishikawa, G. Shirane, J. A. Tarvin, and M. Kohgi. Magnetic excitations in the weak itinerant ferromagnet MnSi. *Phys. Rev. B*, 16(11):4956–4970, 1977.

57. J. Iwasaki, M. Mochizuki, and N. Nagaosa. Current-induced skyrmion dynamics in constricted geometries. *Nat. Nanotechnol.*, 8:742, 2013.

58. J. Iwasaki, M. Mochizuki, and N. Nagaosa. Universal current-velocity relation of skyrmion motion in chiral magnets. *Nat. Commun.*, 4:1463, 2013.

59. M. Janoschek, M. Garst, A. Bauer, P. Krautscheid, R. Georgii, P. Böni, and C. Pfleiderer. Fluctuation-induced first-order phase transition in Dzyaloshinskii-Moriya helimagnets. *Phys. Rev. B*, 87:134407, 2013.

60. T. Jeong and W. E. Pickett. Implications of the B20 crystal structure for the magnetoelectronic structure of MnSi. *Phys. Rev. B*, 70:075114, 2004.

61. W. Jiang, X. Zhang, G. Yu, W. Zhang, X. Wang, M. B. Jungfleisch, J. E. Pearson, X. Cheng, O. Heinonen, K. L. Wang, and et al. Direct observation of the skyrmion Hall effect. *Nat. Phys.*, 13(2):162–169, 2017.

62. M. E. Jones and R. E. Marsh. The Preparation and Structure of Magnesium Boride, MgB_2. *J. Am. Chem. Soc.*, 76(5):1434–1436, 1954.

63. F. Jonietz, S. Mühlbauer, C. Pfleiderer, A. Neubauer, W. Münzer, A. Bauer, T. Adams, R. Georgii, P. Böni, R. A. Duine, and et al. Spin Transfer Torques in MnSi at Ultralow Current Densities. *Science*, 330(6011), 2010.

64. R. I. Joseph and E. Schlömann. Demagnetizing Field in Nonellipsoidal Bodies. *J. Appl. Phys.*, 36(5):1579–1593, 1965.

65. J. Karpinski, M. Angst, J. Jun, S. M. Kazakov, R. Puzniak, A. Wisniewski, J. Roos, H. Keller, A. Perucchi, L. Degiorgi, M. R. Eskildsen, P. Bordet, L. Vinnikov, and A. Mironov. MgB_2 single crystals: high pressure growth and physical properties. *Supercond. Sci. Technol.*, 16:221–230, 2003.

66. K. Karube, J. S. White, N. Reynolds, J. L. Gavilano, H. Oike, A. Kikkawa, F. Kagawa, Y. Tokunaga, H. M. Rønnow, Y. Tokura, and et al. Robust metastable skyrmions and their triangular–square lattice structural transition in a high-temperature chiral magnet. *Nat. Mater.*, 15(12):1237–1242, 2016.

67. K. Karube, J. S. White, D. Morikawa, M. Bartkowiak, A. Kikkawa, Y. Tokunaga, T. Arima, H. M. Rønnow, Y. Tokura, and Y. Taguchi. Skyrmion formation in a bulk chiral magnet at zero magnetic field and above room temperature. *Phys. Rev. Mater.*, 1:074405, 2017.

68. J. Kindervater, I. Stasinopoulos, A. Bauer, F. X. Haslbeck, F. Rucker, A. Chacon, S. Mühlbauer, C. Franz, M. Garst, D. Grundler, and C. Pfleiderer. Weak Crystallization of Fluctuating Skyrmion Textures in MnSi. *Phys. Rev. X*, 9: 041059, 2019.

69. C. Kittel. *Introduction to Solid State Physics*. Wiley, Hoboken, NJ, 8th ed. edition, 2005. ISBN 047141526X.

70. W. H. Kleiner, L. M. Roth, and S. H. Autler. Bulk Solution of Ginzburg-Landau Equations for Type II Superconductors: Upper Critical Field Region. *Phys. Rev.*, 133(5A):A1226–A1227, 1964.

71. V. G. Kogan. London approach to anisotropic type-II superconductors. *Phys. Rev. B*, 24:1572–1575, 1981.

72. V. G. Kogan, M. Bullock, B. Harmon, P. Miranovic, L. Dobrosavlevic-Grujic, P. L. Gammel, and D. J. Bishop. Vortex lattice transitions in borocarbides. *Phys. Rev. B*, 55:R8693–R8696, 1997.

73. S. J. Kuhn. Exploring highly anisotropic vortex lattices of unconventional superconductors using small angle neutron scattering, 2017.

74. S. J. Kuhn, W. Morgenlander, E. R. Louden, C. Rastovski, W. J. Gannon, H. Takatsu, D. C. Peets, Y. Maeno, C. D. Dewhurst, J. Gavilano, and M. R. Eskildsen. Anisotropy and multiband superconductivity in Sr_2RuO_4 determined by small-angle neutron scattering studies of the vortex lattice. *Phys. Rev. B*, 96:174507, 2017.

75. S. Kusaka, K. Yamamoto, T. Komatsubara, and Y. Ishikawa. Ultrasonic study of magnetic phase diagram of MnSi. *Solid State Commun.*, 20(9):925–927, 1976.

76. L. Landau. *Collected Papers of L.D. Landau*, page 546–568. 1965.

77. M. Laver, E. M. Forgan, S. P. Brown, D. Charalambous, D. Fort, C. Bowell, S. Ramos, R. J. Lycett, D. K. Christen, J. Kohlbrecher, C. D. Dewhurst, and R. Cubitt. Spontaneous Symmetry-Breaking Vortex Lattice Transitions in Pure Niobium. *Phys. Rev. Lett.*, 96(16):167002, 2006.

78. M. Laver, C. J. Bowell, E. M. Forgan, A. B. Abrahamsen, D. Fort, C. D. Dewhurst, S. Mühlbauer, D. K. Christen, J. Kohlbrecher, R. Cubitt, and S. Ramos. Structure and degeneracy of vortex lattice domains in pure superconducting niobium: A small-angle neutron scattering study. *Phys. Rev. B*, 79:014518, 2009.

79. A. W. D. Leishman, R. M. Menezes, G. Longbons, E. D. Bauer, M. Janoschek, D. Honecker, L. DeBeer-Schmitt, J. S. White, A. Sokolova, M. V. Milošević, and et al. Topological energy barrier for skyrmion lattice formation in MnSi. *Phys. Rev. B*, 102(10):104416, 2020.

80. A. W. D. Leishman, A. Sokolova, M. Bleuel, N. D. Zhigadlo, and M. R. Eskildsen. Field-angle dependent vortex lattice phase diagram in MgB_2. *arXiv*, 2021.

81. S. J. Levett, C. D. Dewhurst, and D. M. Paul. Vortex-lattice transitions in YNi_2B_2C: Nature of the 45-degree reorientation. *Phys. Rev. B*, 66(1):014515, 2002.

82. Y.-Y. Li. Domain Walls in Antiferromagnets and the Weak Ferromagnetism of FeO. *Phys. Rev.*, 101(5):1450–1454, 1956.

83. K. Litzius, I. Lemesh, B. Krüger, P. Bassirian, L. Caretta, K. Richter, F. Büttner, K. Sato, O. A. Tretiakov, J. Förster, and et al. Skyrmion Hall effect revealed by direct time-resolved X-ray microscopy. *Nat. Phys.*, 13(2): 170–175, 2017.

84. I. S. Lobanov, H. Jónsson, and V. M. Uzdin. Mechanism and activation energy of magnetic skyrmion annihilation obtained from minimum energy path calculations. *Phys. Rev. B*, 94:174418, 2016.

85. G. G. Lonzarich and L. Taillefer. Effect of spin fluctuations on the magnetic equation of state of ferromagnetic or nearly ferromagnetic metals. *J. Phys. C*, 18:4339–4371, 1985.

86. E. R. Louden, A. W. D. Leishman, C. Rastovski, S. J. Kuhn, L. DeBeer-Schmitt, C. D. Dewhurst, N. D. Zhigadlo, and M. R. Eskildsen. Structural studies of metastable and equilibrium vortex lattice domains in MgB_2. *New J. Phys.*, 21 (6):063003, 2019.

87. E. R. Louden, C. Rastovski, L. DeBeer-Schmitt, C. D. Dewhurst, N. D. Zhigadlo, and M. R. Eskildsen. Non-equilibrium structural phase transitions of the vortex lattice in MgB_2. *Phys. Rev. B*, 99:144515, 2019.

88. E. R. Louden, C. Rastovski, S. J. Kuhn, A. W. D. Leishman, L. DeBeer-Schmitt, C. D. Dewhurst, N. D. Zhigadlo, and M. R. Eskildsen. Structural transition kinetics and activated behavior in the superconducting vortex lattice. *Phys. Rev. B*, 99:060502(R), 2019.

89. R. P. Louis Néel. Etude thermomagnétique d'un monocristal de Fe_2O_3-alpha. *C. R. Acad. Sci.*, 234:2172–2174, 1952.

90. Y. Luo, S.-Z. Lin, M. Leroux, N. Wakeham, D. M. Fobes, E. D. Bauer, J. B. Betts, J. D. Thompson, A. Migliori, M. Janoschek, and B. Maiorov. Skyrmion creep at ultra-low current densities. Private communication.

91. Y. Luo, S.-Z. Lin, D. M. Fobes, Z. Liu, E. D. Bauer, J. B. Betts, A. Migliori, J. D. Thompson, M. Janoschek, and B. Maiorov. Anisotropic magneto-crystalline coupling of the skyrmion lattice in MnSi. *Phys. Rev. B*, 97:104423, 2018.

92. L. Lyard, P. Samuely, P. Szabo, T. Klein, C. Marcenat, L. Paulius, K. H. P. Kim, C. U. Jung, H.-S. Lee, B. Kang, and et al. Anisotropy of the upper critical field and critical current in single crystal MgB_2. *Phys. Rev. B*, 66(18):180502, 2002.

93. D. López, W. Kwok, H. Safar, R. Olsson, A. Petrean, L. Paulius, and G. Crabtree. Spatially resolved dynamic correlation in the vortex state of high temperature superconductors. *Physical Review Letters*, 82(6):1277–1280, 1999. ISSN 0031-9007. doi: 10.1103/physrevlett.82.1277.

94. K. Makino, J. D. Reim, D. Higashi, D. Okuyama, T. J. Sato, Y. Nambu, E. P. Gilbert, N. Booth, S. Seki, and Y. Tokura. Thermal stability and irreversibility of skyrmion-lattice phases in Cu_2OSeO_3. *Phys. Rev. B*, 95:134412, 2017.

95. S. V. Maleyev. Cubic magnets with Dzyaloshinskii-Moriya interaction at low temperature. *Phys. Rev. B*, 73:174402, 2006.

96. W. Meissner and R. Ochsenfeld. Ein neuer Effekt bei Eintritt der Supraleitfähigkeit. *Sci. Nat.*, 21(44):787–788, 1933.

97. P. Milde, D. Köhler, J. Seidel, L. M. Eng, A. Bauer, A. Chacon, J. Kindervater, S. Mühlbauer, C. Pfleiderer, S. Buhrandt, and et al. Unwinding of a Skyrmion Lattice by Magnetic Monopoles. *Science*, 340(6136):1076–1080, 2013.

98. T. Moriya. Anisotropic Superexchange Interaction and Weak Ferromagnetism. *Phys. Rev.*, 120(1):91–98, 1960.

99. S. Mühlbauer, C. Pfleiderer, P. Böni, M. Laver, E. M. Forgan, D. Fort, U. Keiderling, and G. Behr. Morphology of the Superconducting Vortex Lattice in Ultrapure Niobium. *Phys. Rev. Lett.*, 102:136408, 2009.

100. S. Mühlbauer, D. Honecker, È. A. Pèrigo, F. Bergner, S. Disch, A. Heinemann, S. Erokhin, D. Berkov, C. Leighton, M. R. Eskildsen, and A. Michels. Magnetic small-angle neutron scattering. *Rev. Mod. Phys.*, 91:015004, 2019.

101. G. P. Müller, M. Hoffmann, C. Dißelkamp, D. Schürhoff, S. Mavros, M. Sallermann, N. S. Kiselev, H. Jónsson, and S. Blügel. Spirit: Multifunctional framework for atomistic spin simulations. *Phys. Rev. B*, 99:224414, 2019.

102. S. Mühlbauer, B. Binz, F. Jonietz, C. Pfleiderer, A. Rosch, A. Neubauer, R. Georgii, and P. Böni. Skyrmion Lattice in a Chiral Magnet. *Science*, 323 (5916):915–919, 2009.

103. J. Nagamatsu, N. Nakagawa, T. Muranaka, Y. Zenitani, and J. Akimitsu. Superconductivity at 39 K in magnesium diboride. *Nature*, 410(6824):63–64, 2001.

104. T. Nakajima, H. Oike, A. Kikkawa, E. P. Gilbert, N. Booth, K. Kakurai, Y. Taguchi, Y. Tokura, F. Kagawa, and T.-h. Arima. Skyrmion lattice structural transition in MnSi. *Sci. Adv.*, 3(6):e1602562, 2017.

105. Y. Nii, T. Nakajima, A. Kikkawa, Y. Yamasaki, K. Ohishi, J. Suzuki, Y. Taguchi, T. Arima, Y. Tokura, and Y. Iwasa. Uniaxial stress control of skyrmion phase. *Nat. Commun.*, 6(1):8539, 2015.

106. H. Oike, A. Kikkawa, N. Kanazawa, Y. Taguchi, M. Kawasaki, Y. Tokura, and F. Kagawa. Interplay between topological and thermodynamic stability in a metastable magnetic skyrmion lattice. *Nat. Phys.*, 12:62–66, 2016.

107. D. Okuyama, M. Bleuel, J. S. White, Q. Ye, J. Krzywon, G. Nagy, Z. Q. Im, I. Živković, M. Bartkowiak, H. M. Rønnow, and et al. Deformation of the moving magnetic skyrmion lattice in MnSi under electric current flow. *Nat. Commun. Phys.*, 2(1):79, 2019.

108. M. W. Olszewski, M. R. Eskildsen, C. Reichhardt, and C. J. O. Reichhardt. Rotational transition, domain formation, dislocations, and defects in vortex systems with combined sixfold and twelvefold anisotropic interactions. *Phys. Rev. B*, 101:224504, 2020.

109. H. K. Onnes and H. K. Onnes. Through Measurement to Knowledge, The Selected Papers of Heike Kamerlingh Onnes 1853–1926. *Boston Stud. Philos. Sci.*, page 264–266, 1991.

110. T. Y. Ou-Yang, G. J. Shu, C. D. Hu, and F. C. Chou. Manganese Deficiency in MnSi Single Crystal and Skyrmion Pinning. *IEEE Trans. Magn.*, 50(11):1–4, 2014.

111. D. Pal, L. DeBeer-Schmitt, T. Bera, R. Cubitt, C. D. Dewhurst, J. Jun, N. D. Zhigadlo, J. Karpinski, V. G. Kogan, and M. R. Eskildsen. Measuring the penetration depth anisotropy in MgB_2 using small-angle neutron scattering. *Phys. Rev. B*, 73:012513, 2006.

112. S. S. P. Parkin, M. Hayashi, and L. Thomas. Magnetic Domain-Wall Racetrack Memory. *Science*, 320(5873):190–194, 2008.

113. L. Pauling and A. M. Soldate. The nature of the bonds in the iron silicide, FeSi, and related crystals. *Acta Crystallogr.*, 1(4):212–216, 1948.

114. D. Pinna, F. A. Araujo, J.-V. Kim, V. Cros, D. Querlioz, P. Bessiere, J. Droulez, and J. Grollier. Skyrmion Gas Manipulation for Probabilistic Computing. *Phys. Rev. Appl.*, 9(6):064018, 2018.

115. R. Pynn. Neutron Scattering– A Primer. *Los Alamos Science*, page 1–31, 1990.

116. C. Rastovski, K. J. Schlesinger, W. J. Gannon, C. D. Dewhurst, L. DeBeer-Schmitt, N. D. Zhigadlo, J. Karpinski, and M. R. Eskildsen. Persistence of Metastable Vortex Lattice Domains in MgB_2 in the Presence of Vortex Motion. *Phys. Rev. Lett.*, 111:107002, 2013.

117. T. Reimann, A. Bauer, C. Pfleiderer, P. Böni, P. Trtik, A. Tremsin, M. Schulz, and S. Mühlbauer. Neutron diffractive imaging of the skyrmion lattice nucleation in MnSi. *Phys. Rev. B*, 97(2):020406, 2018.

118. S. Rohart, J. Miltat, and A. Thiaville. Path to collapse for an isolated Néel skyrmion. *Phys. Rev. B*, 93:214412, 2016.

119. F. N. Rybakov, A. B. Borisov, S. Blügel, and N. S. Kiselev. New Type of Stable Particlelike States in Chiral Magnets. *Phys. Rev. Lett.*, 115:117201, 2015.

120. T. Schulz, R. Ritz, A. Bauer, M. Halder, M. Wagner, C. Franz, C. Pfleiderer, K. Everschor, M. Garst, and A. Rosch. Emergent electrodynamics of skyrmions in a chiral magnet. *Nat. Phys.*, 8(4):301, 2012.

121. C. Schütte and A. Rosch. Dynamics and energetics of emergent magnetic monopoles in chiral magnets. *Phys. Rev. B*, 90:174432, 2014.

122. S. H. Simon. *The Oxford Solid State Basics*. Oxford University Press, Oxford, first edition. edition, 2013. ISBN 9780191502101.

123. G. Sizoo and H. Onnes. Further experiments with liquid helium. CB. Influence of elastic deformation on the supraconductivity of tin and indium. *Commun. Phys. Lab. Univ. Leiden*, (No. 180b), 1925.

124. T. Skyrme. A unified field theory of mesons and baryons. *Nucl. Phys.*, 31: 556–569, 1962.

125. A. Sokolova, A. E. Whitten, L. de Campo, J. Christoforidis, A. Eltobaji, J. Barnes, F. Darmann, and A. Berry. Performance and characteristics of the BILBY time-of-flight small-angle neutron scattering instrument. *J. Appl. Crystallogr.*, 52:1–12, 2019.

126. S. M. Stishov and A. E. Petrova. Itinerant Chiral Magnet MnSi. *J. Exp. Theor. Phys.*, 131(1):201–207, 2020.

127. D. Stosic, J. Mulkers, B. Van Waeyenberge, T. B. Ludermir, and M. V. Milošević. Paths to collapse for isolated skyrmions in few-monolayer ferromagnetic films. *Phys. Rev. B*, 95:214418, 2017.

128. G. Tatara, H. Kohno, J. Shibata, Y. Lemaho, and K.-J. Lee. Spin Torque and Force due to Current for General Spin Textures. 76:054707, 2007.

129. A. Tonomura, X. Yu, K. Yanagisawa, T. Matsuda, Y. Onose, N. Kanazawa, H. Park, and Y. Tokura. Real-Space Observation of Skyrmion Lattice in Helimagnet MnSi Thin Samples. *Nano Lett.*, 12(3):1673–1677, 2012.

130. J. Wild, T. N. G. Meier, S. Pöllath, M. Kronseder, A. Bauer, A. Chacon, M. Halder, M. Schowalter, A. Rosenauer, J. Zweck, J. Müller, A. Rosch, C. Pfleiderer, and C. H. Back. Entropy-limited topological protection of skyrmions. *Sci. Adv.*, 3:e1701704, 2017.

131. H. J. Williams, J. H. Wernick, R. C. Sherwood, and G. K. Wertheim. Magnetic Properties of the Monosilicides of Some 3 d Transition Elements. *J. Appl. Phys.*, 37(3):1256–1256, 1966.

132. M. N. Wilson, M. Crisanti, C. Barker, A. Štefančič, J. S. White, M. T. Birch, G. Balakrishnan, R. Cubitt, and P. D. Hatton. Measuring the formation energy barrier of skyrmions in zinc-substituted Cu_2OSeO_3. *Phys. Rev. B*, 99(17): 174421, 2019.

133. M. Yethiraj, H. A. Mook, G. D. Wignall, R. Cubitt, E. M. Forgan, S. L. Lee, D. M. Paul, and T. Armstrong. Anisotropic vortex lattice in $YBa_2Cu_3O_7$. *Phys. Rev. Lett.*, 71:3019–3022, 1993.

134. X. Yu, J. P. DeGrave, Y. Hara, T. Hara, S. Jin, and Y. Tokura. Observation of the Magnetic Skyrmion Lattice in a MnSi Nanowire by Lorentz TEM. *Nano Lett.*, 13(8):3755–3759, 2013.

135. X. Z. Yu, Y. Onose, N. Kanazawa, J. H. Park, J. H. Han, Y. Matsui, N. Nagaosa, and Y. Tokura. Real-space observation of a two-dimensional skyrmion crystal. *Nature*, 465(7300):901–904, 2010.

136. X. Zhang, M. Ezawa, and Y. Zhou. Magnetic skyrmion logic gates: conversion, duplication and merging of skyrmions. *Sci. Rep.*, 5(1):9400, 2015.

137. M. E. Zhitomirsky and V. H. Dao. Ginzburg-Landau theory of vortices in a multigap superconductor. *Phys. Rev. B*, 69:054508, 2004.

138. B. B. Zhou, S. Misra, E. H. d. S. Neto, P. Aynajian, R. E. Baumbach, J. D. Thompson, E. D. Bauer, and A. Yazdani. Visualizing nodal heavy fermion superconductivity in $CeCoIn_5$. *Nat. Phys.*, 9(8):474–479, 2013.

139. Y. Zhou, R. Mansell, and S. v. Dijken. Voltage control of skyrmions: creation, annihilation and zero-magnetic field stablization. *arXiv*, 2021.